INSTABILITIES IN THREE-DIMENSIONAL SOLIDS

by

John A. Vera Laboy

A thesis submitted in partial fulfillment of the requirements for the degree of

DOCTOR OF PHILOSOPHY
in
CIVIL ENGINEERING

UNIVERSITY OF PUERTO RICO
MAYAGÜEZ CAMPUS
November, 2007

Approved by:

_____   _____
Felipe J. Acosta, Ph.D.   Date
Member, Graduate Committee

_____   _____
Arsenio Cáceres, Ph.D.   Date
Member, Graduate Committee

_____   _____
Ricardo R. López, Ph.D.   Date
Member, Graduate Committee

_____   _____
Luis A. Godoy, Ph.D.   Date
President, Graduate Committee

_____   _____
Basir Shafiq, Ph.D.   Date
Representative, Graduate Studies

_____   _____
Ismael Pagán Trinidad, M.S.C.E.   Date
Director, Civil Engineering Department

ABSTRACT

This thesis presents an investigation of the buckling phenomenon and the consequences of stability theory for three-dimensional, thick solids. The theme structures considered are solid cylinders under axial compression. An analytical formulation using a linear fundamental path and an incremental displacement field is derived, leading to an eigenvalue problem. Bifurcation analyses are performed on the simplified analytical model for a variety of isotropic linear-elastic materials. Results predict bifurcations for very high deformations in modes that display a wavy pattern on the external surfaces of the cylinder. Bifurcation analyses are also performed using a general purpose finite element program. Predicted bifurcations are confirmed to appear at large deformation levels. Limit points for solid structures are also investigated with geometrically nonlinear analyses. Results show that limit point instabilities are found at smaller displacement levels than the bifurcations. A reduced energy method is developed in the thesis to obtain a lower bound to buckling loads in this problem. Earlier developments in lower bound approaches to stability problems were directed towards the buckling of thin-walled structures. The reduced energy method is applied to the solid buckling problem using the analytical formulation. Results show reasonable agreement between the reduced methodology developed and the finite element nonlinear analyses, but not lower bounds. Imperfection sensitivity, inferred from the bifurcation analysis results, is also studied. Buckling modes obtained from the finite element bifurcation analyses are imposed as imperfections on the initial geometry of the solids and nonlinear analyses are performed. Results indicate reduced displacement capacity. The effect of imperfection amplitude is also studied. Increasing amplitude is shown to lower displacement capacity of the solid, though limitations of the finite element analyses become apparent at larger imperfection amplitudes. Finally, the behavior of solid three-dimensional cylinders made with nonlinear elastic materials, foams, is investigated, to elucidate the influence of material nonlinearity on the response. Results indicate that the phenomena investigated in this thesis holds for models of such materials as well.

RESUMEN

Esta tesis presenta una investigación del fenómeno de pandeo y las consecuencias de la teoría de estabilidad para sólidos gruesos tridimensionales. Las estructuras consideradas son cilindros sólidos bajo compresión axial. Se deriva una formulación analítica usando una trayectoria fundamental lineal y un campo de desplazamientos incrementales, llegando a un problema de valores propios. Se realizan análisis de bifurcación con el modelo analítico simplificado para varios materiales isótropos y lineal-elásticos. Los resultados predicen bifurcaciones para deformaciones muy altas en modos que reflejan patrones de ondas en las superficies externas.También se realizan análisis de bifurcación usando un programa de elementos finitos. Se confirma con éstos que tales bifurcaciones aparecen a grandes niveles de deformación. Se investigan puntos límite para estructuras sólidas con análisis geométricamente nolineales. Los resultados muestran que las inestabilidades de punto límite se encuentran a niveles de desplazamiento inferiores a los de bifurcaciones. Se desarrolla un método de energía reducida para obtener límites inferiores a las cargas de pandeo. Anteriormente estos métodos se han dirigido al pandeo de estructuras de pared delgada. El método se aplica usando la formulación analítica. Los resultados muestran similitud razonable entre la metodología reducida desarrollada y los análisis nolineales con elementos finitos, pero no límites inferiores. La sensibilidad a imperfecciones, inferida de los resultados de los análisis de bifurcación, también se estudia. Modos de pandeo obtenidos de los análisis de bifurcación se utilizan como imperfecciones en la geometría inicial y se realizan análisis geométricamente nolineales. Los resultados indican que se reduce la capacidad de desplazamiento. También se estudia el efecto de la amplitud de imperfección. Se muestra que al aumentar la amplitud se reduce la capacidad de desplazamiento del sólido, aunque limitaciones del programa de elementos finitos relucen para mayores amplitudes. Finalmente, se investiga el comportamiento de cilindros sólidos de materiales elásticos nolineales, "foams", para determinar la influencia de la nolinealidad del material en la respuesta. Los resultados indican que el fenómeno también aplica a modelos con tales materiales.

To All My Grandparents

ACKNOWLEDGEMENTS

TABLE OF CONTENTS:

LIST OF FIGURES:

LIST OF TABLES:

INTRODUCTION

1.1 GENERAL INTRODUCTION

One of the great advances in theories of engineering interest following the development of the general theory of elasticity was the development of the theory of stability. The field of stability of structures finds its modern beginnings with Euler's studies of a column in the 1740's (Euler, 1744). It is interesting to note that stability problems of columns were identified before the development of a theory of elasticity, which in turn was developed before the theory of elastic stability. The studies of stability revealed the limitations of considering only material strength as a failure criterion, because in certain cases a failure dependent on both the geometry of the structure and loading conditions was found to control the design process. Studies of stability were adapted from columns to shell structures, and these two topics have since dominated stability research literature, due to observed propensity of these structures to buckling failure in common applications (von Kárman and Tsien, 1941).

There are two general types of buckling: "snap buckling" and "bifurcation buckling". These types of buckling can be visualized with a load-displacement diagram, where a displacement in some relevant point in the structure is plotted against the load. In such a plot, the path emerging from the unloaded state is the fundamental path. In snap buckling the load-displacement path is nonlinear, and reaches a maximum load where the path tangent becomes horizontal. This point is known as the limit point. In bifurcation buckling, the fundamental path may or may not be linear. Buckling occurs when the fundamental path intersects another equilibrium path, changing the trajectory of displacements - causing the geometric changes observed in buckling of this type. These deformed shapes are known as eigenmodes, eigenvectors, or simply buckling modes.

Bifurcation buckling studies reveal that several paths may exist for a given structure and loading combination, and that such paths may intersect and/or be coincident or nearly so at a point in the fundamental path. Advanced topics in stability theory include such interactions between modes at coincident critical points and their effects on the structural system. One consequence that arises from buckling mode interaction is a most important theme since the second half of the twentieth century: imperfection sensitivity. Imperfection sensitivity was first found to be the cause of large discrepancies between predicted critical loads and experimental failure loads in shells by Von Kárman and Tsien (1941). Here, the actual geometry of the structure plays the critical part in the instability process. Imperfection sensitivity may greatly decrease a structure's capacity to bear load, even in comparison to a predicted buckling load. This phenomenon was found to be greatly influenced by geometric symmetry by Koiter, who was able to explain the mechanics of coupling between modes of instability of structures and imperfections in the

geometry (Koiter, 1945). Structural forms prone to instability with imperfection sensitivity include mainly thin-walled structures such as cylindrical silo shells and sandwich beams (Evans et al., 1999). Through the insidious nature of imperfection sensitivity, instability processes surprised engineers and researchers until the phenomenon was recognized.

Within this framework of stability knowledge, we now further the cause by applying the established precepts to a fully three-dimensional problem.

1.2 JUSTIFICATION

Buckling is a physical phenomenon which occurs when a structure loses its geometric shape and becomes unstable. The study of buckling has historically been relegated to one-dimensional and two-dimensional structures (such as columns, plates, shells and thin-walled structures); however, there is no particular reason why this phenomenon should be restricted to such structures. The general criterion for stability of discrete systems is applicable to any structure (Thompson and Hunt, 1973, Godoy, 2000), and the equations in the study of stability have generally been derived with respect to three-dimensional systems. This research postulates that buckling can occur in three-dimensional solid structures, and attempts to establish under what circumstances this may occur.

The historical focus of buckling studies in thin-walled structures (for example, in thin-walled cylinders, spheres or plates) is due to the readily apparent catastrophic failures exhibited by such structures. Research has been directed mainly to produce or evaluate design processes/codes that are meant to lead to relatively "safe" thin structures (see, for example, Song and Teng, 2003). Thus, investigation into a complex and not-

readily-observable phenomenon, such as in three-dimensional solids, has not been found necessary in engineering practice. Furthermore, most engineers would consider that three-dimensional solids are not prone to buckling because they would fall under the category of stable structures. However, it is readily apparent that buckling is a three-dimensional phenomenon, wherein the special cases of thin-walled structures are contained. Also, there is the possibility of buckling as a phenomenon in a non-continuous solid. Investigation into three-dimensional buckling will yield hitherto unknown information about stability. Clearly, these possibilities are well worth investigating.

While great knowledge has been gathered about thin structures, the basic tenet regarding solids has been that stability considerations do not apply. This seems to stem originally from the time of Bryan and his work (Bryan, 1888), in which he writes:
"… it follows that the equilibrium of an elastic solid acted on by any system of bodily forces or surface tractions, which produce only small strains of the substance, is essentially stable for all displacements…". Seemingly confirmed by common engineering experience, and overshadowed by the readily apparent instability effects in columns and shells, interest in solid instabilities was quickly quelled.

In modern times, the study of three dimensional stability has not been curtailed by factors of impossibility; rather the forces which have relegated this research to a netherworld have been engineering sense and economics. Practical considerations and research evermore geared toward solutions to specific and immediate problems, have caused there to be an enormous gap in the body of knowledge regarding instabilities in thick solids.

Engineering, by its very nature, cannot be, and cannot be regarded as, static. Even though an era span generations of engineers, where no great advances are seen, still there can never be an ultimate engineering method that no man will ever improve upon, modify, or even render obsolete. Advances in materials, construction and manufacturing methods, and theories all change engineering constantly, even in imperceptibly slow fashion.

It seems then, that even if common experience dictates that a certain postulate may hold true, it is worthwhile to investigate whether these really hold, or whether common engineering experience is grounded on special cases where assumptions have been observed or are expected to hold true. This is the primary motivation in our study.

1.3 OBJECTIVES

The main objective of this research is to prove the existence of instability effects in three-dimensional, thick solids.

The specific objectives for this research are as follows:

- To verify whether old results of essential solid stability are valid.
- To extricate under what conditions instability processes may occur in a thick solid.
- To investigate the role of material properties in buckling of linear elastic solids.
- To determine whether imperfection sensitivity can occur in three-dimensional solids.
- To explore the effect of material nonlinearity in solid stability.

1.4 LITERATURE REVIEW

As mentioned earlier, the first modern works of stability recognized are Euler's studies of a column in the 1740's (Euler, 1744). Kirchhoff (1877) follows with considerations upon the equilibrium of elastic bodies with given forces, in which he concludes that equilibrium is stable except in the case of rigid body motions, a conclusion now known to be erroneous. These, and Greenhill's (1881) work in "vertical poles" and "thin wires" were noticed by Bryan (1888), perhaps the catalyst for efforts toward a theory of stability, who first took upon himself "… to give a general investigation of the circumstances under which an elastic system can be in unstable equilibrium for other than rigid body displacements of the various bodies forming the system". His work contained considerations for three dimensional elastic bodies as well as wires, plates and shells; and his conclusions in this respect were that equilibrium of three dimensional bodies would always be stable, unless rigid body motions were allowed. His work was critiqued by Southwell (1914), who pointed out several deficiencies in his work, the most important among them the assumption of small strains. Southwell himself is a step in the formulation of a general stability, as he considered a state of strain derived from the homogeneous state by infinitesimal displacements. However, Southwell's work is proof that interest in solid, three-dimensional bodies has all but vanished even at this point in time, as he concentrated on thin-walled structures such as tubular struts.

Biezeno and Hencky (1928) followed with an attempt at a true general stability theory. They considered the body in an initially known loaded state, and then a state arrived at by infinitesimal displacements. Trefftz (1933) developed stability theory from an elasticity theory for finite deformations. He used the energy criterion to judge the

stability. Biot (1938) derived the equations for neutral equilibrium from a theory of elasticity for finite deformations. Stability considerations up to this point were specifically directed towards determination of the stability limit (critical load). Koiter (1945), in his doctoral dissertation, expanded the topic of stability, investigating postbuckling paths and imperfection sensitivity. This landmark work firmly established the field of stability.

Today, elastic stability theory is well defined and methods to implement it have been developed and are widely used. General equilibrium state definitions, linear perturbation techniques, exploration of bifurcation and limit point states and methods for obtaining postcritical paths are readily available (i.e., Croll and Walker, 1972; Thompson and Hunt, 1973; Godoy, 2000). Such methods, however, have been historically applied to two-dimensional bodies (or rather, structures which are dominated by a length or two lengths in three-dimensional space).

Instabilities of thick solids have been predicted previously, but these have dealt with two-dimensional models of three-dimensional phenomena with in-plane loads. Kerr and Tang (1966) studied such a problem considering a harmonic "standard" material (a material derived from a strain energy density and whose constitutive relations are perfectly linear elastic); Wu and Widera (1969) likewise but using the Mooney-Rivlin constitutive relations. Burgess and Levinson (1972) also studied the instability of a rectangular solid in plane strain, using slightly compressible Blatz-Ko and compressible polynomial material models. Their differing results indicated the importance of the material model utilized when undertaking such investigations. However, pertinent to our investigation: all these studies on "thick solids" have been made on models with infinite

dimensions on the out-of-plane direction. Though reasonable to consider the in-plane behavior, the truth is that the infinite constraint imposed by the out-of-plane assumptions rob these studies of the potentialities of true three-dimensional behavior.

Bažant and Cedolin (1991) discuss the nuances of the finite strain tensor and its implications for three-dimensional instabilities. They state that three-dimensional solid stability must be evaluated using finite strain tensors. Thus, the geometrically nonlinear nature of the tensor severely complicates the analysis, since even different definitions of the tensor stress must be used. However, this requirement is more an assumption based on the results obtained by Bryan (1888), than a strict research conclusion. They list possibilities of critical states on solids, and restrict them to the following cases:

1) Highly anisotropic materials.

2) Certain composite structures having soft components.

3) Continuum approximations of latticed structures.

4) Materials that undergo a drastic reduction of tangential stiffness due to damage, plasticity, or shear, cracking or crushing bands.

These are hardly materials for elastic stability. Such a case-by-case approach, while practical and utilitarian, does not advance general knowledge: each case is a beautiful spire – with foundations still unseen.

Three-dimensional studies of structures such as sandwich columns (Bažant and Beghini, 2004) consider a mix of materials where the differing properties induce factors from which the instability effect cannot be extricated. In addition, such columns, while short, cannot be considered thick solids. The instability processes of sandwich panels with foam core material have been investigated previously and have gone as far as including the

interaction between global and local instabilities (Léotoing et al., 2005). However, the possibility of a macroscopic type of instability – that of the material in solid form - has not been studied. In this instability process, there would be imperfection sensitivity to geometric deviations of the solid from its ideal form. This type of macro sensitivity we enunciate is distinct and different from imperfection sensitivity of the foam microstructure, where morphological deviations play a crucial role in defining the material behavior: these imperfections catalyze the onset of instability that defines the elastic limit of a foam (Gong et al., 2005). Geometric *structural* deviations, on the other hand, would facilitate instabilities of the solid as a whole.

In engineered systems, the elastic behavior is typical of small strains under service loads; however, most designs tend now to be based on limit state considerations, in which plasticity and fracture are taken into account. The instability of 3D bodies has been mainly investigated in the context of the failure of soils and granular solids, in which case there are failure surfaces and material plasticity plays an important role.

But there are many systems in nature for which an elastic behavior is the only way to perform a function. For such systems, the elastic behavior is a key part of the normal functioning of the system.

Consider for example the behavior of muscles in human and animal bodies, illustrated in Figure 1.1. Voluntary muscles consist of bundles of cells called myofibers. Inside the myofibers there are strands of myofibrils containing the proteins (actin and myosin).
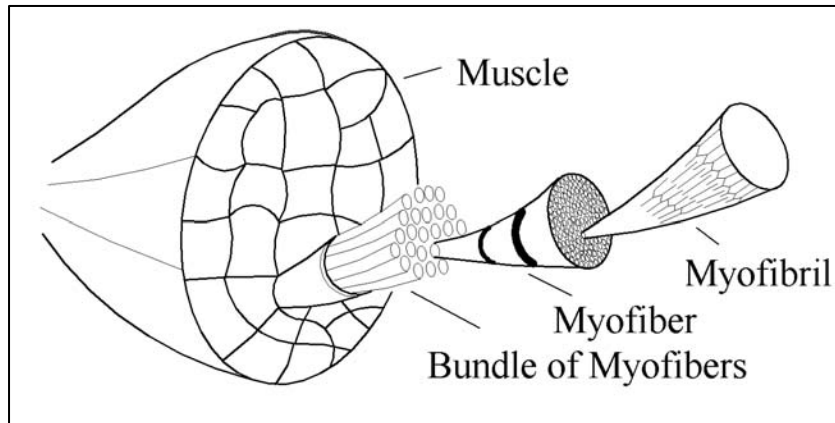
Figure 1.1. Bundles of myofibers in a contracting muscle.

In a contracting muscle, the myosin filaments overlap, making the muscle shorter. The contraction of a muscle is not a high speed action and is usually controlled by the animal or human being. In Figure 1.2, on the left the muscle is shown in a contracted position, whereas it is relaxed on the right of the image. The actual shape of the muscle illustrated in Figure 1.2 does not involve a significant change in shape, so that the external surface appears to coincide in both cases.
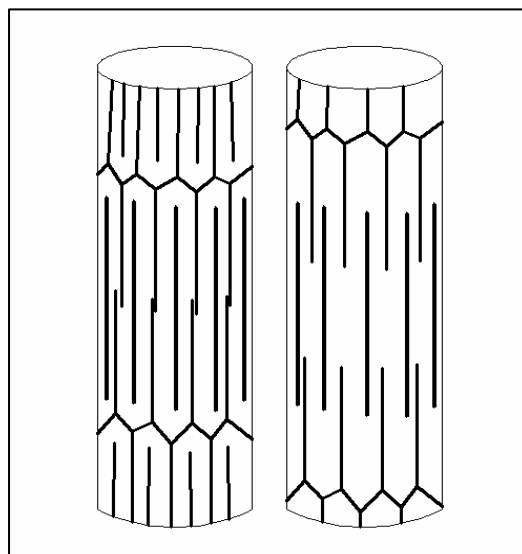
Figure 1.2. Contracted and relaxed configurations of a muscle.

In the previous figure it is shown that a change in length is not accompanied by a change in the diameter of the filaments. However, the actual details of the shape of the contracted muscle have not been investigated in detail by researchers in this field; i.e. what are the mechanisms of deformation between the two configurations of a muscle in order to change its length? Are there volume changes during the process? Figure 1.3 shows a section of an aortic valve. Notice the corrugations on the inside surface. The specialized extra cellular matrix enables dynamic aortic valve function (Schoen, 2006).
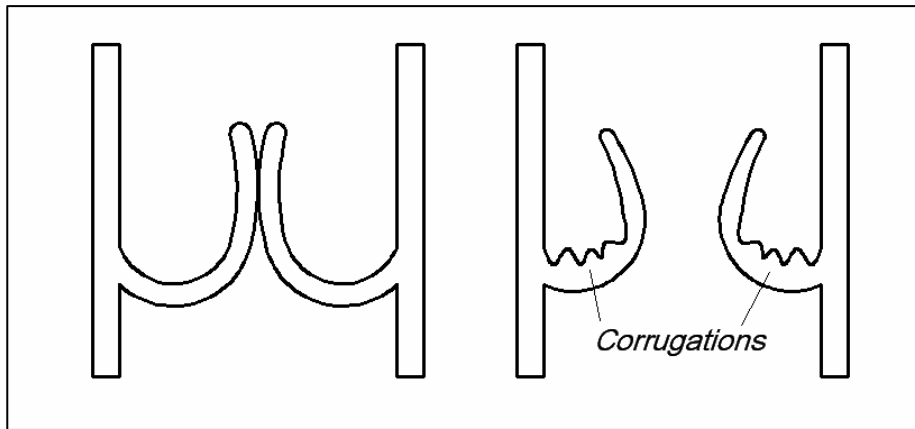
Figure 1.3. Valve dynamics in cyclical cardiac function.

What does the preceding figure imply? Research could conceivably show that the valve deforms according to a preset shape. But it is also possible that the natural mechanism makes use of the buckling phenomenon.

In contrast to the workings of the previously mentioned cases, there are many situations in which the problem has been studied in great detail, because the actual mechanism of contraction is vital to the understanding of the functioning of a muscle and the survival of the individual. One such case is the catch mechanism in *Eucidaris tribuloides* (a sea urchin), for which several hypotheses have been proposed (del Castillo

et al., 1995; Elphick and Melarange, 2001) and falsified (Takemae and Motokawa, 2005). In essence the problem consists of the organism being able to alter the stiffness of a non-muscle type cellular structure. But loss of stiffness has the stamp of buckling process at work. These investigations do not consider this possibility.

Corrugations similar to those of Figure 1.3 can be seen in a man-made material. Figure 1.4 shows a synthetic rubber in a wrist rest of a mouse pad. Notice the surface corrugations under bending, which can be seen through the nearly transparent material.

(a)
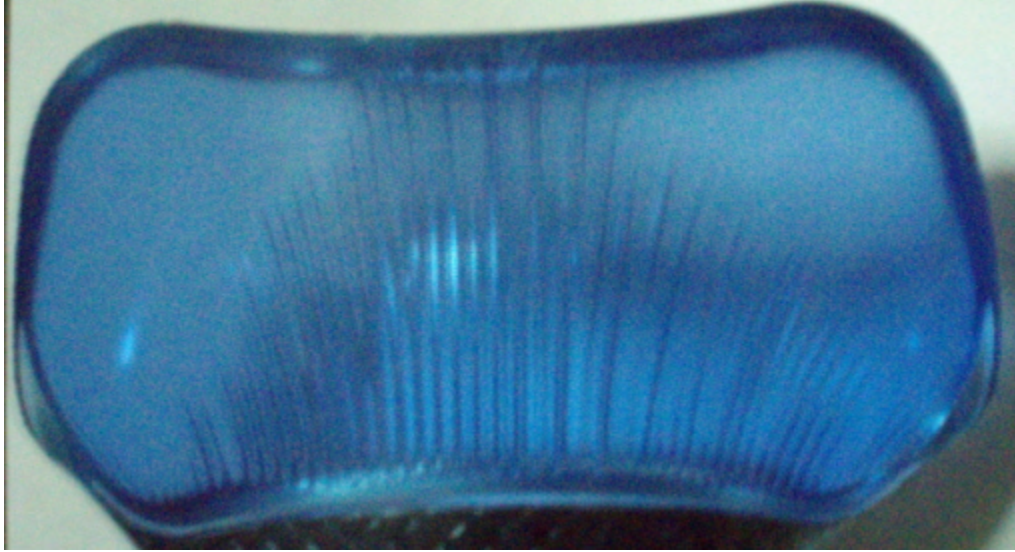
(b)

Figure 1.4. Corrugations on man made rubber material under bending, (a) Front view;
(b) Top view.

Why does this occur? What determines the number and size of the corrugations?

These are unknowns at present, but one thing is clear: this is a buckling phenomenon at

work, because for slight bending there are no corrugations. In this material, there is surely

a buckling point being crossed.

Another field in which the buckling process may be of relevance is the mechanics

of glaciers, in which masses of fluidized ice under pressure deflect as the glacier moves,

and the mechanics of snow. Similar changes in stiffness in the rock masses can also be

seen as buckling processes (Bažant and Cedolin, 1991). Those are usually slow motion

processes, however, and not immediately apparent as buckling consequences.

Considering the possibilities, 3D solid buckling is an interesting area for research;

however, so far as we are able to see, a study of a thick, nonslender structure made of a

single material has not been realized. Therefore, the nuances of an instability process in a

three-dimensional solid cannot be considered to have been extracted at present.

1.5 SCOPE

This investigation focuses on three-dimensional solids, specifically solid cylinders under compression. The primary materials used follow the linear elastic model, although a nonlinear foam model is also utilized in the course of the investigation. All material models are isotropic. Linearity of the system response is assumed in the fundamental path used to develop an analytical formulation and in the linear analyses using finite elements. Nonlinearity (large displacement theory) is assumed in geometrically nonlinear finite element analyses.

1.6 METHODOLOGY

In order to carry out this investigation, two approaches are taken: analytical and computational. An analytical formulation based on the total potential energy is developed and a simplified version is used to perform eigenvalue extraction analyses for various incremental displacement fields. These analyses correspond to critical states associated to bifurcations. Bifurcations are also evaluated with buckling analyses using finite elements. Finite elements are also used to evaluate limit point critical states, which necessitate nonlinear step-by-step methods such as that found in our finite element package. This research makes extensive use of the finite-element program ABAQUS. This program has been chosen because of its versatility, historical reliability, capabilities and availability. Linear, nonlinear and buckling analyses are performed with this program.

Further along in our investigation, we integrate the reduced energy methodology into our simplified analytical formulation. A trial and error approach is taken in order to

determine the relevant energy terms to be eliminated from the total potential energy when following this methodology.

The finite element method is again used when evaluating imperfection sensitivity. Imperfections are taken from eigenmodes which result from the bifurcation analyses using finite elements. The eigenmodes are imposed as imperfections on the initial geometry of the solid.

1.7 ORGANIZATION

This thesis is organized in seven chapters and an appendix. The present chapter contains the general introduction to our investigation (instabilities of three-dimensional solids), as well as the motivation, objectives, literature review, scope and methodology followed in the course of the research..

Chapter 2 presents a simplified analytical approach using the total potential energy formulation. A theme problem of solid cylinder under compressive load is studied. Linear elastic materials are assumed. Both the derivation of the problem and results of bifurcation buckling analyses are presented. Results are given for various materials and cylinder heights.

Chapter 3 includes bifurcation, linear and nonlinear analyses of the theme problem, using the finite element method. Comparisons are made between all results, including the ones obtained in the preceding chapter.

In Chapter 4, the reduced energy methodology is applied to the 3D solid problem using the analytical formulation developed in Chapter 2. The contributions of individual potential energy terms are evaluated. The results are compared to those of preceding chapters.

Chapter 5 presents a study of imperfection sensitivity in the theme solid. Buckling modes are imposed as initial imperfections upon the solid geometry and nonlinear analyses are performed. The results are then compared to the nonlinear analyses without imperfections.

In Chapter 6, the effect of material nonlinearity on the solid buckling problem is evaluated using highly nonlinear materials, foams. Imperfection sensitivity was also explored for these materials. Both nonlinear analyses with and without imperfections were performed. Again, buckling modes are imposed as initial imperfections upon the solid geometry, and the effects of imperfection amplitude evaluated.

In closing, Chapter 7 gives our general conclusions and future work recommendations.

SIMPLIFIED ANALYSIS OF BIFURCATIONS IN 3D SOLIDS

2.1 INTRODUCTION

As previously mentioned in Chapter 1, knowledge of stability of thick solids at present can hardly be considered more than pervasive belief . This in part is due to the conclusions of Bryan in his 1888 work (Bryan, 1888), which considered full three-dimensional stability, however utilizing linearity assumptions which unwittingly produced negative results for the buckling of thick solids. Said conclusions at the forefront of the field, the initial assumptions were accepted tacitly - resulting in the persistence of the intuitive belief that solids *could not* buckle. In more recent times, works with other cases that might be considered three-dimensional (Kerr and Tang, 1966; Wu and Widera, 1969; Burgess and Levinson, 1972), while now including the full stability considerations, contained constraint assumptions which made said investigations little more than plane representations.

In this chapter we present the total potential energy and its use as stability criterion. A fully three-dimensional formulation for buckling of a solid is developed. Results of eigenvalue extraction analyses on models of solid cylinders under compression are presented and discussed.

2.2 THE TOTAL POTENTIAL ENERGY

The total potential energy is a functional used in theoretical elasticity and frequently in elastic stability problems. As its name indicates, it is a summation of all energy in the structure considered. The total potential energy is defined mathematically as:

$$V \equiv \int_V \omega d\mathrm{V} + \int_V \rho d\mathrm{V} + \int_{S_f} \psi d\mathrm{S} \tag{2.1}$$

where V is the total potential energy, ω is the strain energy density per unit volume of the body, ρ is the potential of the forces in the volume of the body, ψ is the potential of the forces acting on the boundaries, dV is a differential of the volume of the body an dS is a differential of the surface space of the body. The integration limit S_f on the third term in the right side of equation 2.1 refers to the parts of the surface where forces are defined (even if they are zero on a free boundary condition). [*]

The strain energy density per unit volume of the body, ω, refers to the internal energy produced by the stresses (σ) and strains (ε) in the body. In the material cases considered, which are linear elastic, the strain energy density becomes:

---

[*] Mixed boundaries, in which load and displacement components are both defined at the same location, are not considered in this work.

18

$$\omega = \frac{1}{2}\sigma_{ij}\varepsilon_{ij} \qquad (2.2)$$

where indicial notation implies a sum of terms for i = 1, 2, 3 and j = 1, 2, and 3.

The potential of the forces in the volume of the body, ρ, and the potential of the forces acting on the boundaries, ψ, are usually taken in simple form as:

$$\rho = -F_i u_i$$
$$\qquad (2.3)$$
$$\psi = -f_i u_i$$

where F_i's are forces per unit volume and f_i's are forces per unit surface, while the u_i's refer to the displacements in the directions in which the forces act. Further assuming that these forces all increase at the same rate, they can be represented by a single control parameter, Λ:

$$\rho = -\Lambda \ F_i u_i$$
$$\qquad (2.4)$$
$$\psi = -\Lambda \ f_i u_i$$

The energy for a structure governed by a single load parameter, composed of a single linear elastic material is:

$$V \equiv \frac{1}{2}\int_V \sigma_{ij}\varepsilon_{ij}dV - \Lambda\int_V F_i u_i dV - \Lambda\int_{S_f} f_i u_i dS \qquad (2.5)$$

The displacements u_i are used to obtain the strains ε_{ij} with the kinematic equations

$$\varepsilon_{ij} = \frac{1}{2}\left(\frac{\partial u_i}{\partial x_j} + \frac{\partial u_j}{\partial x_i} + \frac{\partial u_m}{\partial x_i}\frac{\partial u_m}{\partial x_j}\right) \qquad (2.6)$$

In which the u_i's represent the displacements in the i- direction, and the x_i's are the coordinate directions.

The stresses σ_{ij} in turn are obtained from the strains ε_{ij} by the material constitutive relations, which in the case of a linear elastic isotropic material take the form:

$$\sigma_{ij} = \frac{E}{1+v}\left(\varepsilon_{ij} + \frac{v}{1-2v}\delta_{ij}\varepsilon_{mm}\right) \tag{2.7}$$

where E is Young's modulus (or elastic stress-strain rate), v is Poisson's ratio (or ratio of lateral strain to axial strain caused by a load in the axial direction), and δ_{ij} is Kronecker's delta, which takes a unit value for i=j and is zero otherwise.

2.2.1 Total Potential Energy and Stability

The total potential energy's usefulness primarily comes from the fact that higher order variations of it are directly related to critical stability states. The first variation of the total potential energy with respect to the displacement field is related to the equilibrium of a state. For the form we have described previously (Equation 2.5), the first variation of the total potential energy becomes:

$$\delta V \equiv \frac{1}{2}\int_{V}\sigma_{ij}\delta\varepsilon_{ij}dV - \Lambda\int_{V}F_{i}\delta u_{i}dV - \Lambda\int_{S_{f}}f_{i}\delta u_{i}dS \tag{2.8}$$

According to the principle of virtual work, which states: "A necessary and sufficient condition for equilibrium of a set of forces and stresses is that, for any virtual displacement field, the internal virtual work should be equal to the external virtual work" (Washizu, 1968), the sum of internal and external work should be zero. Naming the virtual displacements δu_{i}, the virtual strains obtained from the virtual displacements following the kinematic equations (Equation 2.6) are $\delta\varepsilon_{ij}$. Letting σ_{ij} be real stresses in a problem, the internal virtual work is:

$$IVW = \frac{1}{2} \int_{V} \sigma_{ij} \delta \varepsilon_{ij} dV \tag{2.9}$$

If F_i and f_i are the real forces of the problem, then the external virtual work is:

$$EVW = \Lambda \int_{V} F_i \delta u_i dV + \Lambda \int_{S_f} f_i \delta u_i dS \tag{2.10}$$

Equality of internal and external virtual work implies that the summation of these terms should be zero. Therefore we obtain:

$$\frac{1}{2} \int_{V} \sigma_{ij} \delta \varepsilon_{ij} dV - \Lambda \int_{V} F_i \delta u_i dV - \Lambda \int_{S_f} f_i \delta u_i dS = 0 \tag{2.11}$$

This form matches exactly the terms of the first variation of the total potential energy if we let δu_i be the actual displacements of the problem, which obey the kinematic relations. The condition of equilibrium of a load state from the first variation of the potential energy is:

$$\delta V = 0 \tag{2.12}$$

Furthermore, the total potential energy is also a criterion of stability for said equilibrium states, in the second variation. For stability of an equilibrium state, the total potential energy must be a minimum with respect to the displacement field.

The energetic criterion of stability can be stated simply:

if:

$$\delta^2 V > 0 \tag{2.13}$$

Then the state is stable. If:

$$\delta^2 V < 0 \tag{2.14}$$

the state is unstable.

The third alternative:

$$\delta^2 V = 0 \tag{2.15}$$

indicates a state of neutral equilibrium, also known as a critical state.

It is to the third condition that buckling is associated to. Critical states usually imply a deformation of the structure that changes its shape significantly. These changes may be considered adverse or beneficial, but more often than not, they represent a failure of the structure for all intents and purposes. That is why it has become an important part of structural engineering to evaluate structures and structural members for the possibility of failure by buckling.

There are two general types of buckling: "snap buckling" and "bifurcation buckling". These types of buckling can be visualized with a load-displacement diagram, where a displacement in some relevant point in the structure is plotted against the load. In such a plot, the path emerging from the unloaded state is the fundamental path.

As shown in Figure 2.1, in snap buckling the load-displacement path is nonlinear, and reaches a maximum load where the path tangent becomes horizontal. This point is known as the limit point.
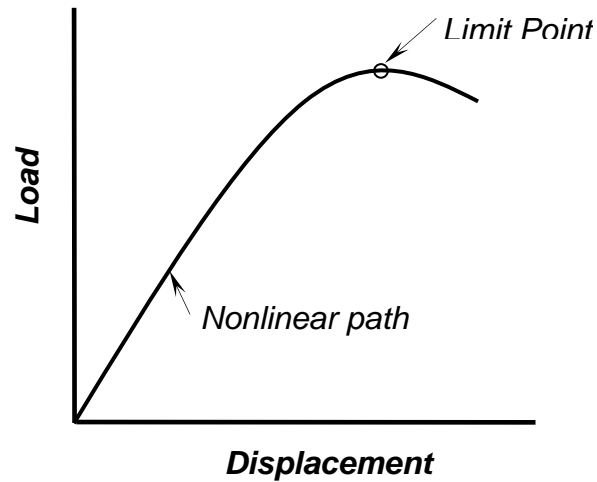
Figure 2.1. Sample load-displacement behavior for snap buckling.

The fundamental path may or may not be linear in bifurcation buckling. Buckling occurs when the path intersects another equilibrium path, which changes the trajectory of the displacement (which causes the geometric changes observed in buckling of this type). This is illustrated in Figure 2.2.
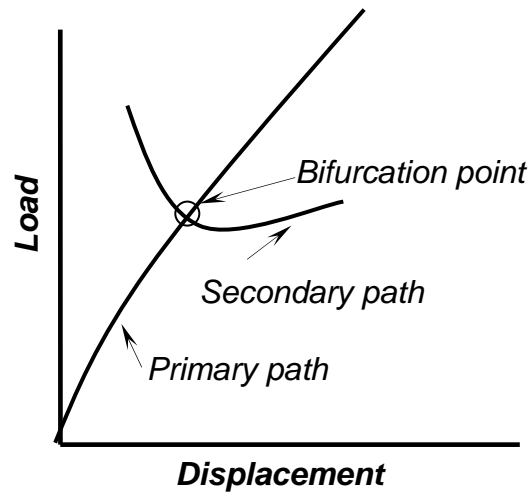
Figure 2.2. Sample load-displacement behavior for bifurcation buckling.

In this work we aim to investigate the critical states of three-dimensional solids, but we do not seek to evaluate the stability of such states or explore post-critical paths. For further discussion on buckling, limit point and bifurcation paths, the reader is referred to Croll and Walker, 1972; Thompson and Hunt, 1973; and Brush and Almroth, 1975.

2.3 STABILITY OF A SOLID USING THE TOTAL POTENTIAL ENERGY

Considering a general solid structure, let us denote the total displacements of the structure as the sum of the fundamental path displacements and incremental displacements:

$$U_i = U_i^F + u_i \tag{2.16}$$

where the U_i^F represent the fundamental path displacements and the u_i are the incremental displacements. This is a convenient way to investigate buckling because the displacements in the fundamental path may be derived in a simplified way, whereas a more detailed representation may be given to the incremental displacements u_i. The strains obtained from kinematic relations, divided into the terms coming from the fundamental path and incremental displacements, are:

$$\varepsilon_{ij} = \varepsilon_{ij}^F + \varepsilon_{ij}^{'} + \varepsilon_{ij}^{''} \tag{2.17}$$

Where:

$$\varepsilon_{ij}^F = \frac{1}{2}\left(\frac{\partial U_i^F}{\partial x_j} + \frac{\partial U_j^F}{\partial x_i}\right)$$

$$\varepsilon_{ij}^{'} = \frac{1}{2}\left(\frac{\partial u_i}{\partial x_j} + \frac{\partial u_j}{\partial x_i}\right) \quad (2.18)$$

$$\varepsilon_{ij}^{''} = \frac{1}{2}\left(\frac{\partial u_m}{\partial x_i}\frac{\partial u_m}{\partial x_j}\right)$$

The first line in Equation 2.18 is the linear contribution to the fundamental path; the second line is the linear contribution to the incremental strains, the third line represents the non linear contribution to the incremental strains.

The total strains are comprised of the linear terms from the fundamental path, the linear terms from the incremental displacements and the nonlinear terms from the incremental displacements. As the fundamental path is assumed to be linear, there are no nonlinear terms arising from the fundamental path.

The stresses, obtained from the constitutive equations, can be separated similarly:

$$\sigma_{ij} = \sigma_{ij}^{F} + \sigma_{ij}^{'} + \sigma_{ij}^{''} \quad (2.19)$$

Substituting into Equation 2.5, we obtain:

$$V = \frac{1}{2}\int_{V}(\sigma_{ij}^{F} + \sigma_{ij}^{'} + \sigma_{ij}^{''})(\varepsilon_{ij}^{F} + \varepsilon_{ij}^{'} + \varepsilon_{ij}^{''})dV$$
$$- \Lambda\int_{V}F_i(U_i^{F} + u_i)dV - \Lambda\int_{S_f}f_i(U_i^{F} + u_i)dS \quad (2.20)$$

Expanding the equation and separating the stress-strain terms according to their degree (constant, linear, quadratic, etc), the total potential energy is:

$$V = \frac{1}{2}\int_V \sigma_{ij}^F \varepsilon_{ij}^F \, dV + \frac{1}{2}\int_V (\sigma_{ij}^F \varepsilon_{ij}^{'} + \sigma_{ij}^{'}\varepsilon_{ij}^F)\, dV$$

$$+ \frac{1}{2}\int_V (\sigma_{ij}^{'}\varepsilon_{ij}^{'} + \sigma_{ij}^F \varepsilon_{ij}^{''} + \sigma_{ij}^{''}\varepsilon_{ij}^F)\, dV$$

$$+ \frac{1}{2}\int_V (\sigma_{ij}^{'}\varepsilon_{ij}^{''} + \sigma_{ij}^{''}\varepsilon_{ij}^{'})\, dV \quad + \frac{1}{2}\int_V (\sigma_{ij}^{''}\varepsilon_{ij}^{''} + \sigma_{ij}^{''}\varepsilon_{ij}^{''})\, dV \qquad (2.21)$$

$$- \Lambda\int_V F_i(U_i^F + u_i)\, dV - \Lambda\int_{Sf} f_i(U_i^F + u_i)\, dS$$

Listing the energy terms, represented as V_i, with increasing stress-strain order:

$$V = V_0 + V_1 + V_2 + V_3 + V_4 \qquad (2.22)$$

V_0 contains only fundamental path terms:

$$V_0 = \frac{1}{2}\int_V \sigma_{ij}^F \varepsilon_{ij}^F \, dV - \Lambda\int_V F_i U_i^F \, dV - \Lambda\int_{Sf} f_i U_i^F \, dS \qquad (2.23)$$

so it is a constant, independent of the incremental terms.

 The terms that make up V_1:

$$V_1 = \frac{1}{2}\int_V (\sigma_{ij}^F \varepsilon_{ij}^{'} + \sigma_{ij}^{'}\varepsilon_{ij}^F)\, dV - \Lambda\int_V F_i u_i)\, dV - \Lambda\int_{Sf} f_i u_i dS \qquad (2.24)$$

equal the first variation of the total potential energy with respect to the fundamental state.

$$V_1 = \delta V \qquad (2.25)$$

The solution of $V_1 = 0$ returns the fundamental path (σ_{ij}^F, ε_{ij}^F). The terms V_2, V_3 and V_4 have no load terms, only internal deformation energy. The terms that make up V_2 are the quadratic terms in incremental displacements:

$$V_2 = \frac{1}{2}\int_V (\sigma_{ij}^{'}\varepsilon_{ij}^{'} + \sigma_{ij}^F \varepsilon_{ij}^{''} + \sigma_{ij}^{''}\varepsilon_{ij}^F)\, dV \qquad (2.26)$$

V_2 equals the second variation of the potential energy:

$$V_2 = \delta^2 V \tag{2.27}$$

We consider the case where the second variation is zero, and the fundamental path can be scaled by virtue of its linearity. We use the load control parameter Λ as the scale factor for the fundamental path terms. Denoting the fundamental path terms corresponding to a unit load system as $\overline{\sigma}_{ij}^F$ for stresses and $\overline{\varepsilon}_{ij}^F$ for strains, we arrive at:

$$\int_V \sigma_{ij}' \varepsilon_{ij}' dV + \Lambda \int_V (\overline{\sigma}_{ij}^F \varepsilon_{ij}'' + \sigma_{ij}'' \overline{\varepsilon}_{ij}^F) dV = 0 \tag{2.28}$$

which is an eigenvalue and eigenvector problem. The eigenvalue is Λ, the load multiplier that increases the stresses and strains along the fundamental path. The eigenvector is not explicitly shown in Equation 2.28, but is evident when the incremental displacement field is defined. In explicit form:

$$
\begin{aligned}
&\int_V (\sigma_{11}' \varepsilon_{11}' + \sigma_{22}' \varepsilon_{22}' + \sigma_{33}' \varepsilon_{33}' + 2\sigma_{12}' \varepsilon_{12}' + 2\sigma_{13}' \varepsilon_{13}' + 2\sigma_{23}' \varepsilon_{23}') dV \\
&+ \Lambda \int_V (\sigma_{11}^F \varepsilon_{11}'' + \sigma_{22}^F \varepsilon_{22}'' + \sigma_{33}^F \varepsilon_{33}'' + 2\sigma_{12}^F \varepsilon_{12}'' + 2\sigma_{13}^F \varepsilon_{13}'' + 2\sigma_{23}^F \varepsilon_{23}'') dV \\
&+ \Lambda \int_V (\sigma_{11}'' \varepsilon_{11}^F + \sigma_{22}'' \varepsilon_{22}^F + \sigma_{33}'' \varepsilon_{33}^F + 2\sigma_{12}'' \varepsilon_{12}^F + 2\sigma_{13}'' \varepsilon_{13}^F + 2\sigma_{23}'' \varepsilon_{23}^F) dV = 0
\end{aligned} \tag{2.29}
$$

2.4 PROBLEM FORMULATION

To illustrate the behavior of a solid 3D elastic body, a simple problem has been considered in this thesis. We treat a thick cylindrical solid under uniform pressure P, as shown in Figure 2.3.
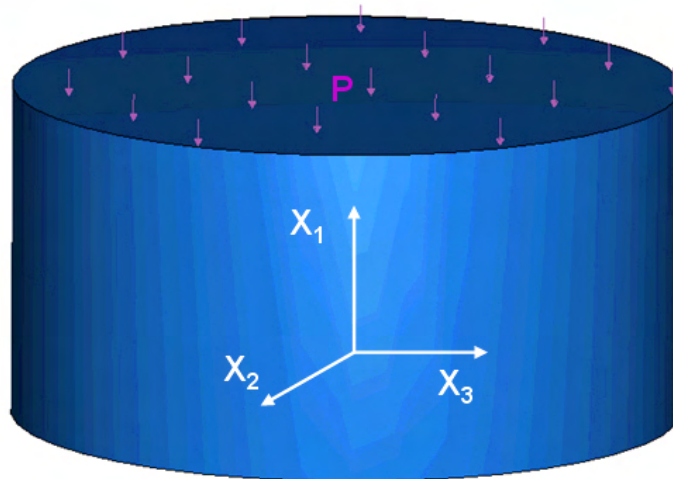
Figure 2.3. Coordinate axes and load in theme solid.

This is a problem for which analytical approximations are possible, and which exhibits symmetry. Symmetry has been recognized as an important component in instability problems. An excellent account of the role of symmetry in instability is given in *Fearful Symmetry: is God a Geometer?* by I.Stewart and M. Golubitsky (1992).

As the solid is cylindrical, a convenient coordinate system is the one presented in Figure 2.4, in which the position of each point is identified by a radius, a circumferential coordinate which follows the angle θ, and the elevation.
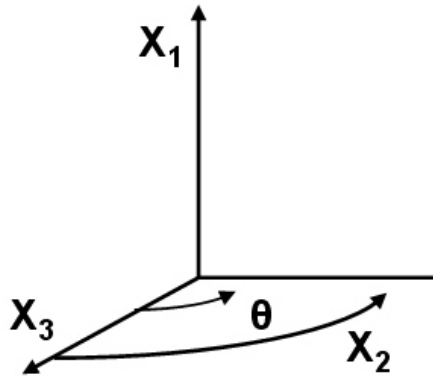
Figure 2.4. Coordinate axes in cylindrical system.

In the preceding figure, X_1 is the vertical direction, X_3 the radial direction, and X_2 a circumferential direction (θ denotes the angular path of the X_2 coordinate).

2.4.1 Definition of the Linear Fundamental Path

For this simple problem, the linear fundamental path can be defined by establishing the axial stress as load divided by the cross-sectional area, and the other stresses set to zero.

$$\sigma_{11}^F = P \qquad \sigma_{12}^F = 0$$

$$\sigma_{22}^F = 0 \qquad \sigma_{13}^F = 0 \tag{2.30}$$

$$\sigma_{33}^F = 0 \qquad \sigma_{23}^F = 0$$

This is clearly an approximation to the solution, because idealized boundary conditions are required to satisfy such a stress state.

The strains are obtained from the stresses using linear elasticity constitutive equations:

$$\varepsilon_{ij} = \frac{(1+v)}{E}\left(\sigma_{ij} - \frac{v}{(1+v)}\delta_{ij}\sigma_{mm}\right) \qquad (2.31)$$

Where E is Young's modulus, v is Poisson's ratio, ε_{ij} are the components of the strain tensor, σ_{ij} the components of the stress tensor, and δ_{ij} Kronecker's delta in indicial notation, which is equal to one when the indices are equal and zero otherwise.

The strain terms in the fundamental path become:

$$\varepsilon_{11}^{F} = \left(\frac{P}{E}\right)$$

$$\varepsilon_{22}^{F} = \left(\frac{-vP}{E}\right) \qquad (2.32)$$

$$\varepsilon_{33}^{F} = \left(\frac{-vP}{E}\right)$$

Since the shear stresses are zero and linear isotropic elasticity is considered, the shear strains along the fundamental path are also zero:

$$\varepsilon_{12}^{F} = 0$$

$$\varepsilon_{13}^{F} = 0 \qquad (2.33)$$

$$\varepsilon_{23}^{F} = 0$$

The fundamental path stress and strain tensors are already in their principal form:

$$\sigma_{ij}^{F} = \begin{bmatrix} P & 0 & 0 \\ 0 & 0 & 0 \\ 0 & 0 & 0 \end{bmatrix}$$

$$(2.34)$$

$$\varepsilon_{ij}^F = \begin{bmatrix} \dfrac{P}{E} & 0 & 0 \\ 0 & \dfrac{-vP}{E} & 0 \\ 0 & 0 & \dfrac{-vP}{E} \end{bmatrix}$$

In summary, the linear fundamental path defined assumes that there are no shear stresses or strains and that linear elasticity is followed (no second order stress or strain terms). Furthermore, we assume the compressive uniformly distributed load P to have a unit value, and use the load parameter Λ as the load unknown in the total potential energy.

2.4.2 Definition of the Incremental Displacement Field

Stability problems, like many others in engineering, are usually discretized in order to reduce the number of unknowns to a manageable or desired quantity. This is typical of the finite-element method, where unknowns such as displacements are determined only at certain locations in the structure and functions are used to interpolate for the values in between such locations. With the potential energy it also serves well to use a discrete number of unknowns in the context of the Rayleigh-Ritz method. This can be achieved by utilizing generalized coordinates (degrees of freedom), which are not necessarily displacement unknowns at a point in the structure but might also be multipliers of displacement functions, or the variables that the displacements are functions of. Denoting the generalized coordinates as Q_i's, the displacements can be written as:

$$u_j = u_j(Q_i)$$ (2.35)

with the discretized system the total potential energy V becomes a function of the generalized coordinates and the load parameter:

$$V = V[Q_i, \Lambda]$$ (2.36)

We employ such a discretized system in the definition of the incremental displacement field. Three displacement equations define the eigenmode. First, we assume that the eigenmode may be solely defined in terms of the radial displacement component u_3, and that the axial and tangential displacements may be neglected. Thus, both the axial (1-direction) and angular (2-direction) incremental displacements are set equal to zero:

$$u_1 = 0$$
$$u_2 = 0$$ (2.37)

The mode definition is completed by using a shape function for the radial incremental displacements as follows:

$$u_3 = \left(\frac{x_3}{R}\right) * \sin\left(\frac{\pi M x_1}{L}\right) * \sin\left(\frac{N x_2}{2R}\right) * Q$$ (2.38)

Where u_3 is the radial incremental displacement, R the radius and L the length of the solid; M and N the number of waves in the axial and circumferential directions, respectively, for the mode described; x_1, x_2 and x_3 the axial, angular distance and radial coordinates of the points inside the cylinder and Q is the radial generalized coordinate. This generalized coordinate represents the "primary" radial displacement, a magnitude that, multiplied by the other terms in the u_3 function, gives the mode shape its ultimate size.

The boundary conditions to be satisfied are: $u_3=0$ at $x_1=0$ and $x_1=L$. The sine term in the x_1 direction sets the radial displacements to zero on the top and bottom borders, allowing for the set number of waves. The sine term sets the number of waves in the x_2 (circumferential) direction. The radial displacement is set to increase linearly from zero outwards with increasing radius (the x_3/R term).

Figure 2.5 is a three-dimensional plot of the shape function with the generalized coordinate Q set to 1, with the base radial coordinate x_3 equal to unity, for a unit height. The number of waves M and N both set equal to 2. The axial coordinates are on the X1 axis, while the circumferential coordinates are on the X2 axis. The radial displacements on the surface of the solid, normalized to unity, are plotted on the X3 axis. As can be seen, the figure is composed of two inward and two outward bulges.
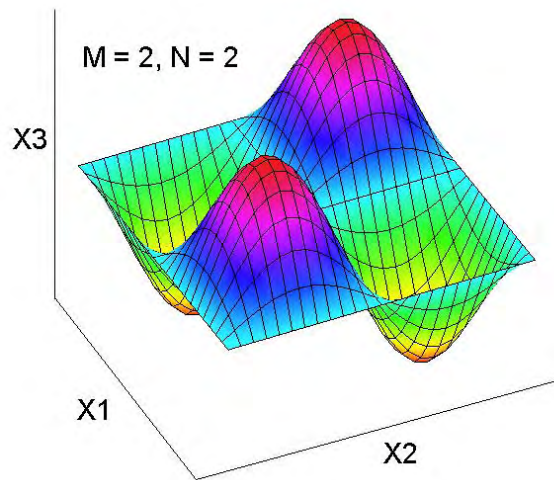
Figure 2.5. 3D plot of wave function for incremental radial displacement.

For the incremental state, the strains are obtained directly from the displacement functions. Considering first the linear components:

$$\varepsilon'_{11} = \frac{\partial u_1}{\partial x_1} = 0$$

$$\varepsilon'_{22} = \frac{\partial u_2}{\partial x_2} = 0$$

$$\varepsilon'_{33} = \frac{\partial u_3}{\partial x_3} = \sin\left(\frac{\pi M x_1}{L}\right) * \sin\left(\frac{N x_2}{2R}\right) * \frac{Q}{R}$$

$$\varepsilon'_{12} = \varepsilon'_{21} = \frac{1}{2}\left(\frac{\partial u_1}{\partial x_2} + \frac{\partial u_2}{\partial x_1}\right) = 0$$

(2.39)

$$\varepsilon'_{13} = \varepsilon'_{31} = \frac{1}{2}\left(\frac{\partial u_1}{\partial x_3} + \frac{\partial u_3}{\partial x_1}\right) = \frac{\pi M x_3}{2RL} * \cos\left(\frac{\pi M x_1}{L}\right) * \sin\left(\frac{N x_2}{2R}\right) * Q$$

$$\varepsilon'_{23} = \varepsilon'_{32} = \frac{1}{2}\left(\frac{\partial u_2}{\partial x_3} + \frac{\partial u_3}{\partial x_2}\right) = \frac{N x_3}{4R^2} * \sin\left(\frac{\pi M x_1}{L}\right) * \cos\left(\frac{N x_2}{2R}\right) * Q$$

The strain tensor of linear components of incremental strains is:

$$\varepsilon'_{ij} = \begin{bmatrix} 0 & 0 & \varepsilon'_{13} \\ 0 & 0 & \varepsilon'_{23} \\ \varepsilon'_{13} & \varepsilon'_{23} & \varepsilon'_{33} \end{bmatrix}$$

(2.40)

The associated stress tensor, obtained by constitutive relations, is:

$$\sigma'_{ij} = \begin{bmatrix} \sigma'_{11} & 0 & \sigma'_{13} \\ 0 & \sigma'_{22} & \sigma'_{23} \\ \sigma'_{13} & \sigma'_{23} & \sigma'_{33} \end{bmatrix}$$

(2.41)

Even though σ'_{11} and σ'_{22} are present in the tensor, they do not participate in the energy calculation, since the associated strain terms annul them.

The nonlinear strain components are:

$$\varepsilon''_{11} = \frac{1}{2}\left(\frac{\partial u_1}{\partial x_1}\frac{\partial u_1}{\partial x_1} + \frac{\partial u_2}{\partial x_1}\frac{\partial u_2}{\partial x_1} + \frac{\partial u_3}{\partial x_1}\frac{\partial u_3}{\partial x_1}\right) \qquad (2.42)$$

Since u_1 and u_2 are zero:

$$\varepsilon''_{11} = \frac{1}{2}\left(\frac{\partial u_3}{\partial x_1}\frac{\partial u_3}{\partial x_1}\right) = \frac{1}{2}\left(\frac{\partial u_3}{\partial x_1}\right)^2$$

$$= \frac{1}{2}\left[\frac{\pi M x_3}{RL}*\cos\left(\frac{\pi M x_1}{L}\right)*\sin\left(\frac{N x_2}{2R}\right)*Q\right]^2$$

Similarly:

$$\varepsilon''_{22} = \frac{1}{2}\left(\frac{\partial u_3}{\partial x_2}\right)^2 = \frac{1}{2}\left[\frac{N x_3}{2R^2}*\sin\left(\frac{\pi M x_1}{L}\right)*\cos\left(\frac{N x_2}{2R}\right)*Q\right]^2$$

$$\varepsilon''_{33} = \frac{1}{2}\left(\frac{\partial u_3}{\partial x_3}\right)^2 = \frac{1}{2}\left[\sin\left(\frac{\pi M x_1}{L}\right)*\sin\left(\frac{N x_2}{2R}\right)*\frac{Q}{R}\right]^2$$

$$\varepsilon''_{12} = \frac{1}{2}\left(\frac{\partial u_3}{\partial x_1}\frac{\partial u_3}{\partial x_2}\right) = \frac{\pi M N x_3^2}{16R^3 L}*\sin\left(\frac{2\pi M x_1}{L}\right)*\sin\left(\frac{N x_2}{R}\right)*Q^2 \qquad (2.43)$$

$$\varepsilon''_{13} = \frac{1}{2}\left(\frac{\partial u_3}{\partial x_1}\frac{\partial u_3}{\partial x_3}\right) = \frac{\pi M x_3}{4R^2 L}*\sin\left(\frac{2\pi M x_1}{L}\right)*\sin^2\left(\frac{N x_2}{2R}\right)*Q^2$$

$$\varepsilon''_{23} = \frac{1}{2}\left(\frac{\partial u_3}{\partial x_2}\frac{\partial u_3}{\partial x_3}\right) = \frac{N x_3}{8R^3}*\sin^2\left(\frac{\pi M x_1}{L}\right)*\sin\left(\frac{N x_2}{R}\right)*Q^2$$

For the nonlinear components we have complete tensors. The tensor of nonlinear components of incremental strains is:

$$\varepsilon''_{ij} = \begin{bmatrix} \varepsilon''_{11} & \varepsilon''_{12} & \varepsilon''_{13} \\ \varepsilon''_{12} & \varepsilon''_{22} & \varepsilon''_{23} \\ \varepsilon''_{13} & \varepsilon''_{23} & \varepsilon''_{33} \end{bmatrix} \qquad (2.44)$$

The associated stress tensor, again obtained by constitutive relations, is:

$$\sigma''_{ij} = \begin{bmatrix} \sigma''_{11} & \sigma''_{12} & \sigma''_{13} \\ \sigma''_{12} & \sigma''_{22} & \sigma''_{23} \\ \sigma''_{13} & \sigma''_{23} & \sigma''_{33} \end{bmatrix} \qquad (2.45)$$

According to Equation 2.29, even though the nonlinear component tensors are complete, the individual terms only participate in the total potential energy when multiplied by their fundamental path stress-strain counterparts. For example, ε''_{22} appears in the total potential energy multiplied by σ^F_{22}, which was defined as zero, therefore the energetic contribution of the term as a whole is zero.

After eliminating all the terms that are made zero by the assumptions made in the fundamental path and incremental displacement field definitions, the eigenvalue problem is reduced to the seven-term equation:

$$\int_V (\sigma'_{33}\varepsilon'_{33} + 2\sigma'_{13}\varepsilon'_{13} + 2\sigma'_{23}\varepsilon'_{23})dV + \Lambda \int_V \sigma^F_{11}\varepsilon''_{11}dV$$
$$+ \Lambda \int_V (\sigma''_{11}\varepsilon^F_{11} + \sigma''_{22}\varepsilon^F_{22} + \sigma''_{33}\varepsilon^F_{33})dV = 0 \qquad (2.46)$$

The unknowns in this problem are: the eigenvalue, i.e. the load parameter Λ, which is the load multiplier, and the eigenvector, represented in this simple case by the radial displacement generalized coordinate Q.

2.5 MATERIAL MODELS AND GEOMETRIES

The material models utilized were linear-elastic and isotropic, defined by the elastic modulus (also known as Young's modulus, or E), which is the ratio of stress to

strain, and Poisson's ratio, *v*, the ratio of lateral strain to axial strain caused by a load in the axial direction. Isotropy indicates that the material properties are the same in all directions, which allows the material to be defined by only two constants (further discussion of material definitions and constants can be found in Malvern, 1969).

Three cylindrical geometries were used in this work, with radius of 100 mm in all cases and heights of 50, 70 and 90 mm. For easy reference, the material and geometry combinations presented in this work will henceforth be referred to by the Case ID presented in Table 2.1.

Table 2.1. Case ID's for material model/geometry combinations.

Case ID	Elastic Modulus [Mpa]	Poisson's Ratio	Height [mm]	Radius [mm]
Case .05-50	7	0.05	50	100
Case .15-50	7	0.15	50	100
Case .25-50	7	0.25	50	100
Case .35-50	7	0.35	50	100
Case .45-50	7	0.45	50	100
Case .05-70	7	0.05	70	100
Case .15-70	7	0.15	70	100
Case .25-70	7	0.25	70	100
Case .35-70	7	0.35	70	100
Case .45-70	7	0.45	70	100
Case .05-90	7	0.05	90	100
Case .15-90	7	0.15	90	100
Case .25-90	7	0.25	90	100
Case .35-90	7	0.35	90	100
Case .45-90	7	0.45	90	100

The cases are named by the Poisson's ratio/solid height combination. A single value of elastic modulus is presented in Table 2.1; however, this is a consequence of the

investigation, which revealed that Young's modulus does not affect the stability behavior of the solids (see Section 2.6.1). For any value that might have been used, the results pertinent to our investigation would have remained the same.

2.6 RESULTS

With the incremental displacements set by Equation 2.38, several deformed shapes (or *modes*) were utilized, and the associated eigenvalues obtained by solving Equation 2.46 for each case. Since Equation 2.38 is defined in terms of sine waves, the modes were described by the number of circumferential and vertical "waves" in displacement. Figure 2.6 shows 3D plots of cylinders with deformed shapes according to the number of vertical waves, M, and circumferential waves, N, set to various values. Figure 2.6 (b), the mode shape for M = 2 and N = 2, corresponds to the function plot shown previously in Figure 2.5. The black lines in the figures represent the internal plot grids and are for visual effect only. They do not indicate a finite element mesh.
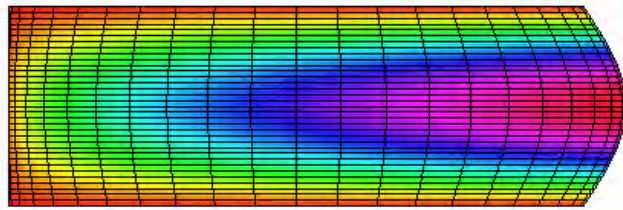
(a)
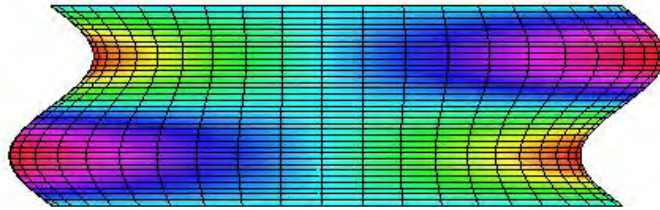
(b)
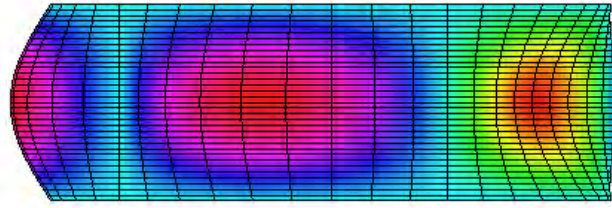
(c)
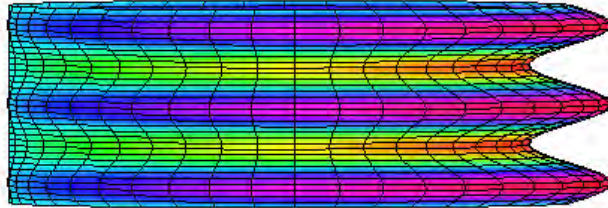
(d)

Figure 2.6. Mode shape for (a) M = 1, N = 1; (b) M = 2, N = 2;
(c) M = 1, N = 5; (d) M = 5, N = 1.

2.6.1 Influence of Material Properties

Several analyses were performed in order to test the influence of the material properties on the eigenvalues obtained. A fact that quickly became apparent was that the value for elastic modulus did not affect the eigenvalue obtained from the analysis. Figure 2.7 demonstrates this fact for several material/mode/geometric cases. It must be noted that strictly speaking, the eigenvalue obtained in the eigenvalue extraction analyses performed is a load value for the variable P. However, since buckling manifests as a geometric phenomenon, in this thesis we have chosen to observe the associated displacement in the top surface where the load acts, for easy comparison between different material cases. The displacements are calculated from elasticity equations (Equation 2.31) using the obtained load eigenvalue.

39

(a)

(b)

40
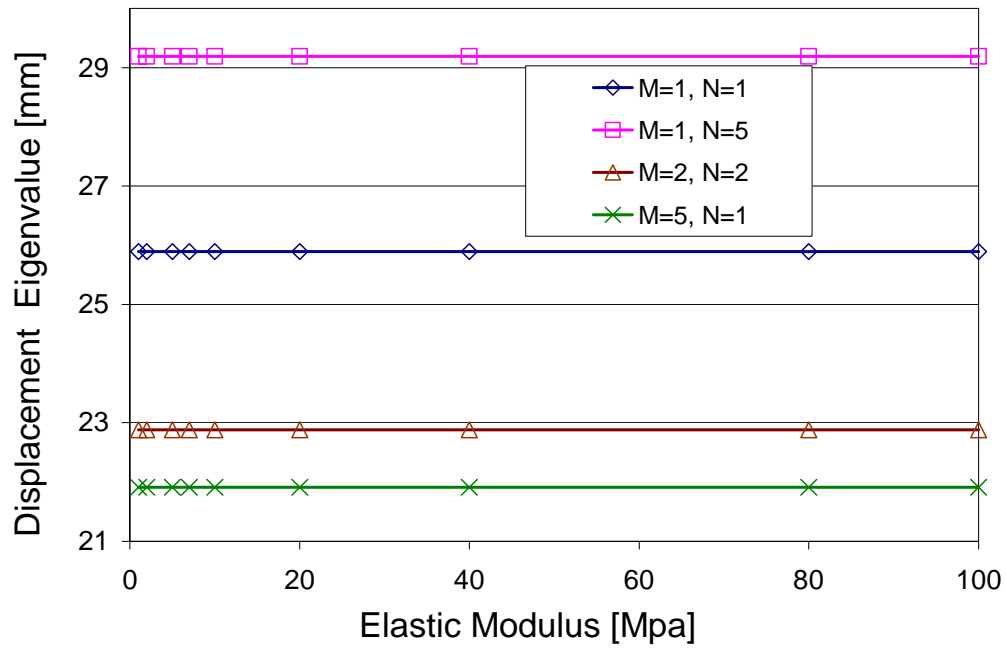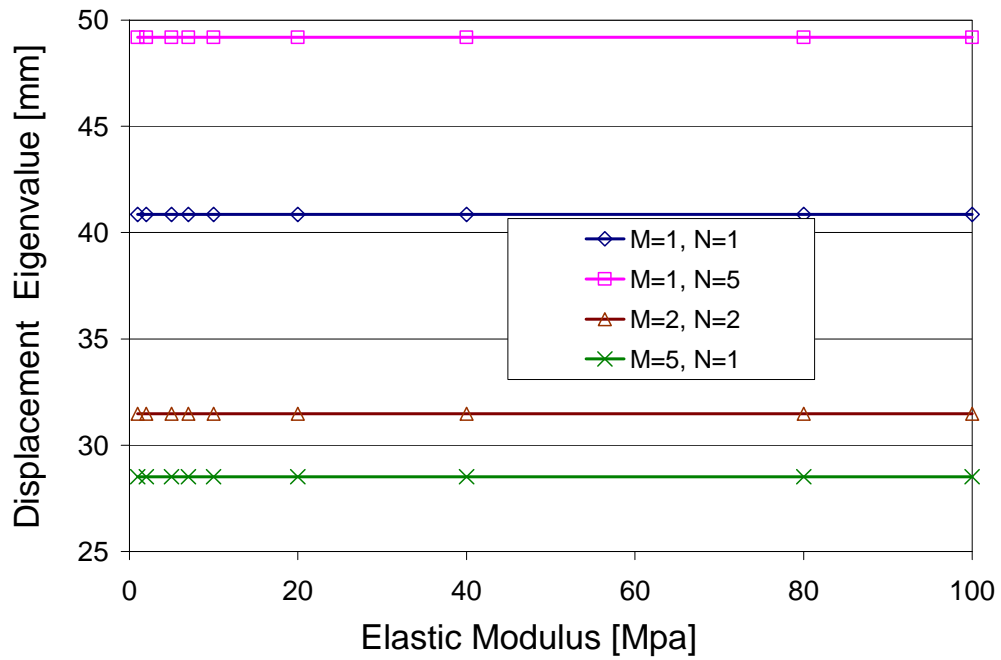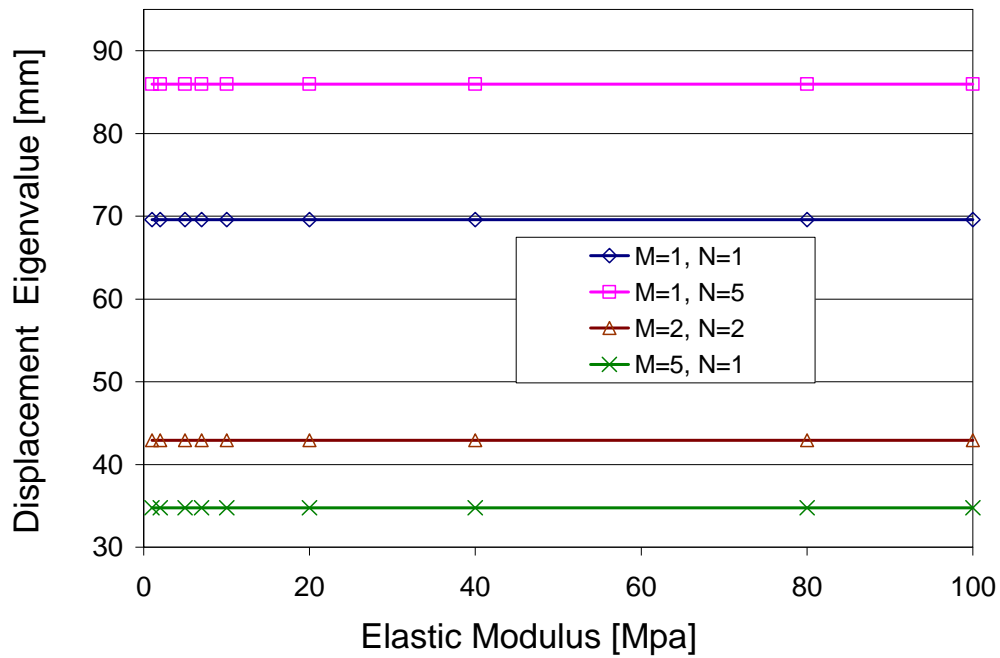
Figure 2.7. Constancy of displacement eigenvalue with increasing elastic modulus
(a) Case .15-50 (b) Case .25-70 (c) Case .35-90.

Although Figure 2.7 does not show results for every eigenmode and case, the displacement eigenvalue remained the same for all values of elastic modulus for each combination of geometry and Poisson's ratio.

The effects of varying Poisson's ratio were also studied. Poisson's ratio, or ν, is defined as the ratio of lateral strain to axial strain when the axial direction is loaded, and can be used as a measure of compressibility in linear elastic materials. For these materials, the theoretical range of ν is from 0 to 0.5. A perfectly incompressible material would have a value of 0.5. For rubber, ν is almost 0.5, while for cork, a material that does not display transverse strains due to the presence of axial strains, ν is close to zero.

(a)

(b)
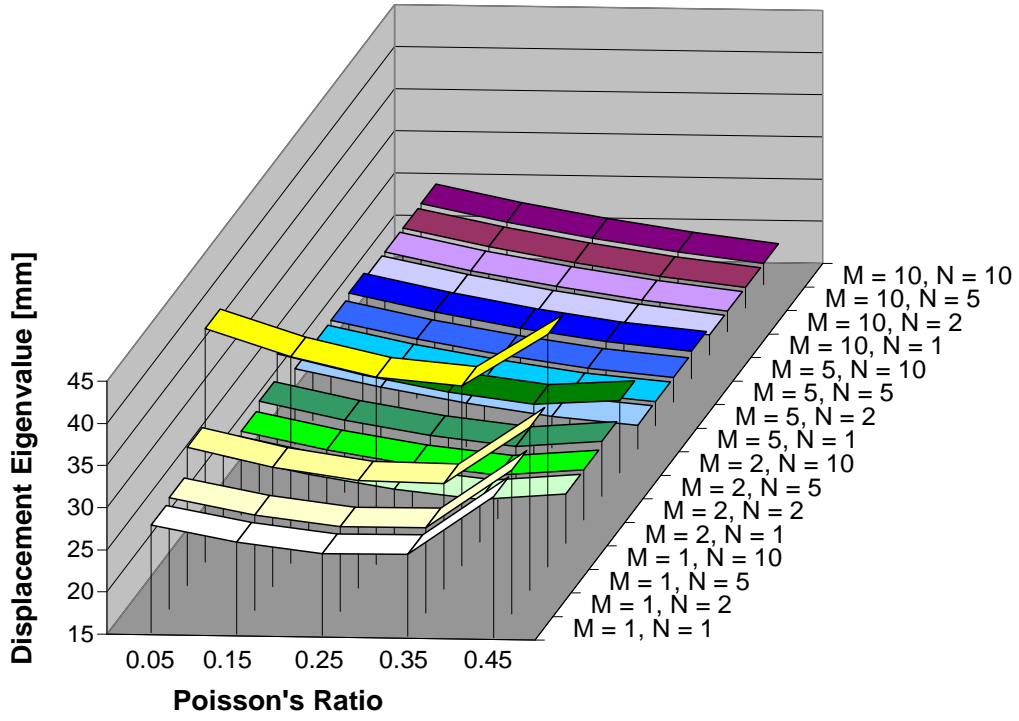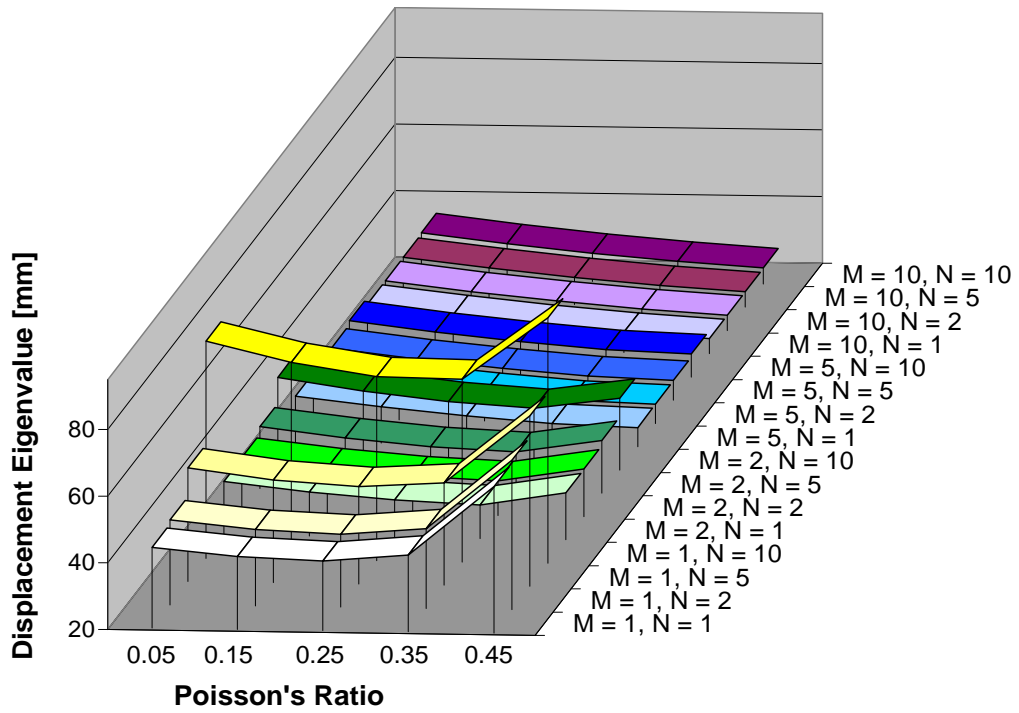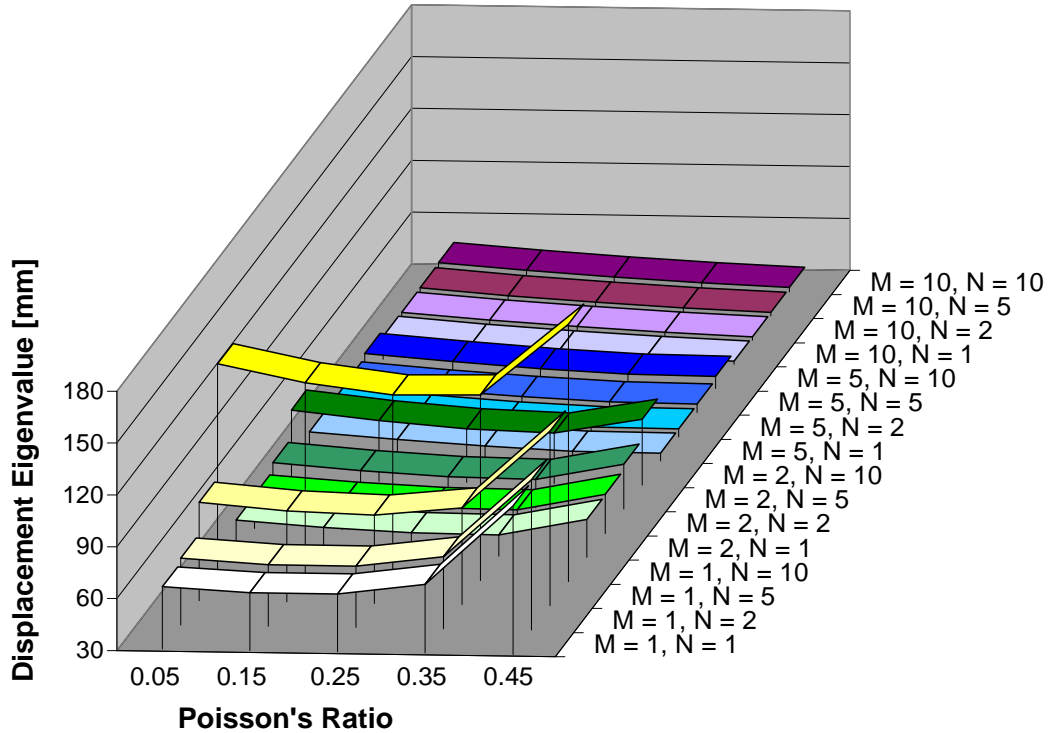
Figure 2.8. Displacement eigenvalue versus Poisson's ratio for various M and N:
(a) Height = 50 mm; (b) Height = 70 mm; (c) Height = 90 mm.

Figure 2.8 shows the eigenvalues obtained for the three geometric cases for all the eigenmodes utilized (the combinations of M = 1, 2, 5, 10 and N = 1, 2, 5, 10), for five values of Poisson's ratio. As Figure 2.8 demonstrates, the eigenvalue behavior with respect to Poisson's ratio is not constant. In addition, the variation behavior is also not monotonic, but is instead dependent on the incremental mode shape applied. This is illustrated in Figure 2.9 and Figure 2.10, which show the eigenvalues obtained for the three geometric cases for M = 10, N = 1 and M = 2, N = 2. The figures show the results directly as obtained and also normalized with respect to the corresponding height for each case.
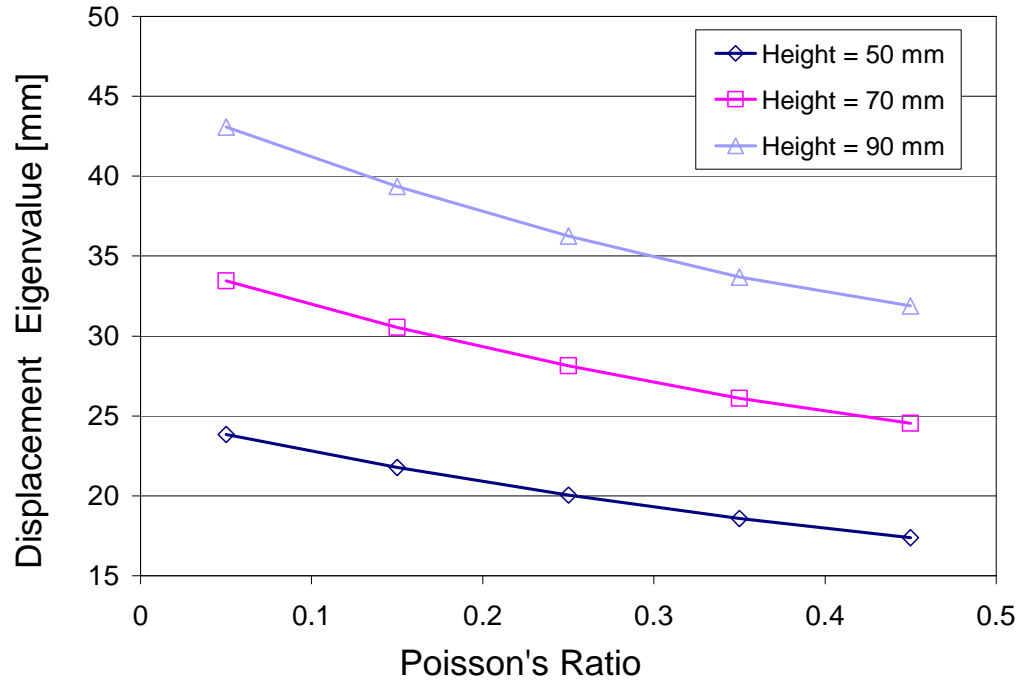
(a)
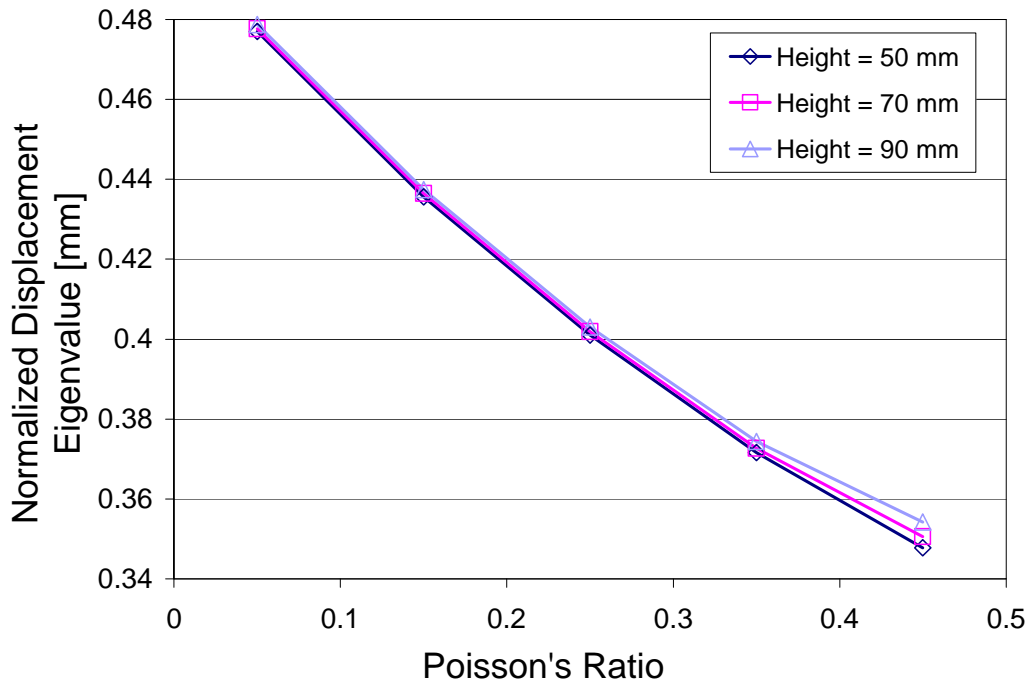
(b)

Figure 2.9. Displacement eigenvalue versus Poisson's Ratio for M=10, N=1;
(a) Direct results, (b) Results normalized with respect to height.

Notice how the curves for M = 10, N = 1 descend smoothly with increasing Poisson's ratio. When normalized, these curves lie almost on top of each other, which implies that this mode has a similar quantitative effect on each geometry. This is not the case for M = 2, N = 2, which exhibits both a U-shape and differing effects for each geometry.
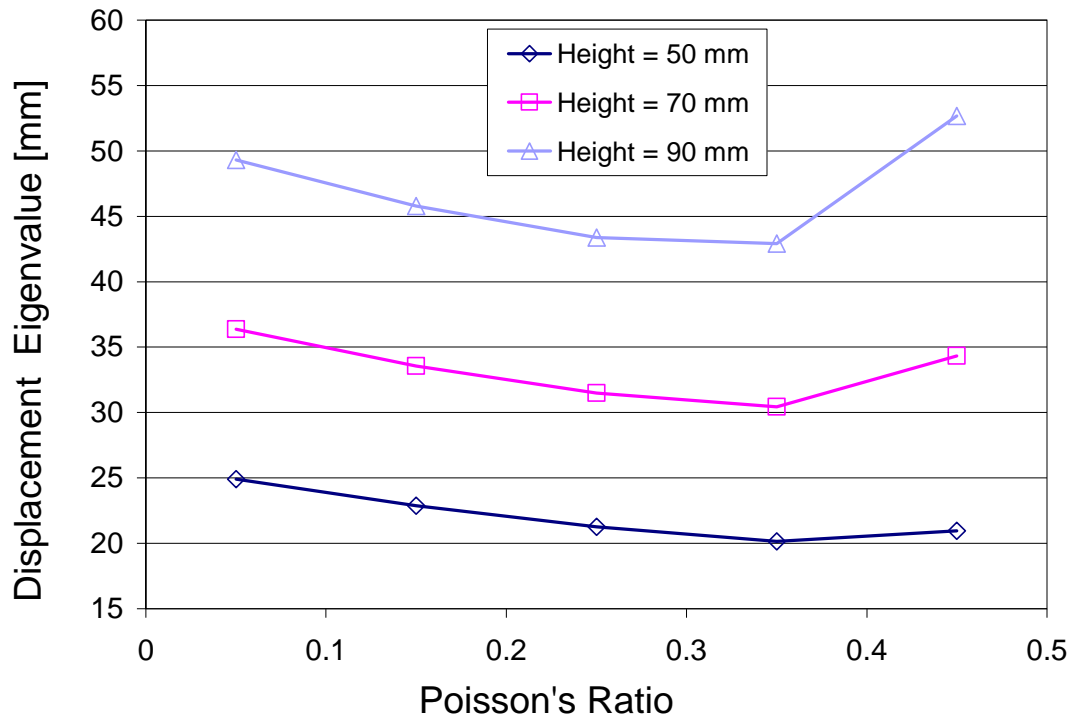
(a)
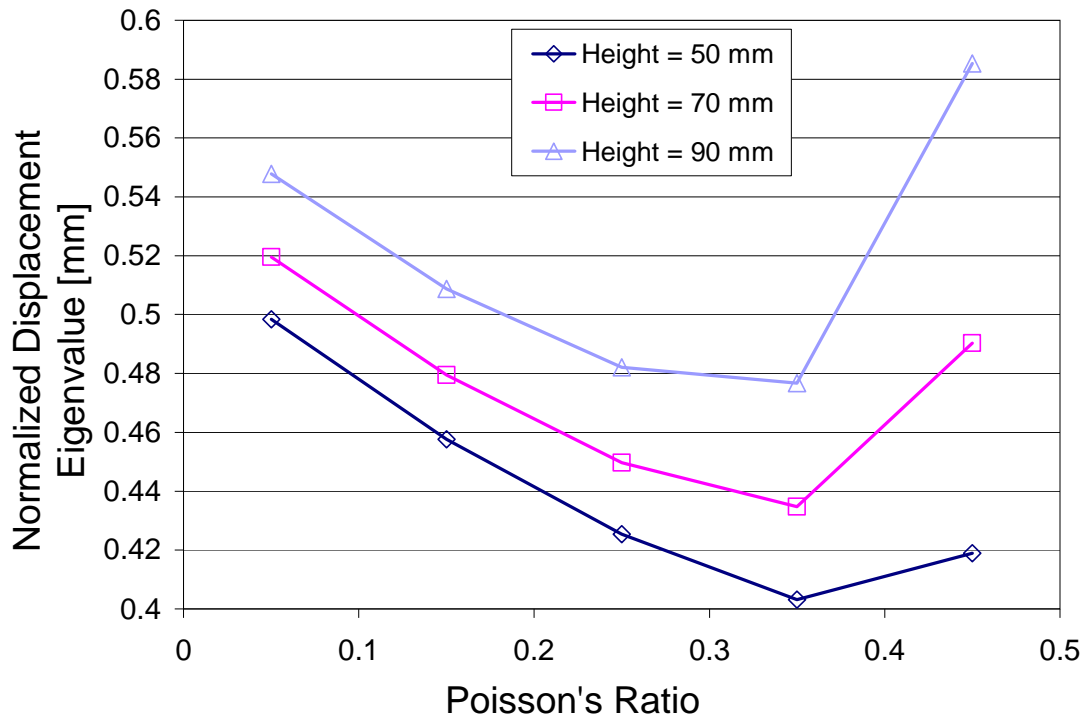
(b)

Figure 2.10. Displacement Eigenvalue versus Poisson's Ratio for M=2, N=2;
(a) Direct results, (b) Results normalized with respect to height.

As can be garnered from the preceding figures, for lower M, the highest eigenvalues correspond to both highest and lowest Poisson's ratio. However, for higher M, the eigenvalue obtained for the same mode and geometry tends to decrease with increasing Poisson's ratio; therefore the curves do not all exhibit the same trend, but are dependent on the shape used for the incremental displacement field.

2.6.2 Results of Eigenvalue Analyses

The associated eigenvalues, in terms of displacement, for each mode were found and plotted for increasing values of M and N. Figure 2.11 shows the results for all geometric/material cases.
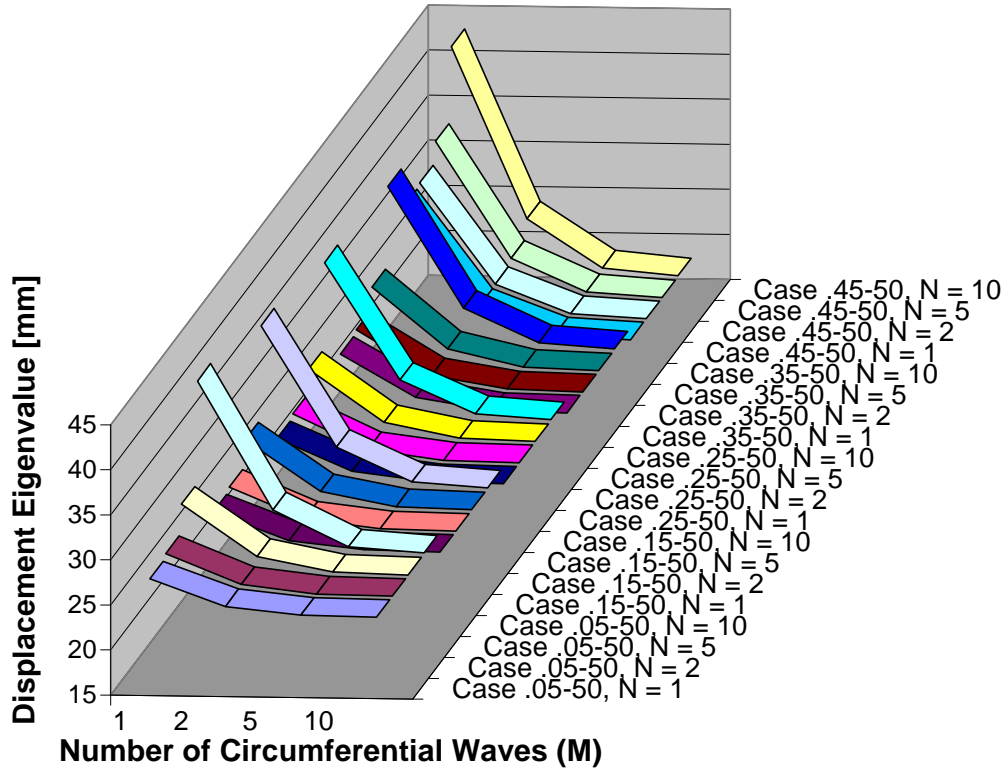
(a)
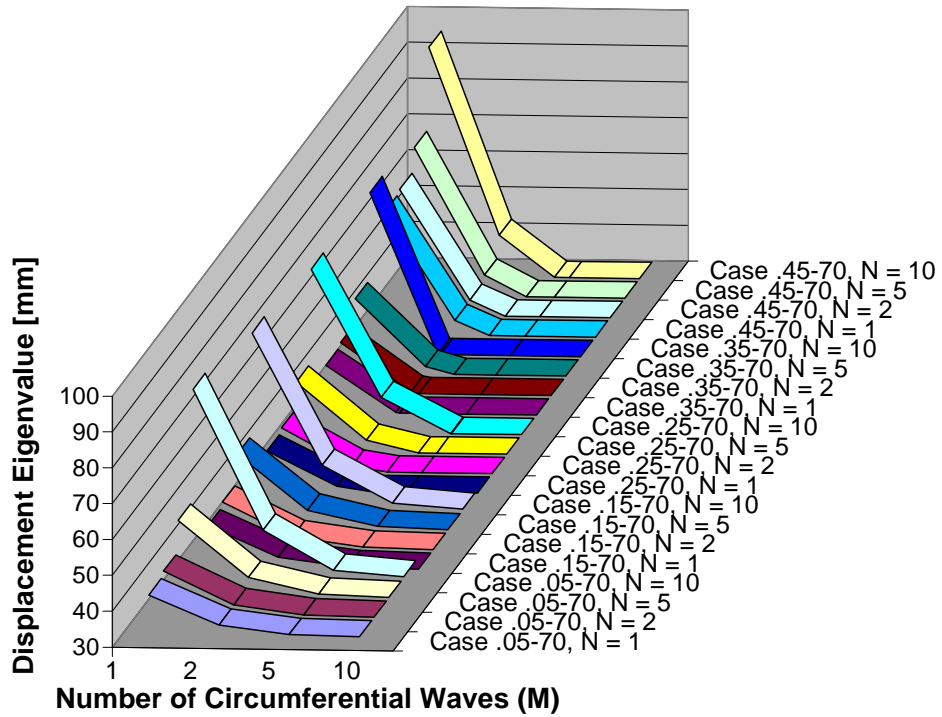
(b)
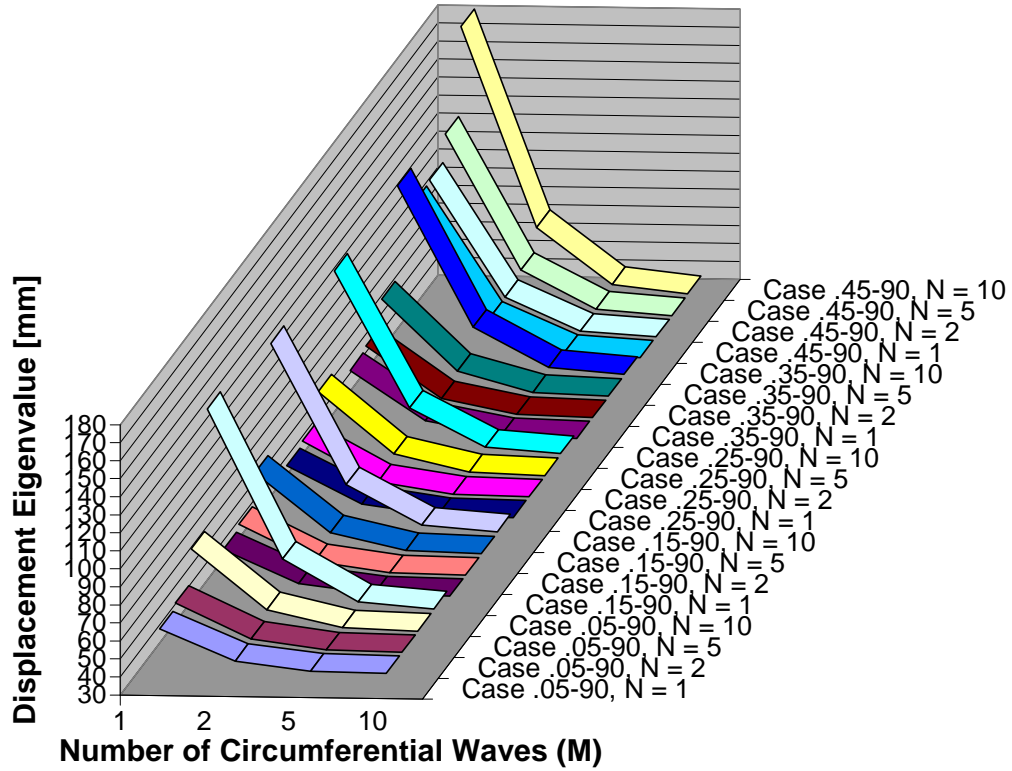
(c)

Figure 2.11. Displacement Eigenvalue versus M for various N:
(a) Height = 50 mm; (b) Height = 70 mm; (c) Height = 90 mm.

As can be seen from the preceding figures, in all cases the trend is the same: A greater number of vertical waves (M), corresponds to decreasing eigenvalue, while with a greater number of circumferential waves (N) a slight increase in eigenvalue is obtained. The results display an asymptotic trend with increasing M. Though not shown on the plots, this behavior was seen to extend to infinity, and held for all geometric/material cases. Figure 2.12 illustrates the behavior two-dimensionally for three geometric/material cases.
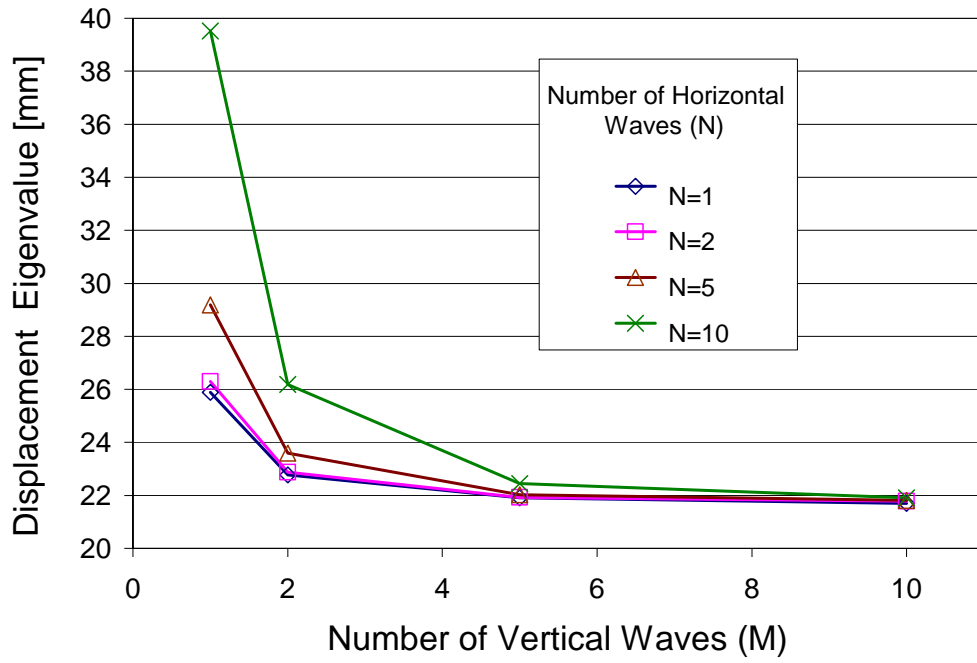
(a)
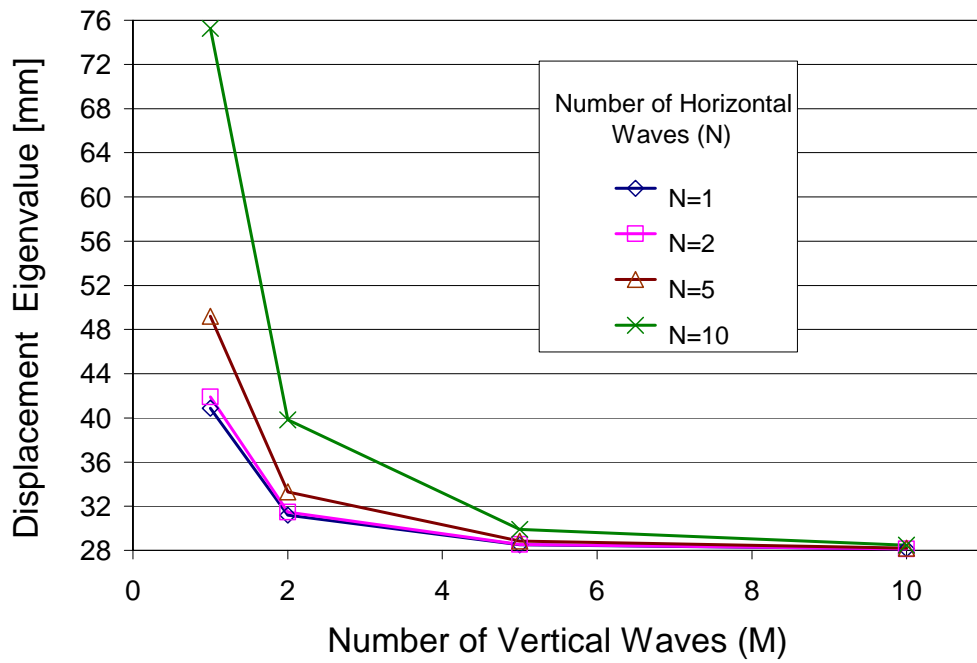
(b)
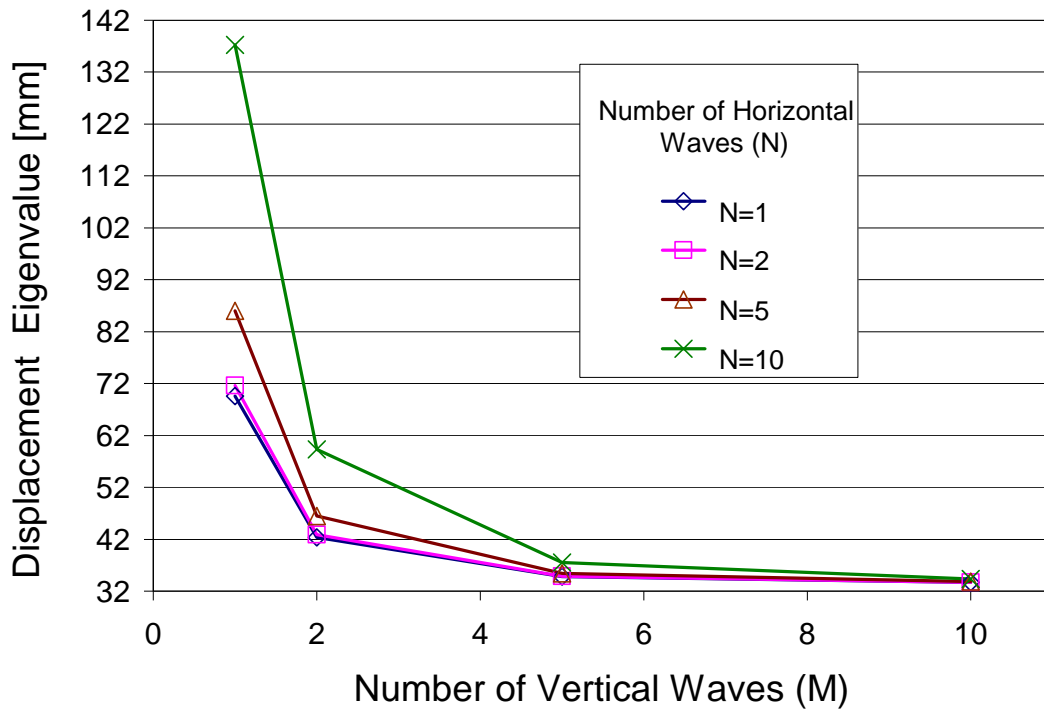
(c)

Figure 2.12. Displacement Eigenvalue versus M for various N, (a) Case .15-50;
(b) Case .25-70; (c) Case .35-90.

Again, we can see that the behavior is the same for the different material/geometry cases shown. Note that some of these displacement eigenvalues obtained, such as the cases for M=1, N=10 on the 70 mm and 90 mm tall cylinders, are larger than the initial solid heights, and therefore cannot occur.

2.7 CONCLUSIONS

From the simplified analytical model presented in this chapter, it was observed that the eigenvalues are the same for all the values of elastic modulus (for the same geometry). This may be surprising at first glance, but it is not counterintuitive if thought of in terms of displacements: for larger modulus values, more load is required to reach

the same displacement level. However, since the reference Poisson's ratio is unchanged, the deformed shape must be equal to that of a material of lesser modulus for the same displacement level – including the critical displacement.

While varying only Poisson's ratio, the eigenvalues were seen to depend strongly on the number of vertical waves M: for lower M, the behavior is concave-upward increasing with Poisson's ratio, with the highest values corresponding to the highest and lowest values of Poisson's ratio. For higher M, the behavior is concave-upward, decreasing with Poisson's ratio. Modes with higher N display the same shapes for the same M, only at higher displacement eigenvalue levels.

With respect to the mode shapes, it is seen that increasing M decreases the eigenvalue, while increasing N increases the eigenvalue. M has a much stronger destabilizing influence than N has a stabilizing influence. It comes as a surprise, in light of common experience in stability problems, that increasing M *always* has a destabilizing effect, since the usual behavior of buckling systems is that a particular mode will correspond to a lowest eigenvalue. The behavior observed in our models was asymptotic with increasing M. This would indicate that the lowest displacement eigenvalue corresponds to an infinite number of waves in the vertical direction – an intuitively unlikely result associated with the simple approximation adopted.

It is important to note that the magnitudes of displacement for buckling computed are very large for all cases: nearly a third of the total cylinder heights is the minimum for all cases. This indicates that indeed it would be extremely difficult to produce buckling on a structural solid made with constructional materials, if such were found to withstand the large strains. However, the problem would be more realistic in solids such as

biological tissues and foams, which may have large strains and still remain elastic. Most importantly, it is proved that buckling of a solid under compression is a structural possibility, unlike certain systems such as cylindrical shells under internal outward pressure and compression at the top of the shell.

The accuracy of the results reported in this chapter is still to be validated. For this purpose, a more refined method for a solution is utilized in the next chapter.

FINITE ELEMENT ANALYSES OF ELASTIC 3D SOLIDS

3.1 INTRODUCTION

Investigations inside of a solid pose an obvious problem, to wit, finding out what goes on inside the solid during a loading cycle. In Chapter 2, we carried out eigenvalue extraction analyses to determine the bifurcation points for various cylindrical solids. In doing so, we introduced several assumptions, for example the linearity of the fundamental path. We also used only one degree of freedom, the radial displacement generalized coordinate Q. More refined solutions to the solid buckling problem are presented in this chapter. Finite element models, with multiple degrees of freedom in all three dimensions, are used to obtain the bifurcation critical points. Nonlinear incremental methods facilitated by finite elements also allow limit points to be found.

In this chapter, three types of analyses are presented: linear analyses, buckling analyses and geometrically nonlinear analyses. The linear analyses serve as a comparison for the linear fundamental path assumed in Chapter 2 and as a reference point for the

behavior of the system. The buckling analyses are used to verify the results obtained using the incremental displacement formulation, both eigenvalues and mode shapes. Finally, the nonlinear analyses carried out allow the limit point behavior to be explored, as well as the degree of linearity or otherwise in the systems studied. The results from all types are compared.

3.2 MATERIAL MODELS, GEOMETRIES AND MESHES

The finite element eigenvalue extraction analyses were performed with the general purpose finite element program ABAQUS (Hibbit et al, 2003). The models had the same properties used previously on Chapter 2, both material and geometry-wise. A finite element mesh consisting of 20-node brick elements (identified as C3D20 in ABAQUS) was used. Active degrees of freedom for these elements are the displacements u_1, u_2 and u_3. The assumed boundary conditions were fixed at the bottom surface of the cylinder and displacements restrained at the top surface in the $x_1 x_2$ plane (i.e., u_1 and u_2). Eigenvalue and nonlinear incremental analyses were performed as displacement controlled experiments, applying a negative displacement at the top surface in the x_3 direction so as to cause compression.

For each of the three geometries investigated, an associated finite element mesh was constructed. The details of the meshes are given in Table 3.1.

Table 3.1. Mesh details for geometries utilized.

Geometry	Number of Elements	Number of Nodes	Characteristic Element Length
R=100mm H=50mm	2,070	10,077	9.14
R=100mm H=70mm	2,898	13,585	9.14
R=100mm H=90mm	3,726	17,093	9.14

3.3 LINEAR ANALYSES

3.3.1 Introduction

A geometrically linear analysis is a usual first step in computational mechanics due to the low computational cost and assumptions of small rotations and strains. For the cases studied, linear analyses also represent the linear fundamental path described in Chapter 2, except for the boundary conditions (recall that for simplicity, the linear fundamental path was defined as having no constraints in the top or bottom planes - see Chapter 2, Section 2.4.1). In the finite element analyses, as well as the incremental displacements in Chapter 2, the top and bottom planes are constrained horizontally. The reasons for this are that in a practical reality an unbounded plane condition would be rather impossible to achieve; also, not having any constraints in the planes of the solid creates mathematical difficulties for the finite element solver.

Figure 3.1 shows the vertical top displacement versus circumferential displacement at midheight for all material and geometry cases. Linear analyses have no "endpoint", as mathematically they continue forever, so the plots are presented only up to

a top displacement equal to half the solid height. The dashed lines indicate that the displacements would continue on with the same slope. As can be seen, the materials with lower Poisson's ratio have steeper slopes, due to the lower radial displacement response.
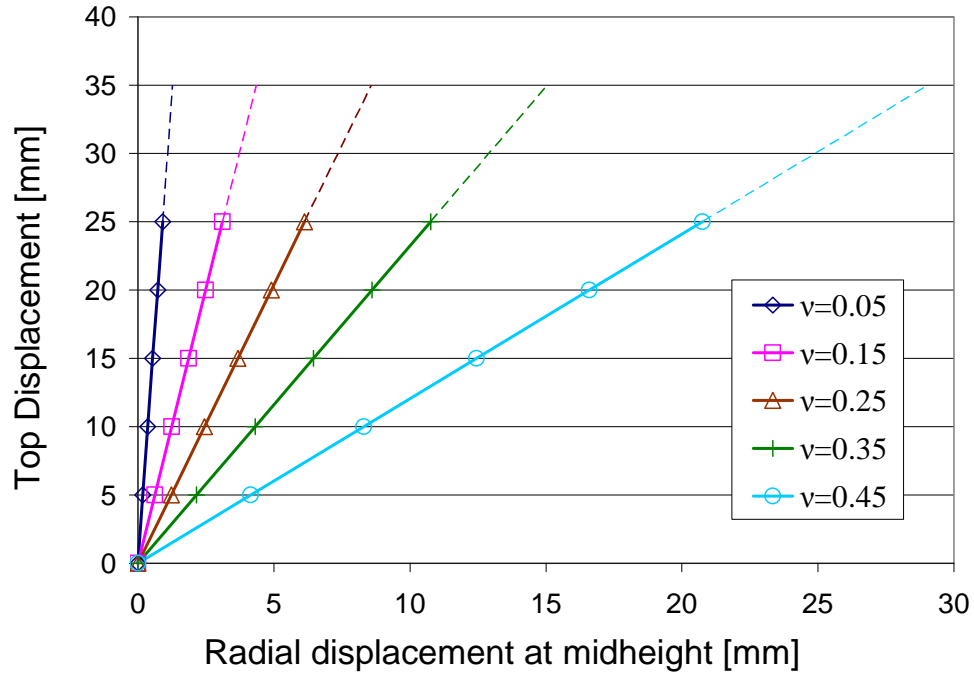
(a)
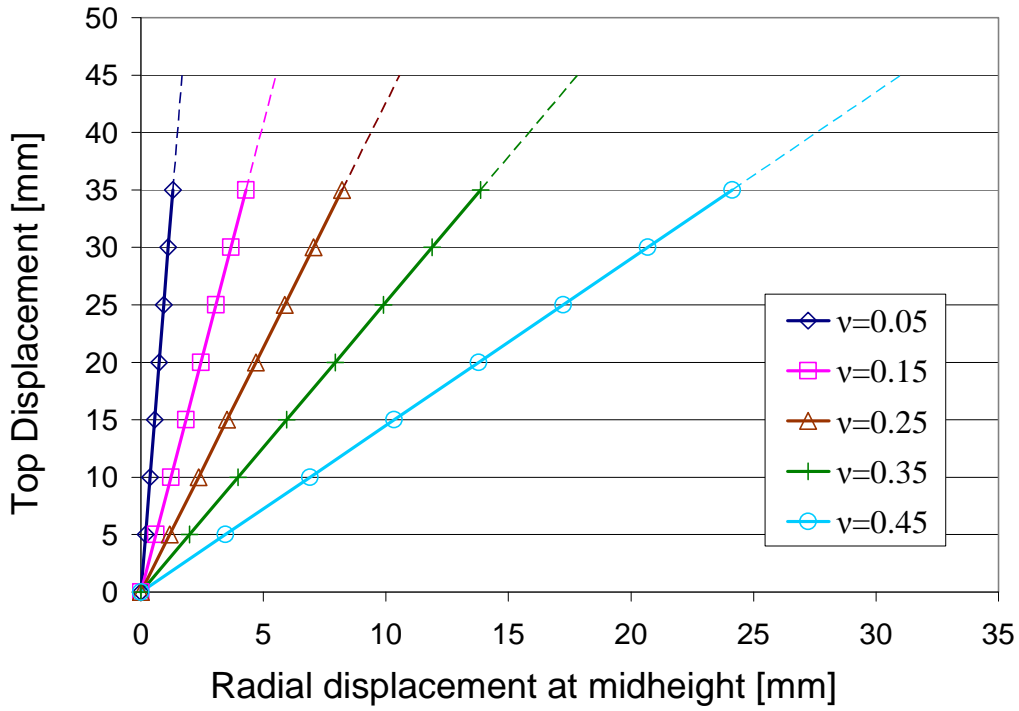
(b)
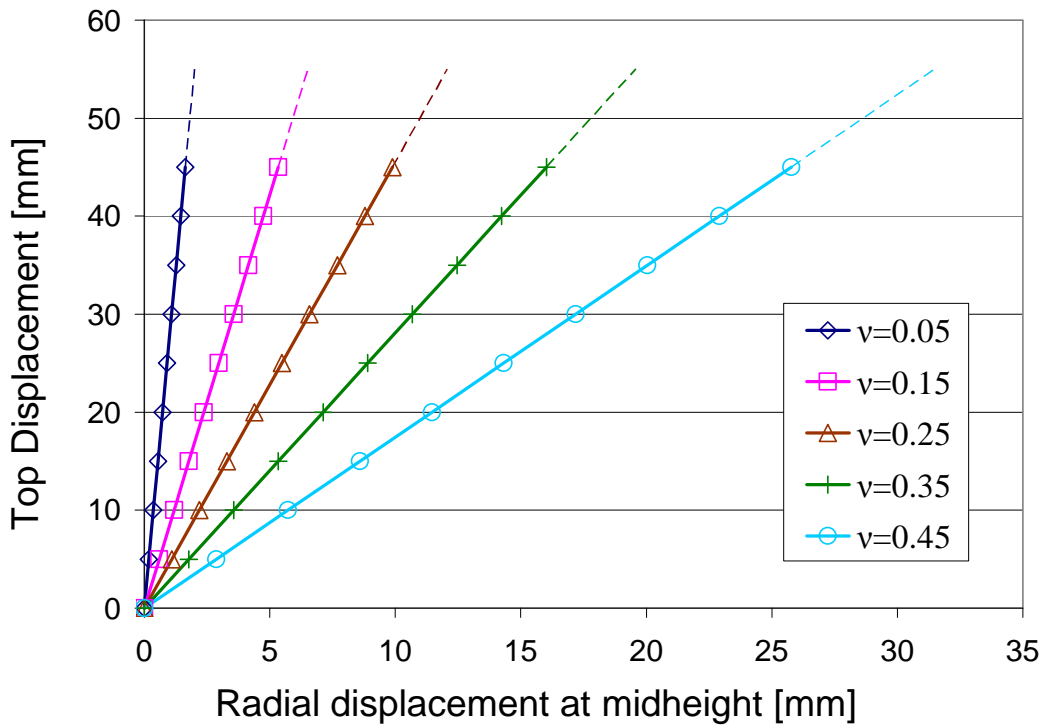
(c)

Figure 3.1. Top displacement versus radial displacement for linear analyses:
(a) Height = 50 mm; (b) Height = 70 mm; (c) Height = 90 mm.

Finite elements allow results inside the solid to be investigated. Cutting into a deformed solid, we can view the displacement distribution. Figure 3.2 shows a typical quarter section in a linear analysis. The displacement U1 represents radial displacement.
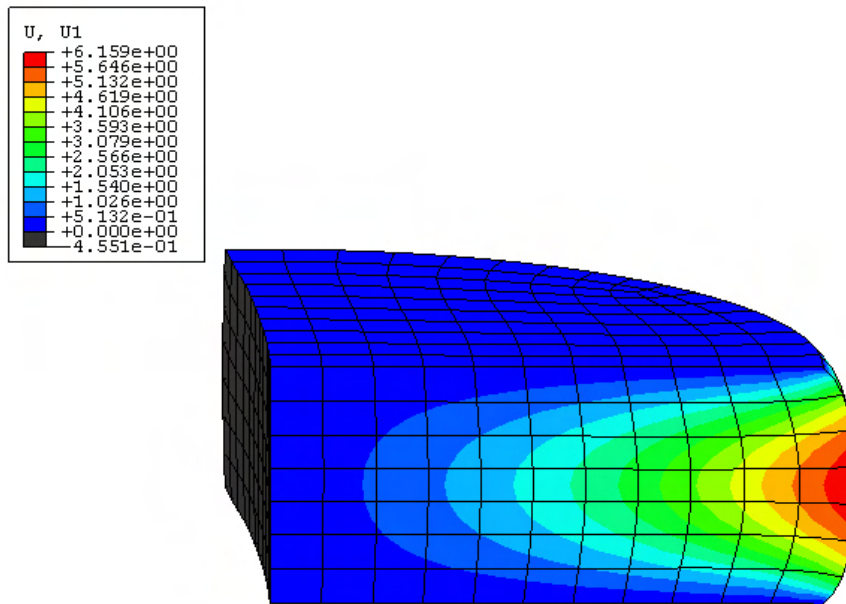
Figure 3.2. Radial displacements in quarter section of solid.

As can be seen from the color bands, which are not equal in size, the radial displacements do not behave linearly with respect to the radial coordinates. However, the distribution is dependent on Poisson's ratio of the material used. Figure 3.3 displays the radial displacements, normalized to the maximum displacement, versus the radial distance from the center of the solid for all geometry and material cases.
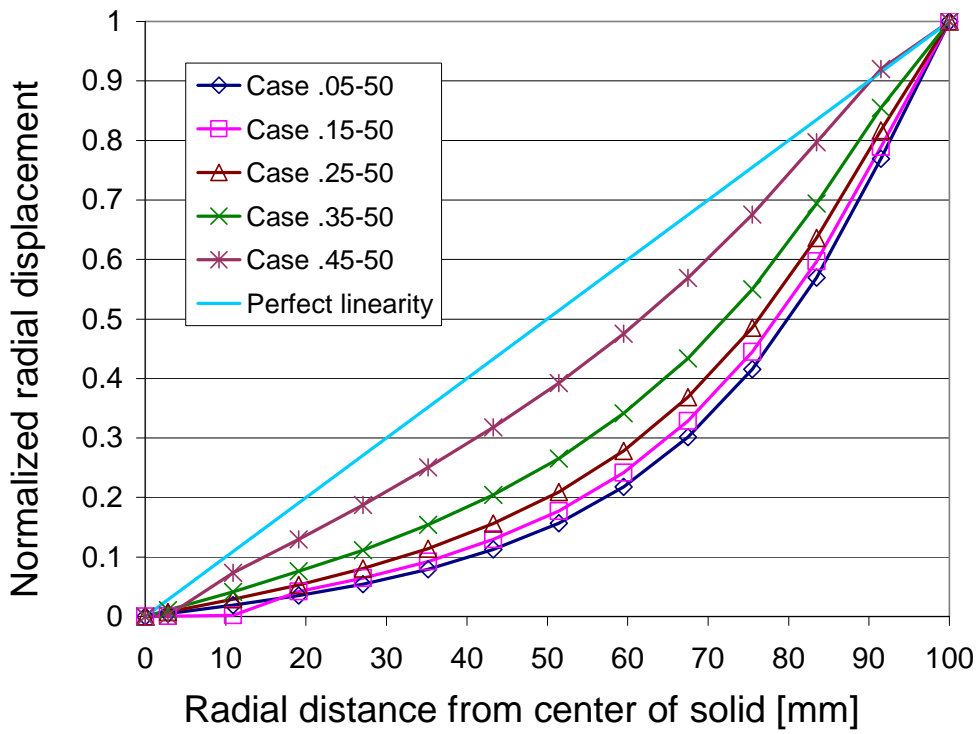
(a)
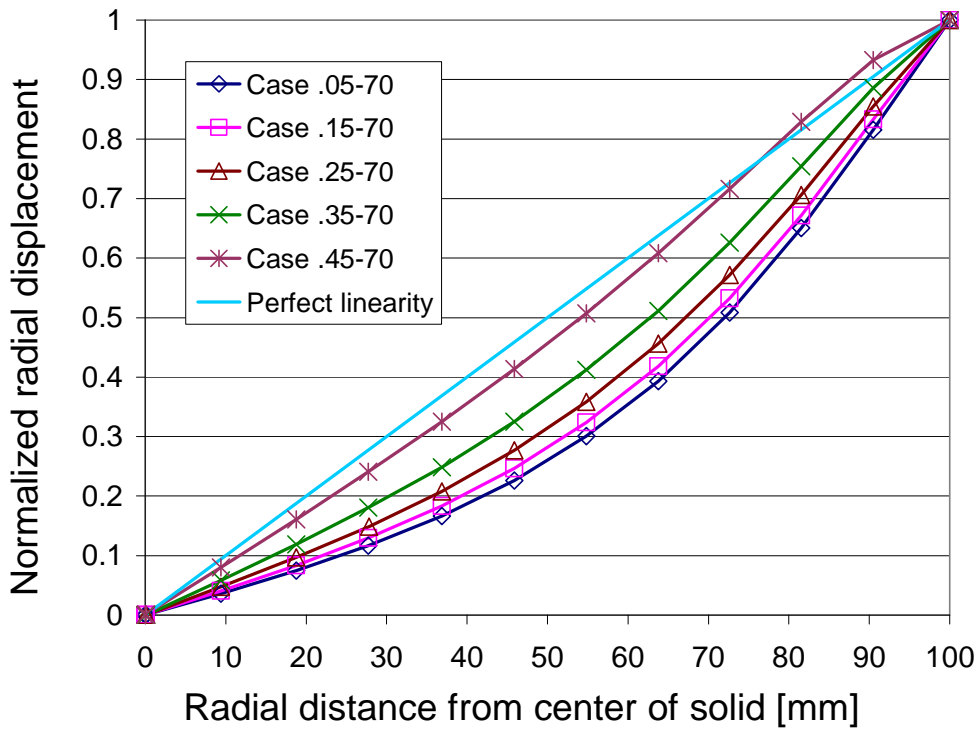
(b)
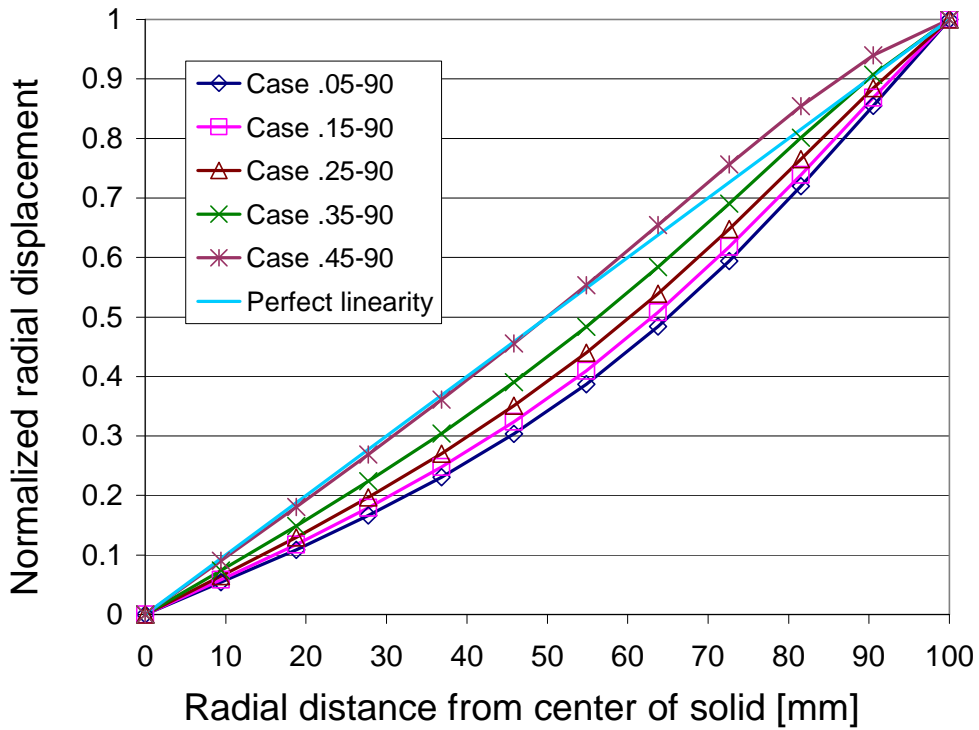
(c)

Figure 3.3. Normalized radial displacements versus radial distance:
(a) Height = 50 mm; (b) Height = 70 mm; (c) Height = 90 mm.

While the radial displacement distribution proved to be nonlinear, the vertical displacements did display linear behavior in all cases, with the maximum displacement at the top of the solid and zero displacement at the bottom as per the boundary condition. Figure 3.4 shows the typical vertical displacement distribution in color bands, where red represents the maximum vertical displacement, dark blue the minimum.
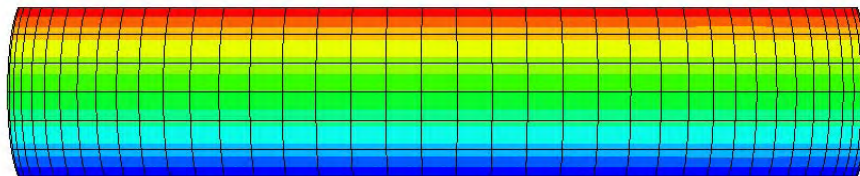
Figure 3.4. Normalized radial displacements versus radial distance.

3.4 EIGENVALUE BUCKLING ANALYSES

In order to confirm the predicted findings of buckling of a linear elastic solid, a linear eigenvalue extraction procedure was performed with finite elements. The buckling analyses that can be performed in ABAQUS are also linear eigenvalue extraction analyses. The analyses were displacement controlled, therefore the eigenvalues obtained were values for the top displacement when the cylinder buckles. The analysis also yields mode shapes, which are the deformed shape the solid is predicted to take when the buckling load is reached. Mode shapes are usually different from the shapes seen from standard load-displacement effects. Figure 3.5 shows the typical deformed shape of a solid cylinder under compression from a linear analysis. Note that the circumference deformation has a characteristic "barrel" shape. In contrast, Figure 3.6 shows a buckling mode for the same cylinder. The buckling mode shape shows highly irregular circumferential displacements. This is one of the possible shapes a solid cylinder could take if a buckling load were reached. The mode shapes given by ABAQUS as output are normalized to the greatest displacement, meaning the largest displacement magnitude is equal to 1.
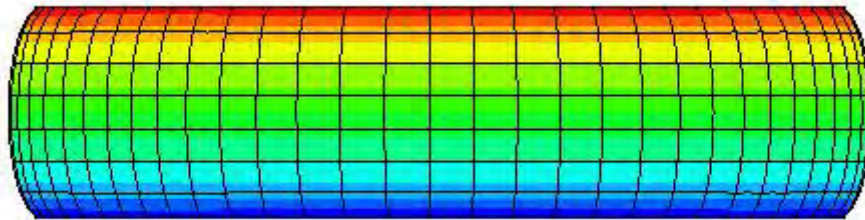
Figure 3.5. Typical barrel deformed shape of solid cylinder from linear analysis.
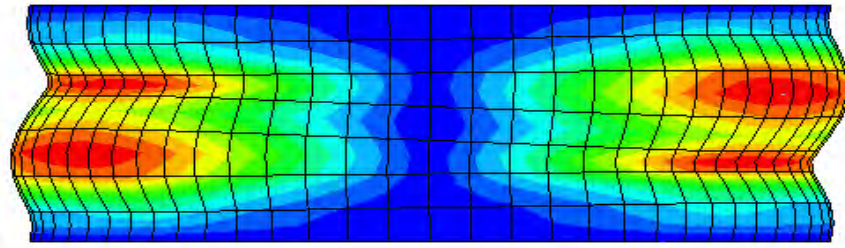
Figure 3.6. Mode shape obtained from eigenvalue extraction analysis.

3.4.1 Influence of Material Parameters on Eigenvalues and Eigenmodes

As discussed previously in Chapter 2, the elastic modulus was observed to play no part in the displacement obtained with an eigenvalue analysis. This was confirmed by several finite element eigenvalue extraction analyses. Again, it was found that changing the modulus had no effect on either the eigenvalues or eigenmodes. Figure 3.7 shows the results of eigenvalue extraction analyses when varying the elastic modulus in cases .15-50, .25-70 and .35-90. The flat lines demonstrate the null influence of Young's modulus on the eigenvalues. Though only three sets of results are presented, the same behavior is observed in all cases.
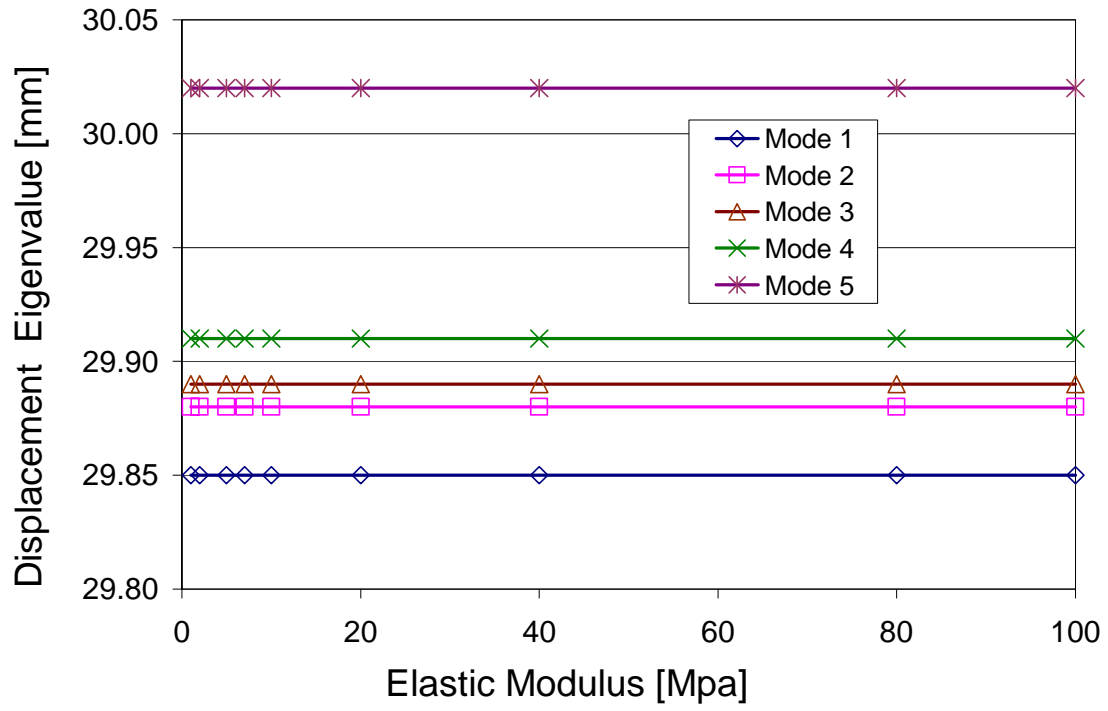
(a)
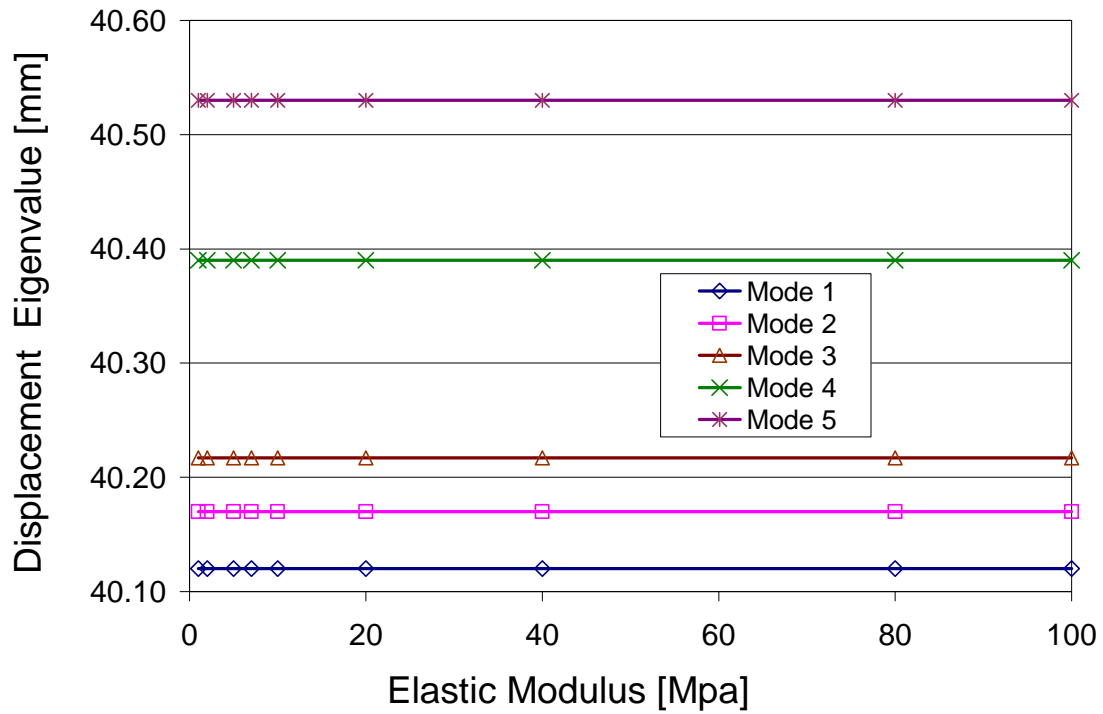
(b)
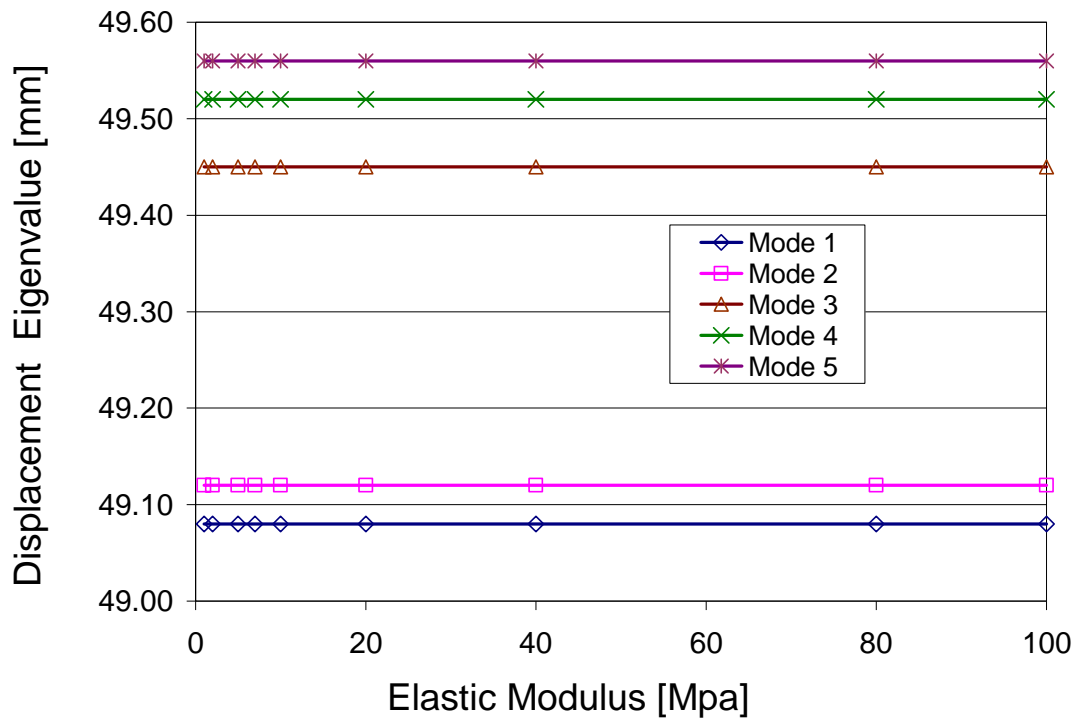
(c)

Figure 3.7. Constancy of displacement eigenvalue with increasing elastic modulus
(a) Case .15-50 (b) Case .25-70 (c) Case .35-90.

The influence of Poisson's ratio on eigenvalues or eigenmodes was also confirmed by performing eigenvalue extraction analyses for varying Poisson's ratio and constant Young's modulus. As Figure 3.8 shows, the eigenvalues decrease nonlinearly with increasing Poisson's ratio. This behavior was also observed in the results from Chapter 2.
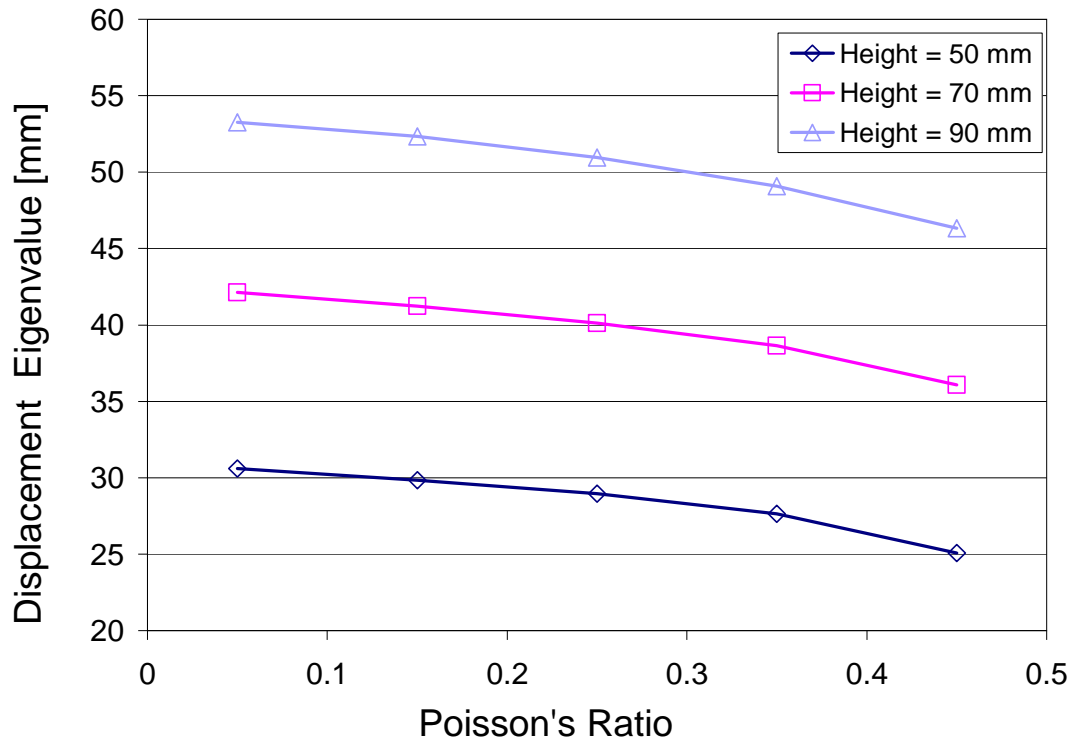
Figure 3.8. Variation of lowest eigenvalue with increasing Poisson's ratio.

3.4.2 Results for Buckling Analyses

Displacement controlled eigenvalue extraction analyses were carried out using ABAQUS. The obtained output consisted of eigenvalues and eigenmodes. Table 3.2 lists the first ten eigenvalues obtained for all the material/geometry cases. The mode numbers correspond to increasing eigenvalues.

Table 3.2. Eigenvalues obtained from finite element analyses.

Displacement Eigenvalues [mm]										
Case ID	Mode 1	Mode 2	Mode 3	Mode 4	Mode 5	Mode 6	Mode 7	Mode 8	Mode 9	Mode 10
.05-50	30.591	30.657	30.663	30.686	30.809	30.814	30.896	31.064	31.194	31.349
.15-50	29.845	29.885	29.887	29.914	30.022	30.025	30.077	30.253	30.337	30.489
.25-50	28.951	28.952	28.969	28.995	29.035	29.039	29.12	29.212	29.342	29.423
.35-50	27.651	27.685	27.721	27.726	27.728	27.797	27.81	27.829	28.008	28.025
.45-50	25.082	25.096	25.116	25.122	25.129	25.177	25.191	25.247	25.255	25.319
.05-70	42.123	42.151	42.215	42.259	42.407	42.459	43.006	43.047	43.276	43.394
.15-70	41.227	41.283	41.304	41.355	41.564	41.609	41.959	42.126	42.185	42.433
.25-70	40.12	40.17	40.217	40.39	40.533	40.562	40.703	40.909	40.978	41.248
.35-70	38.653	38.691	38.87	39.031	39.06	39.077	39.165	39.27	39.292	39.535
.45-70	36.088	36.262	36.283	36.297	36.388	36.391	36.535	36.599	36.603	36.632
.05-90	53.256	53.367	53.534	53.57	53.631	53.683	54.784	54.861	55.037	55.143
.15-90	52.328	52.417	52.463	52.481	52.572	52.621	53.517	53.657	53.743	53.771
.25-90	50.957	51.004	51.153	51.175	51.268	51.304	51.912	52.015	52.199	52.212
.35-90	49.08	49.126	49.454	49.519	49.563	49.629	49.745	49.86	50.183	50.204
.45-90	46.328	46.348	46.523	46.576	46.671	46.784	46.941	46.993	47.097	47.151

Immediately apparent is the fact that the eigenvalues are all very close in magnitude for each case. This is very important to note, because such cases can indicate some form of sensitivity of the solution with respect to design or imperfection parameters (Koiter, 1945). This effect is explored in Chapter 5.

The simplified results from Chapter 2 indicated that the lowest eigenvalues would correspond to a mode with an infinite number of vertical waves. This was not observed on the eigenmodes obtained from the more accurate finite element analyses. Instead, the number of vertical waves varied from one to three, four waves being the maximum seen for higher eigenvalues, for example the 23rd mode for the 05.-70 case. The general trend

observed was that the eigenvalue increased for increasing number of waves, both vertical and circumferential, though no exact pattern was observed.

Figure 3.9 shows some modal shapes obtained from the eigenvalue extraction analyses, along with analogous mode shapes used in Chapter 2.

(a)   (b)

(c)   (d)

(e)   (f)
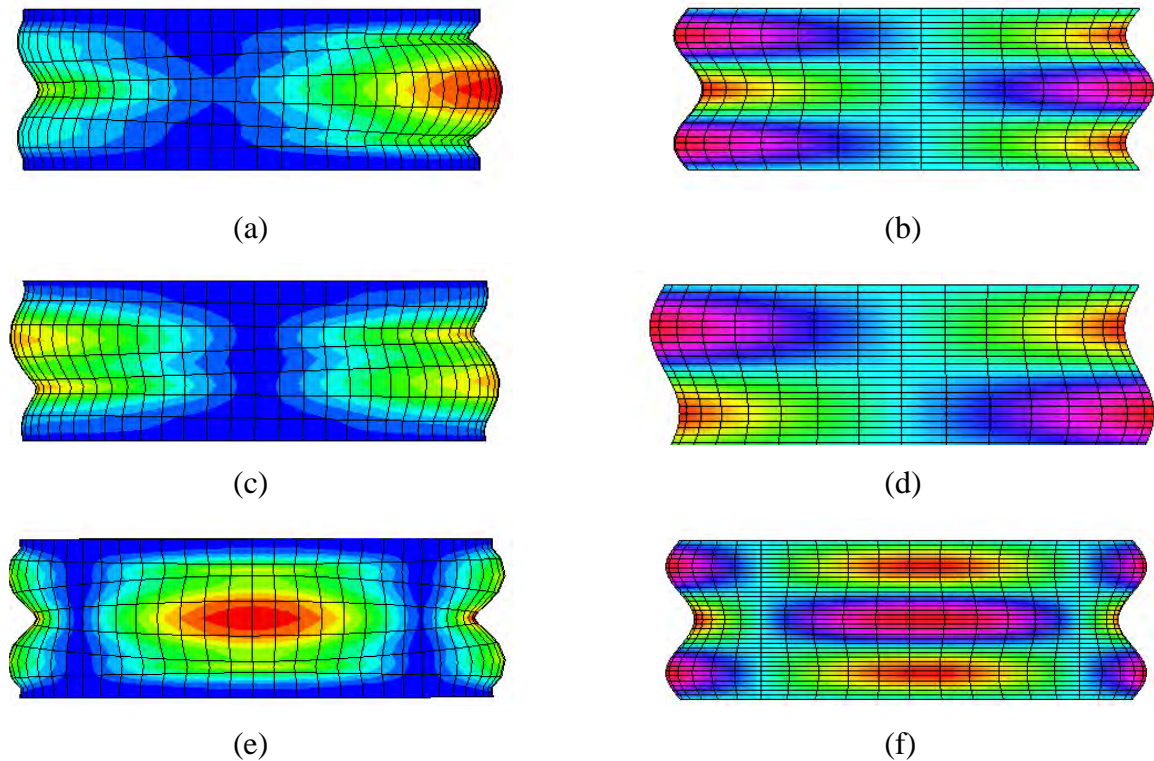
Figure 3.9. Mode shapes from eigenvalue extraction analyses and simplified formulation analogues; (a) Case .25-70, Mode 1; (b) Mode with M=3, N=1; (c) Case .25-70, Mode 6; (d) Mode with M=2, N=2; (e) Case .25-70, Mode 7; (f) Mode with M=3, N=4.

As can be seen from the preceding figures, some modes obtained from the finite element analyses closely matched the simplified displacement formulation modes utilized in the analyses in Chapter 2. However, some modes could not be described by the simple radial displacement function used in Chapter 2. Figure 3.10 shows some of these modes.
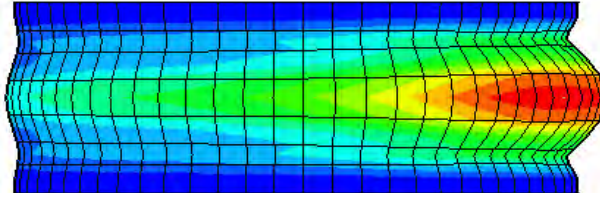
(a)
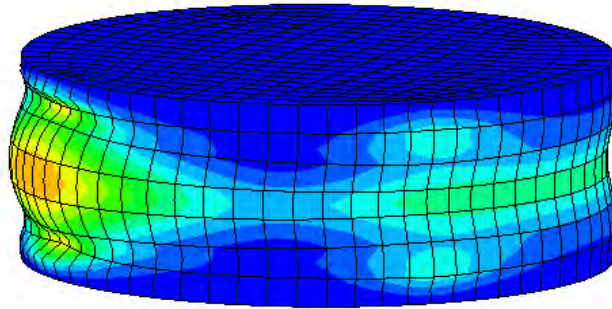
(b)

Figure 3.10. Mode shapes from eigenvalue extraction analyses with no simplified formulation analogue; (a) Case .05-70, Mode 1; (b) Case .45-70, Mode 5.

The mode shape displayed in Figure 3.10 (a) is an "elephant foot" mode, which has no inward displacements in the circumferential direction, thus cannot be approximated by the sinusoid function used for the simplified displacement formulation. Figure 3.10 (b) shows an irregular mode, with localized displacements. These also could not be considered with the displacement function utilized previously.

Another peculiarity of the eigenmodes occurred for the models with nearly incompressible materials (those with highest Poisson's ratios): some modes displayed the largest displacements *inside* of the solid. This internal buckling was not simulated in the buckling analyses of Chapter 2, since the function used was assumed to increase outward linearly from the center. Figure 3.11 shows a mode cross-section with internal maximum displacements.
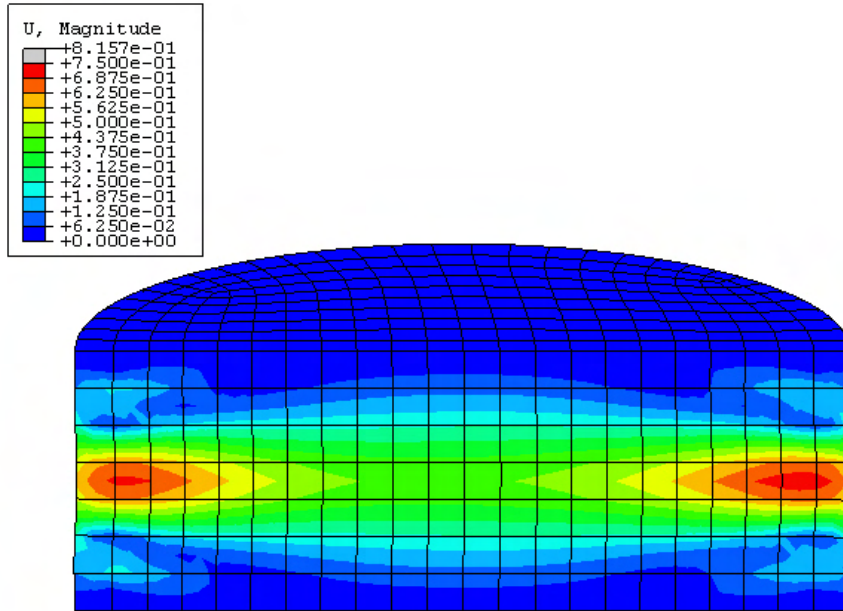
Figure 3.11. Cross-section of mode with internal maximum displacements.

Comparing the results obtained from our formulation and the finite element analyses, similarities and differences arise. The most important difference was in the magnitude of the eigenvalues obtained. In the case of the analytical formulation, the eigenvalues depended heavily on the mode shape assumed. The displacements obtained decreased with larger number of vertical waves and increased with a larger number of circumferential waves, though the effect of the vertical waves was much stronger. With increasing vertical waves, the eigenvalues were seen to decrease asymptotically to values that, in all cases, were lower than the lowest eigenvalue obtained from the corresponding finite element analyses. As previously seen, the eigenvalues obtained from finite elements were all very close to each other numerically. It was noted that there was the general trend of increasing eigenvalue with circumferential waves, similar to what was obtained with our formulation, but there was also a slight trend of increasing eigenvalue

69

with larger number of vertical waves – the exact opposite of the results obtained with the incremental displacement formulation.

3.5 NONLINEAR ANALYSES

3.5.1 Introduction

The stability analyses reported in Chapter 2 and in the previous section have been eigenvalue extraction analyses, which find bifurcation type instabilities. As discussed in Chapter 2, the second type of buckling is a limit point. These points can be found with geometrically nonlinear analyses. In these analyses, the strain and stress tensors account for second order effects on the geometry of the structure.

A nonlinear analysis will always end at some point, since the nonlinearity of the system response will cause the system to become unstable. This can be recognized in graphs of load displacement response, when the response tends to infinity for a given increase in load. Figure 3.12 shows the typical load displacement response of a nonlinear analysis of a solid thick cylinder under compressive displacement, where the radial displacement at a point in the circumference of the solid increases without bound for increasing top displacement. This is indicative of a loss of stiffness, which tends to zero as load is increased.
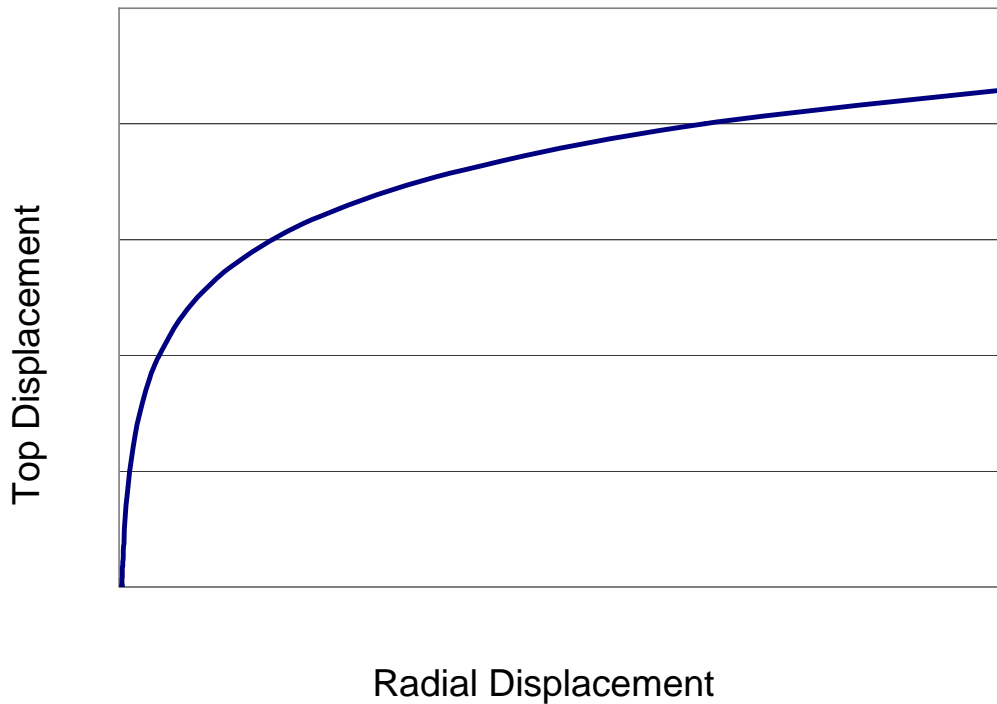
Figure 3.12. Typical load-displacement curve for geometrically nonlinear analyses.

Geometrically nonlinear analyses are incremental, where the system response is obtained by iteration. Since we are searching for points of instability, we use the modified Riks method. In this method, the solution is found a single equilibrium path in a space defined by the nodal variables and the load parameter. Therefore the load parameter itself is an unknown in each increment, and is found as part of the solution for equilibrium along the path. The basic incremental algorithm utilized in ABAQUS is the Newton method, which, as an incremental method, is refined with smaller increments. According to the user manual (Hibbit et al, 2003): "In the modified Riks algorithm, as it is implemented in ABAQUS, the increment size is limited by moving a given distance

71

(determined by the standard, convergence rate-dependent, automatic incrementation algorithm for static case in ABAQUS/Standard) along the tangent line to the current solution point and then searching for equilibrium in the plane that passes through the point thus obtained and that is orthogonal to the same tangent line.". This method has been successful in dealing with unstable problems (Crisfield, 1981; Ramm, 1981). The conditions for use of this method are that loading be proportional (controlled by a single scaling parameter), and that the response not encounter bifurcations. Having already determined the results of bifurcation analysis, we can compare the results from both analyses.

3.5.2 Nonlinear Analysis Results

Figure 3.13. through 3.15 show the top displacement versus circumferential displacement at midheight for all material and geometry cases. Both nonlinear and linear analysis results are presented for comparison. Unlike the linear analyses, the nonlinear analyses show a drop in the slope of these plots. These drops are indicative of the nonlinear geometric effects, which result in loss of stiffness and structure instability. For convenience and easy comparison, the five figures corresponding to the five material cases are all presented in one page per geometry. The three pages list the results for the three geometries in order of increasing solid height (i.e. 50mm, 70mm, and 90mm).

72
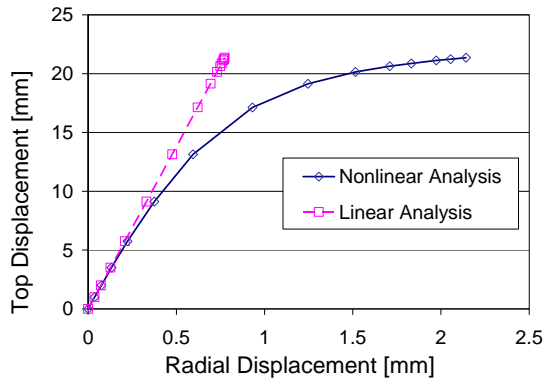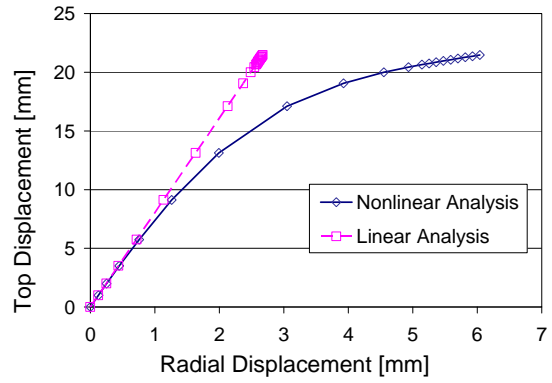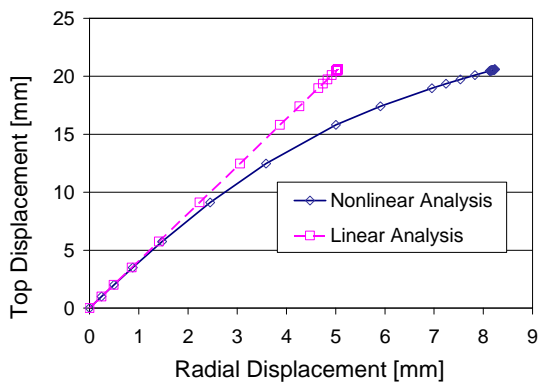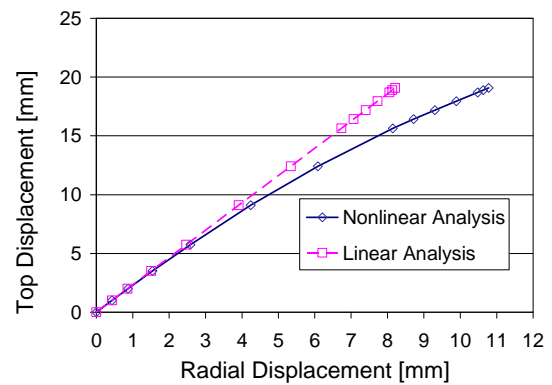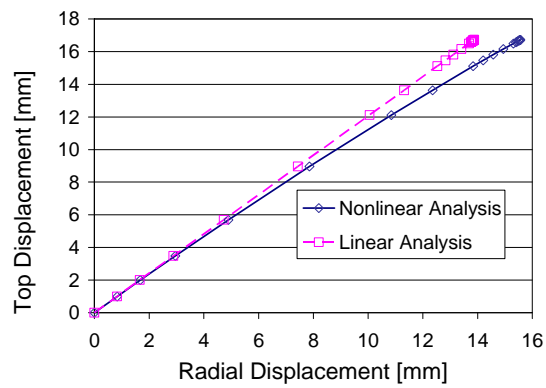
Figure 3.13. Top displacement versus radial displacement plots for cases with
H = 50 mm; (a) Case .05-50; (b) Case .15-50; (c) Case .25-50;
(d) Case .35-50; (e) Case .45-50.
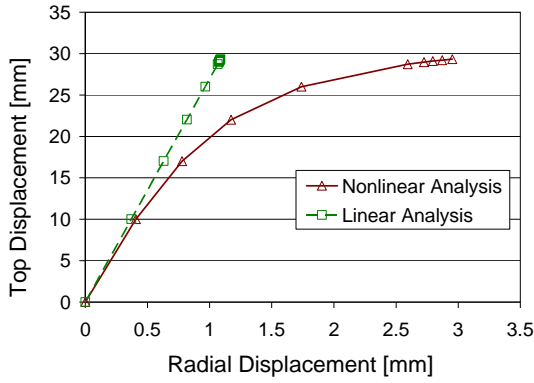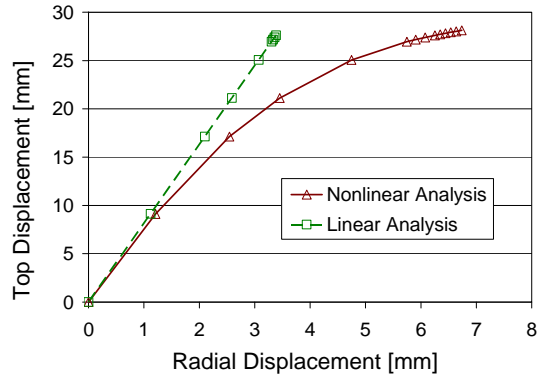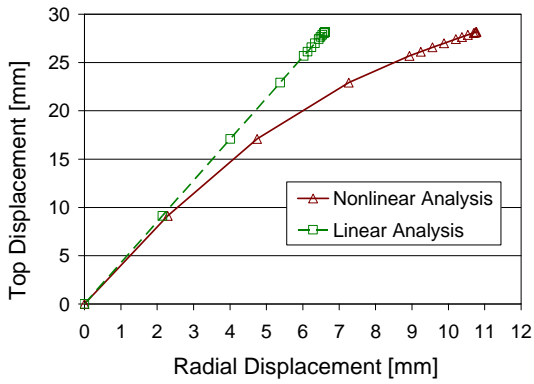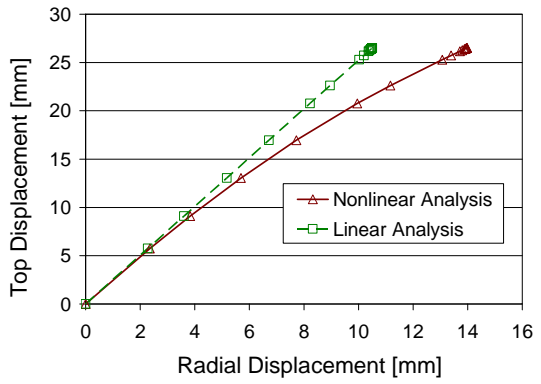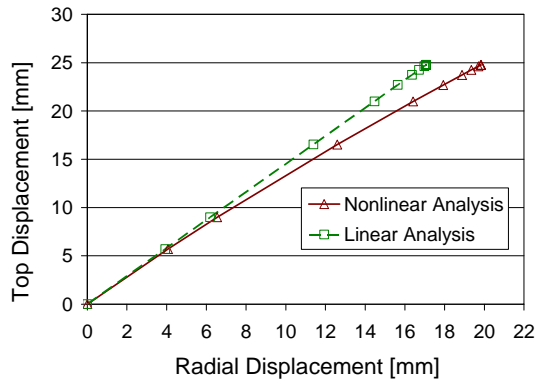
Figure 3.14. Top displacement versus radial displacement plots for cases with
H = 70 mm; (a) Case .05-70; (b) Case .15-70; (c) Case .25-70;
(d) Case .35-70; (e) Case .45-70.
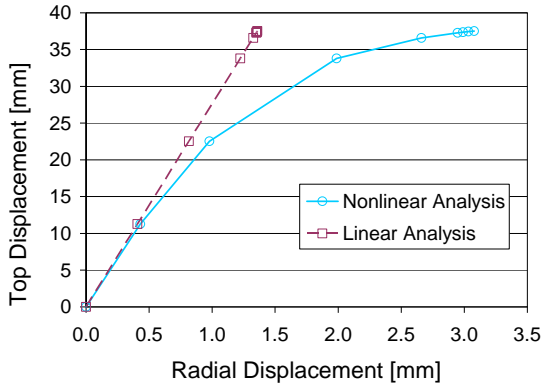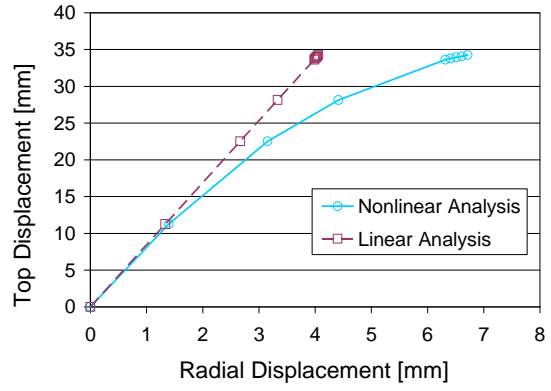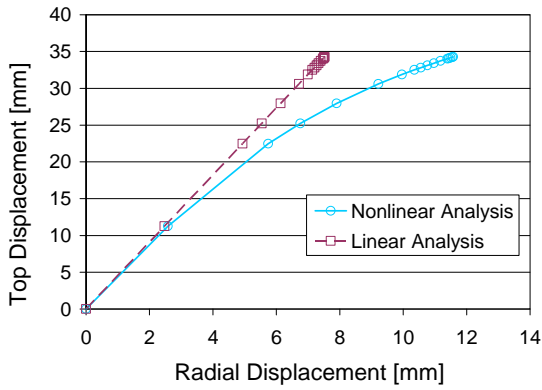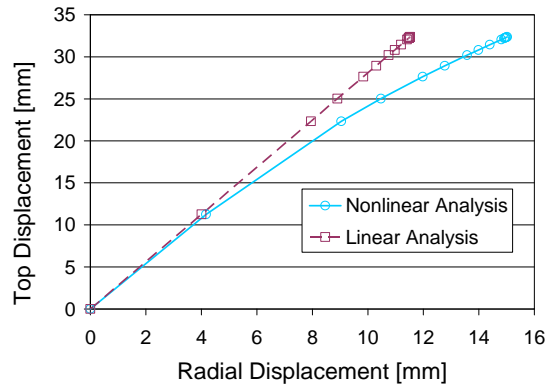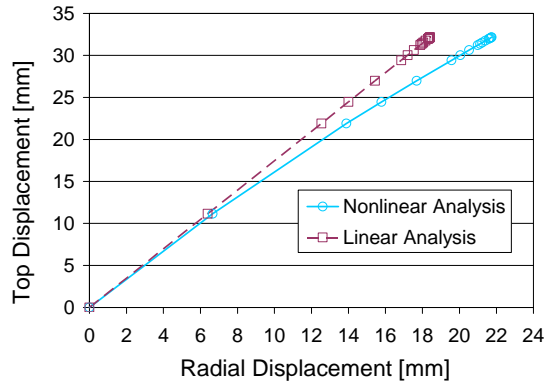
Figure 3.15. Top displacement versus radial displacement plots for cases with
H = 90 mm; (a) Case .05-90; (b) Case .15-90; (c) Case .25-90;
(d) Case .35-90; (e) Case .45-90.

In the preceding figures, more points are seen at the end of the plots. This is because at these points the equilibrium tolerances in the analyses necessitate smaller increments. This indicates the increasing difficulty in obtaining equilibrium that complies with program tolerances. Inspecting the plots closely we can see that for the materials for higher Poisson's ratio (i.e., nearly incompressible materials), the response plots do not even approach the curvature that indicates that a limit point is close. The Riks method employed to follow a nonlinear equilibrium path, as utilized, handles limit points, obtaining even postbuckling paths. Performing straightforward nonlinear analyses (where the load is not an unknown), we found the analyses ending at the same top displacement magnitudes. We had solid ground to suspect a model limitation, which was confirmed by inspecting the deformed mesh at the end of the nonlinear analyses. Figure 3.16 shows a section of the solid for Case .45-70, where the extreme deformation of certain elements is evidenced, compared to the undeformed mesh:

As can be seen in Figure 3.16, the top and bottom edge elements are extremely deformed. This introduces a singularity in the stiffness matrix which makes it impossible to find equilibrium, and the analysis ends. Observing the deformations achieved, it is seen that a refinement of the kinematic model (strain-displacement relations) and the finite element mesh is needed to allow the analysis to continue.
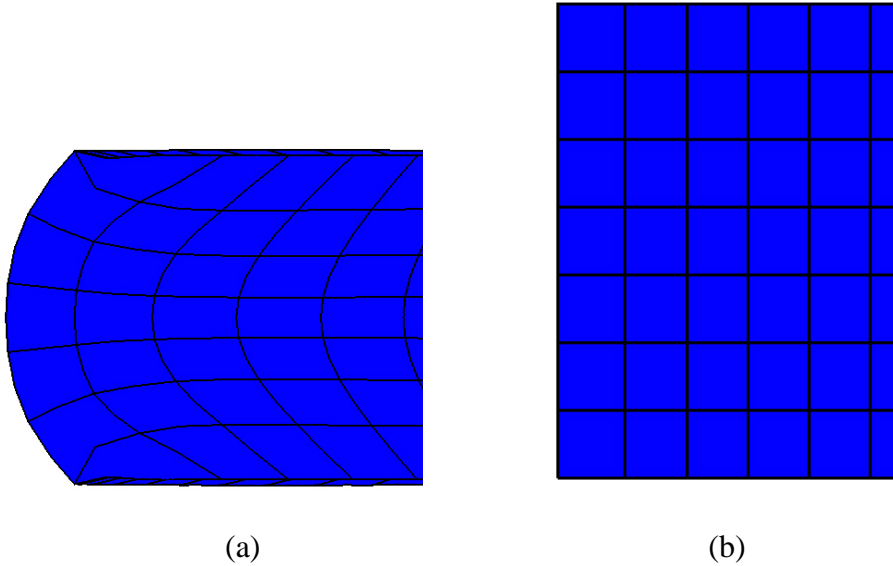
Figure 3.16. Extreme deformation in mesh elements for high Poisson's ratio;
(a) Deformed mesh; (b) Undeformed mesh.

Some of the difficulties found in this class of behavior in incompressible materials are shown in Figure 3.17, where the solid starts to exhibit a bulging behavior which is closer to solid flow than to buckling. Figure 3.17 is an exaggeration of the scale of deformation of Figure 3.16, which demonstrates the deformed state the solid approaches. Such a phenomenon, typical of incompressible materials, is outside the scope of this thesis and is not explored further.
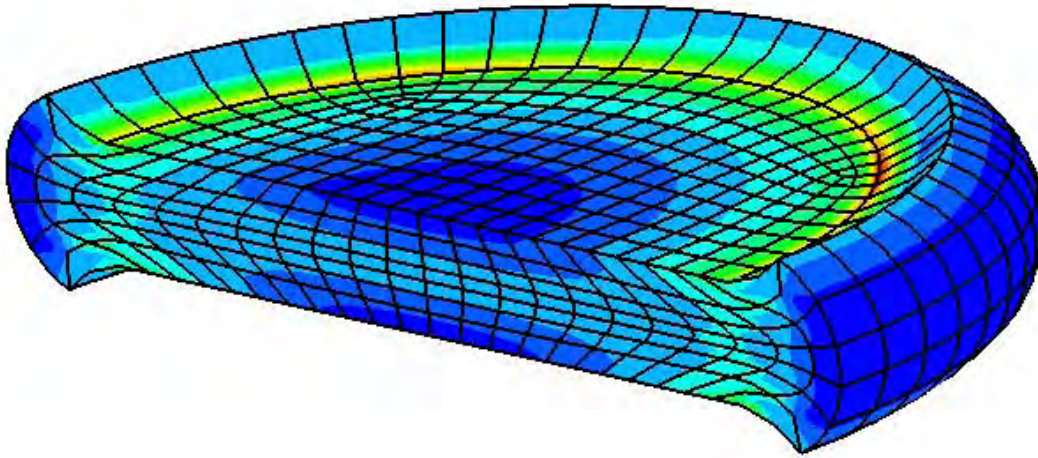
Figure 3.17. Extrapolation of system behavior for large Poisson's ratio.

As can be seen from Figure 3.17, the solid will not only bulge outward, but upwards and downwards as well as it deforms past the initial boundary conditions in the axial direction. This would necessitate the elements to consider large rotations along with large displacements. Also, only large displacement theory is used for the nonlinear analyses in the program. As such, it seems that the problems with large Poisson's ratios cannot be taken to their limit points with the present finite element formulation. We can, however, reasonably expect that the limit points would be found at greater top displacements magnitudes than those reached with the elastic finite element analyses.

3.6 COMPARISON OF RESULTS

Table 3.3 lists the results for the minimum eigenvalues obtained from the finite element buckling analyses, the maximum top displacements from the nonlinear analyses, and the eigenvalues obtained using the incremental displacement formulation with M = 10 and N = 1 (which was closest to the asymptotic value discussed in Chapter 2 in all

cases). The results for higher Poisson's ratio are marked with an asterisk (*), to point out that these are not reasonable approximations to limit points.

Table 3.3. Comparison of results obtained.

Case ID	ABAQUS Buckling Analysis Top Displacement [mm]	ABAQUS Nonlinear Analysis Top Displacement [mm]	Analytical formulation; M=10, N=1 Top Displacement [mm]
Case .05-50	30.59	21.35	23.85
Case .15-50	29.84	21.47	21.78
Case .25-50	28.95	20.59*	20.05
Case .35-50	27.65	19.07*	18.58
Case .45-50	25.08	16.72*	17.39
Case .05-70	42.26	29.46	33.44
Case .15-70	41.3	28.13	30.55
Case .25-70	40.17	28.16*	28.13
Case .35-70	38.69	26.50*	26.09
Case .45-70	36.39	24.76*	24.54
Case .05-90	53.25	37.52	43.09
Case .15-90	52.32	34.24	39.37
Case .25-90	50.95	34.28*	36.27
Case .35-90	49.08	32.36*	33.7
Case .45-90	46.32	32.16*	31.88

From the table we can see that in all cases the eigenvalues obtained from the analytical formulation analyses (performed with a significantly incident mode) were lower than those obtained with finite elements.

Table 3.4 contains a quantification in percent difference between the results for all cases.

Table 3.4. Percent difference between buckling results.

Case ID	ABAQUS Buckling Analysis Top Displacement [mm]	Analytical formulation; M=10, N=1 Top Displacement [mm]	Percent Difference
Case .05-50	30.59	23.85	22%
Case .15-50	29.84	21.78	27%
Case .25-50	28.95	20.05	31%
Case .35-50	27.65	18.58	33%
Case .45-50	25.08	17.39	31%
Case .05-70	42.26	33.44	21%
Case .15-70	41.3	30.55	26%
Case .25-70	40.17	28.13	30%
Case .35-70	38.69	26.09	33%
Case .45-70	36.39	24.54	33%
Case .05-90	53.25	43.09	19%
Case .15-90	52.32	39.37	25%
Case .25-90	50.95	36.27	29%
Case .35-90	49.08	33.7	31%
Case .45-90	46.32	31.88	31%

As Table 3.4 shows, the percent differences vary from 19% to 33%, and are always larger for the material cases with larger Poisson's ratio. However, they are both very large displacements in all cases.

In reference to the nonlinear results, we must discard our results for the larger Poisson's ratio cases (see section 3.5.2). However, we call attention to the fact that all the maximum displacements from the nonlinear analyses for all the material/geometric

combinations are very close in magnitude relative to the solid height. Table 3.5, which shows the nonlinear analysis maximum displacements normalized to the solid height, illustrates this fact. Again, the results for higher Poisson's ratio are marked with an asterisk (*), to point out that these are not reasonable approximations to limit points.

Table 3.5. Normalized nonlinear analysis results.

ABAQUS Nonlinear Analysis		
Case ID	**Top Displacement [mm]**	**Normalized Top Displacement [mm/mm]**
Case .05-50	21.35	42.7%
Case .15-50	21.47	42.9%
Case .25-50	20.59*	41.2%
Case .35-50	19.07*	38.1%
Case .45-50	16.72*	33.4%
Case .05-70	29.46	42.1%
Case .15-70	28.13	40.2%
Case .25-70	28.16*	40.2%
Case .35-70	26.50*	37.9%
Case .45-70	24.76*	35.4%
Case .05-90	37.52	41.7%
Case .15-90	34.24	38.0%
Case .25-90	34.28*	38.1%
Case .35-90	32.36*	36.0%
Case .45-90	32.16*	35.7%

As we can see from the preceding table, the maximum displacements achieved for all cases range from 33% to 43%, the highest percentage belonging to the highly nonlinear response of the lower Poisson's ratio cases. However, even at the maximum displacements obtained, the cases with higher Poisson's ratio exhibit very linear

behavior. This has a very important implication, which is: if limit points are to be found for these cases, then they must lie at *higher* displacement values than the other cases. This inference is drawn based on the linearity of the response up to the points that have been calculated, added to the fact that limit points must be arrived at smoothly – that is, there cannot be a sudden drop in the slope of the top displacement versus radial displacement plots (see Figure 3.13 through 3.15).

Considering only the materials with low Poisson's ratio, we can compare to the eigenvalue buckling analyses as well as the nonlinear analyses.

Table 3.6. Comparison of results for materials with low Poisson's ratio.

Case ID	ABAQUS Buckling Analysis Top Displacement [mm]	ABAQUS Nonlinear Analysis Top Displacement [mm]	Analytical formulation; M=10, N=1 Top Displacement [mm]
Case .05-50	30.59	21.35	23.85
Case .15-50	29.84	21.47	21.78
Case .05-70	42.26	29.46	33.44
Case .15-70	41.3	28.13	30.55
Case .05-90	53.25	37.52	43.09
Case .15-90	52.32	34.24	39.37

There is a clear pattern in all cases: the displacement eigenvalue obtained from finite element buckling analysis is the highest, followed by the eigenvalue calculated with the analytical formulation, and lastly the maximum displacement obtained from the nonlinear analysis. It is noted that of these three, the most similar are the nonlinear analysis and analytical formulation results.

3.7 CONCLUSIONS

Buckling of a solid has been investigated with buckling analyses for bifurcation and nonlinear analyses for limit point. Eigenvalues and mode shapes were obtained from the buckling analyses. These were found to resemble the results from Chapter 2. Again, the displacements required to find a bifurcation were found to be very large: the lowest eigenvalue amounted to close to half the total height for all cases. This, of course, is completely against the small displacement assumption of a linear perturbation analysis such as the eigenvalue analyses carried out. Thus, these eigenvalues may represent higher values than what would be found experimentally, or with a more advanced analysis considering large displacement theory.

The nonlinear analyses, which do consider large displacements effects, found the instability points at lower values than those found by eigenvalue analyses. However, it was found that for nearly incompressible materials (with high Poisson's ratio) the geometrically nonlinear analyses ended due to limitations of the finite element models. It was inferred from the almost linear responses in these cases that the limit point was not approached, and the analyses ended prematurely. Consequently, we discard those results as not representing limit points. For those cases we can say we have obtained values of top displacement under which there are no instabilities, and we infer from the displacement response plots that the limit points must exist at higher top displacement values than those obtained form the analyses for materials with low Poisson's ratio. Being so, it becomes evident that our interest must shift to materials with low Poisson's ratio.

Considering only the nonlinear results for the materials with low Poisson's ratio, we found that there were clear instabilities of the limit point type. It was also seen that for these cases, the maximum displacements from the nonlinear analyses (the limit points) were very close to the lowest displacement eigenvalues found with the analytical formulation. This suggests that the analytical method is worth a closer look. We explore this in the context of the reduced energy method in the next chapter.

CHAPTER 4

REDUCED ENERGY METHOD

4.1 INTRODUCTION

In the previous chapters we have determined that eigenvalue extraction analyses in finite elements predict eigenvalues that are high compared to the ultimate displacements found with a nonlinear analysis. This difference can be attributed to the small displacement/rotation assumption in a linear eigenvalue extraction analysis or the differing type of instability (limit point versus bifurcation). These factors could cause the instabilities of the system to be found at higher levels than when considering a fully geometrically nonlinear analysis. However, the asymptotic eigenvalues for displacement obtained in Chapter 2 very much resembled the maximum displacements achieved in nonlinear analyses for materials with low Poisson's ratio.

The analytical solution presented in Chapter 2 is clearly a simplified version of the problem, in which some terms were retained but some were not included because they would lead to a cumbersome formulation not amenable to analytical solution. As explained in Chapter 3, the analytical results are an upper bound to the more accurate nonlinear finite elements results, in the sense that the critical loads computed analytically

are higher values than those limit points computed with finite elements. The eigenvalue results from finite element buckling analyses are also higher values than the nonlinear limit points, indicating that any eigenvalue model overestimates the actual maximum load that the solid can attain when considering geometric nonlinearity. This however, due to the finite element model limitations discussed in section 3.5.2 of Chapter 3, can only be affirmed to apply to materials with low Poisson's ratio.

The differences in values obtained by bifurcation and limit point analyses are not new in the field of stability theory, and these have been the subject of much research in the context of thin-walled structures. The discrepancies between bifurcation loads computed from a linear fundamental path via eigenvalue analysis and an incremental geometrically nonlinear analysis (leading to a limit-point instability) may be due to various factors, which in thin-walled structures include the presence of geometric imperfections and mode interactions. However, the reasons for this discrepancy in the instability of 3D solids considered in this thesis cannot be considered as known *a priori*. As such, an exploration into the influence of geometric deviations from perfect geometries of 3D solids is reported in this thesis in Chapter 5.

However, the fact that the analytical bifurcation loads are lower than the bifurcations computed numerically seems to indicate that the complete energy of the solid is not a good measure of the energy that is actually involved in the process of instability in more realistic models, such as those including geometric nonlinearity. Thus, it seems reasonable to explore the energy terms that play a role in the instability process and those that, for some reason, are not employed by the solid in resisting external loads at buckling. This is the subject of this chapter.

A procedure which has been developed for shells to obtain results from eigenvalue extraction analyses that agree with ultimate loading values from nonlinear analyses is the reduced energy method, also known as the reduced stiffness method. In this method, a part of the positive (stabilizing) energy is removed from the total potential energy before performing the eigenvalue buckling analysis. This method has been developed in the context of thin shells in the search for lower bounds for buckling loads (Croll, 1975; Batista, 1979). It has been shown to work well for shell systems, and even design procedures have been developed which employ the methodology (Croll and Ellinas, 1983). However, this is because of the particular importance of a membrane energy term which is easily identifiable within shell theory (Croll, 1995), so an analogue in a 3D solid is expected to be a different problem. Even so, this tantalizing avenue is clearly well worth exploring.

In this chapter, the contributions of the integrated potential energy terms used in our analytical formulation are examined for several mode shapes. Positive and negative contributions to the total potential energy are identified and the reduced energy method is applied to solid buckling.

4.2 INTEGRATED POTENTIAL ENERGY TERMS

Delving further into the potential energy, we look into the individual integrated energy terms for each case. The energy of the system is the summation of the integration of the product of stresses and strains. Negative terms are those that destabilize the system. Positive terms stabilize the system. Since the total potential energy is a arithmetical sum, then the most relevant terms are those with the largest magnitudes. Recalling Equation 2.46 in Chapter 2, in our incremental displacement model the energy terms that are

allowed to be nonzero are $\int\sigma'_{33}\varepsilon'_{33}$, $\int\sigma'_{13}\varepsilon'_{13}$, $\int\sigma'_{23}\varepsilon'_{23}$, $\int\sigma^f_{11}\varepsilon''_{11}$, $\int\sigma''_{11}\varepsilon^f_{11}$, $\int\sigma''_{22}\varepsilon^f_{22}$ and $\int\sigma''_{33}\varepsilon^f_{33}$.

Table 4.1 through 4.5 show the integrated energy terms for selected eigenmodes for all material/geometry cases. Note that for $\int\sigma'_{13}\varepsilon'_{13}$ and $\int\sigma'_{23}\varepsilon'_{23}$ the energy tabulated is actually twice that of the terms. Since $\sigma_{ij} = \sigma_{ji}$ and $\varepsilon_{ij} = \varepsilon_{ji}$ they are not considered separately.

Table 4.1. Integrated energy terms for M=1 and N =1.

Case	$\int\sigma'_{33}\varepsilon'_{33}$	$\int\sigma'_{13}\varepsilon'_{13}$	$\int\sigma'_{23}\varepsilon'_{23}$	$\int\sigma^f_{11}\varepsilon''_{11}$	$\int\sigma''_{11}\varepsilon^f_{11}$	$\int\sigma''_{22}\varepsilon^f_{22}$	$\int\sigma''_{33}\varepsilon^f_{33}$
.05-50	213,262	1,329,352	8,418	-775,516	-782,997	2,454	5,027
.15-50	194,537	1,054,121	6,675	-627,667	-672,382	19,506	25,209
.25-50	201,022	881,783	5,584	-544,194	-670,953	59,589	67,170
.35-50	269,897	819,625	5,190	-547,356	-917,414	180,086	189,971
.45-50	1,051,927	1,258,436	7,969	-1,159,166	-4,692,988	1,754,381	1,779,440
.05-70	756,791	2,406,839	29,873	-1,596,752	-1,618,832	5,850	16,231
.15-70	710,729	1,964,878	24,388	-1,349,997	-1,466,052	46,007	70,048
.25-70	770,967	1,725,428	21,416	-1,258,905	-1,591,938	149,329	183,704
.35-70	1,141,016	1,767,877	21,943	-1,465,418	-2,556,245	519,478	571,349
.45-70	5,976,220	3,647,677	45,274	-4,834,586	-20,759,020	7,859,793	8,064,641
.05-90	2,167,587	4,170,220	85,563	-3,211,685	-3,274,003	13,901	48,418
.15-90	2,095,489	3,504,515	71,904	-2,835,954	-3,135,435	107,998	191,483
.25-90	2,381,343	3,223,993	66,148	-2,835,742	-3,705,439	370,848	498,849
.35-90	3,844,766	3,603,639	73,938	-3,761,172	-6,903,420	1,461,085	1,681,163
.45-90	25,133,904	9,280,273	190,408	-17,302,293	-79,951,819	30,718,814	31,930,712

Table 4.2. Integrated energy terms for M=2 and N =2.

Case	$\int\sigma'_{33}\varepsilon'_{33}$	$\int\sigma'_{13}\varepsilon'_{13}$	$\int\sigma'_{23}\varepsilon'_{23}$	$\int\sigma^f_{11}\varepsilon''_{11}$	$\int\sigma''_{11}\varepsilon^f_{11}$	$\int\sigma''_{22}\varepsilon^f_{22}$	$\int\sigma''_{33}\varepsilon^f_{33}$
.05-50	171,545	4,277,266	27,086	-2,237,949	-2,252,789	6,745	8,095
.15-50	151,944	3,293,307	20,855	-1,733,053	-1,838,112	51,098	53,961
.25-50	149,187	2,617,635	16,576	-1,391,699	-1,684,140	144,458	147,983
.35-50	179,312	2,178,143	13,793	-1,185,625	-1,928,808	369,645	373,538
.45-50	457,793	2,190,659	13,873	-1,331,162	-5,153,880	1,908,743	1,913,975
.05-70	511,683	6,509,268	80,792	-3,550,871	-3,578,987	11,959	16,156
.15-70	457,799	5,062,520	62,835	-2,791,577	-2,973,453	86,419	95,457
.25-70	457,517	4,095,704	50,835	-2,302,028	-2,808,150	247,346	258,775
.35-70	571,973	3,544,835	43,998	-2,080,403	-3,428,179	667,193	680,582
.45-70	1,719,814	4,198,859	52,116	-2,985,395	-11,783,895	4,387,750	4,410,750
.05-90	1,209,242	9,305,839	190,933	-5,353,007	-5,404,574	20,554	31,014
.15-90	1,095,107	7,325,866	150,309	-4,285,641	-4,590,749	141,085	164,023
.25-90	1,117,679	6,052,704	124,187	-3,647,285	-4,496,475	409,628	439,562
.35-90	1,462,073	5,481,513	112,467	-3,528,026	-5,912,489	1,173,465	1,210,998
.45-90	5,209,344	7,693,851	157,859	-6,530,527	-26,434,293	9,910,300	9,993,466

Table 4.3. Integrated energy terms for M=1 and N =5.

Case	$\int\sigma'_{33}\varepsilon'_{33}$	$\int\sigma'_{13}\varepsilon'_{13}$	$\int\sigma'_{23}\varepsilon'_{23}$	$\int\sigma^f_{11}\varepsilon''_{11}$	$\int\sigma''_{11}\varepsilon^f_{11}$	$\int\sigma''_{22}\varepsilon^f_{22}$	$\int\sigma''_{33}\varepsilon^f_{33}$
Mode: M=1, N=5							
.05-50	272,439	1,698,230	268,854	-1,119,762	-1,139,568	12,098	7,708
.15-50	247,360	1,340,345	212,196	-899,951	-989,550	49,631	39,968
.25-50	253,574	1,112,302	176,093	-770,985	-997,440	119,575	106,881
.35-50	334,816	1,016,769	160,969	-756,277	-1,366,913	313,389	297,247
.45-50	1,232,651	1,474,640	233,457	-1,470,374	-6,646,469	2,606,831	2,569,264
.05-70	1,134,743	3,608,849	1,119,812	-2,931,702	-3,018,449	54,636	32,111
.15-70	1,052,273	2,909,110	902,686	-2,432,034	-2,776,101	197,626	146,441
.25-70	1,117,860	2,501,777	776,292	-2,197,964	-3,041,313	457,139	386,209
.35-70	1,587,898	2,460,271	763,413	-2,405,791	-4,815,939	1,255,394	1,154,754
.45-70	7,394,861	4,513,566	1,400,542	-6,654,484	-34,725,267	14,202,004	13,868,778
.05-90	3,775,045	7,262,807	3,725,373	-7,381,613	-7,717,163	214,653	120,897
.15-90	3,564,587	5,961,448	3,057,856	-6,291,946	-7,533,705	730,330	511,429
.25-90	3,901,104	5,281,530	2,709,100	-5,945,867	-8,940,560	1,655,939	1,338,754
.35-90	5,872,667	5,504,359	2,823,397	-7,100,211	-16,053,528	4,722,154	4,231,162
.45-90	32,210,470	11,893,176	6,100,468	-25,102,057	-154,354,630	65,665,231	63,587,342

Table 4.4. Integrated energy terms for M=5 and N =1.

Case	$\int\sigma'_{33}\varepsilon'_{33}$	$\int\sigma'_{13}\varepsilon'_{13}$	$\int\sigma'_{23}\varepsilon'_{23}$	$\int\sigma^f_{11}\varepsilon''_{11}$	$\int\sigma''_{11}\varepsilon^f_{11}$	$\int\sigma''_{22}\varepsilon^f_{22}$	$\int\sigma''_{33}\varepsilon^f_{33}$
Mode: M=5, N=1							
.05-50	158,754	24,739,622	6,267	-12,452,322	-12,520,376	33,201	34,854
.15-50	139,275	18,866,861	4,779	-9,505,457	-10,042,651	266,869	270,324
.25-50	134,432	14,742,091	3,734	-7,440,128	-8,937,954	746,840	750,986
.35-50	155,386	11,796,914	2,988	-5,977,644	-9,610,761	1,814,399	1,818,717
.45-50	331,190	9,905,182	2,509	-5,119,440	-19,470,885	7,173,509	7,177,936
.05-70	441,182	35,077,510	17,415	-17,768,053	-17,868,132	47,729	52,350
.15-70	387,750	26,799,285	13,305	-13,600,170	-14,376,784	383,463	393,151
.25-70	375,486	21,008,509	10,430	-10,697,213	-12,864,272	1,077,688	1,089,372
.35-70	438,563	16,987,620	33,736	-8,729,959	-14,070,976	2,666,013	2,675,003
.45-70	966,541	14,748,578	7,322	-7,861,221	-29,975,885	11,050,670	11,063,994
.05-90	953,543	45,863,042	37,640	-23,427,113	-23,564,290	63,553	73,624
.15-90	840,057	35,122,980	28,825	-17,995,931	-19,037,691	510,285	531,475
.25-90	816,958	27,651,068	22,693	-14,245,360	-17,155,226	1,442,073	1,467,793
.35-90	960,791	22,513,354	18,477	-11,746,311	-18,960,407	3,593,302	3,620,795
.45-90	2,223,808	20,527,596	16,847	-11,384,126	-43,558,107	16,071,043	16,102,938

Table 4.5. Integrated energy terms for M=1 and N =10.

Case	$\int \sigma'_{33}\varepsilon'_{33}$	$\int \sigma'_{13}\varepsilon'_{13}$	$\int \sigma'_{23}\varepsilon'_{23}$	$\int \sigma^f_{11}\varepsilon''_{11}$	$\int \sigma''_{11}\varepsilon^f_{11}$	$\int \sigma''_{22}\varepsilon^f_{22}$	$\int \sigma''_{33}\varepsilon^f_{33}$
.05-50	504,014	3,141,736	1,989,528	-2,817,639	-2,938,283	97,707	22,937
.15-50	453,274	2,456,113	1,555,352	-2,232,369	-2,652,186	291,040	128,776
.25-50	457,087	2,005,010	1,269,687	-1,865,892	-2,768,423	555,245	347,285
.35-50	582,735	1,769,649	1,120,643	-1,736,513	-3,851,359	1,182,866	931,980
.45-50	1,889,705	2,260,684	1,431,595	-2,790,992	-16,729,818	7,210,757	6,728,069
.05-70	2,807,547	8,928,909	11,082,424	-11,409,440	-12,308,991	746,487	153,064
.15-70	2,550,144	7,050,116	8,750,495	-9,175,378	-12,064,984	2,098,394	791,211
.25-70	2,616,046	5,854,725	7,266,794	-7,868,782	-13,817,980	3,834,061	2,115,137
.35-70	3,459,284	5,359,774	6,652,469	-7,735,763	-21,708,736	8,081,770	5,891,203
.45-70	12,800,974	7,813,268	9,697,707	-15,155,975	-122,873,874	56,427,674	51,290,226
.05-90	11,654,071	22,421,261	46,002,912	-40,039,122	-45,119,143	4,261,257	818,763
.15-90	10,656,035	17,821,253	36,564,828	-32,521,058	-48,264,267	11,701,051	4,042,157
.25-90	11,055,628	14,967,720	30,710,078	-28,366,713	-60,114,334	20,995,544	10,752,077
.35-90	14,967,850	14,029,131	28,784,326	-28,890,654	-103,741,526	44,187,349	30,663,523
.45-90	59,974,902	22,144,727	45,435,532	-63,777,580	-696,752,029	334,355,824	298,618,625

Inspecting tables 4.1 through 4.5, we see that for all modes the negative (destabilizing terms) are $\int \sigma^f_{11}\varepsilon''_{11}$ and $\int \sigma''_{11}\varepsilon^f_{11}$. The dominant positive terms, however, are different per material and mode. This can be clearly seen if we consider the energy contributions of the positive terms as a percentage of the sum of positive energy. Table 4.6 through 4.10 show the energetic contributions of the positive terms only in terms of percentages of the total positive energy.

Table 4.6. Percentages of total positive energy for M=1 and N =1.

Mode: M=1, N=1					
Case	$\int\sigma'_{33}\varepsilon'_{33}$	$\int\sigma'_{13}\varepsilon'_{13}$	$\int\sigma'_{23}\varepsilon'_{23}$	$\int\sigma''_{22}\varepsilon^f_{22}$	$\int\sigma''_{33}\varepsilon^f_{33}$
.05-50	13.68	85.30	0.54	0.16	0.32
.15-50	14.96	81.08	0.51	1.50	1.94
.25-50	16.54	72.57	0.46	4.90	5.53
.35-50	18.43	55.96	0.35	12.29	12.97
.45-50	17.98	21.50	0.14	29.98	30.41
.05-70	23.54	74.85	0.93	0.18	0.50
.15-70	25.24	69.77	0.87	1.63	2.49
.25-70	27.04	60.52	0.75	5.24	6.44
.35-70	28.37	43.96	0.55	12.92	14.21
.45-70	23.35	14.25	0.18	30.71	31.51
.05-90	33.42	64.30	1.32	0.21	0.75
.15-90	35.09	58.69	1.20	1.81	3.21
.25-90	36.41	49.29	1.01	5.67	7.63
.35-90	36.05	33.79	0.69	13.70	15.76
.45-90	25.84	9.54	0.20	31.59	32.83

Table 4.7. Percentages of total positive energy for M=2 and N =2.

Mode: M=2, N=2					
Case	$\int\sigma'_{33}\varepsilon'_{33}$	$\int\sigma'_{13}\varepsilon'_{13}$	$\int\sigma'_{23}\varepsilon'_{23}$	$\int\sigma''_{22}\varepsilon^f_{22}$	$\int\sigma''_{33}\varepsilon^f_{33}$
.05-50	3.82	95.25	0.60	0.15	0.18
.15-50	4.25	92.22	0.58	1.43	1.51
.25-50	4.85	85.10	0.54	4.70	4.81
.35-50	5.76	69.94	0.44	11.87	11.99
.45-50	7.06	33.78	0.21	29.43	29.51
.05-70	7.18	91.30	1.13	0.17	0.23
.15-70	7.94	87.81	1.09	1.50	1.66
.25-70	8.95	80.15	0.99	4.84	5.06
.35-70	10.38	64.35	0.80	12.11	12.35
.45-70	11.64	28.43	0.35	29.71	29.86
.05-90	11.24	86.50	1.77	0.19	0.29
.15-90	12.34	82.53	1.69	1.59	1.85
.25-90	13.72	74.32	1.52	5.03	5.40
.35-90	15.49	58.06	1.19	12.43	12.83
.45-90	15.80	23.34	0.48	30.06	30.32

Table 4.8. Percentages of total positive energy for M=1 and N =5.

	Mode: M=1, N=5				
Case	$\int\sigma^{'}_{33}\varepsilon^{'}_{33}$	$\int\sigma^{'}_{13}\varepsilon^{'}_{13}$	$\int\sigma^{'}_{23}\varepsilon^{'}_{23}$	$\int\sigma^{''}_{22}\varepsilon^{f}_{22}$	$\int\sigma^{''}_{33}\varepsilon^{f}_{33}$
.05-50	12.06	75.17	11.90	0.54	0.34
.15-50	13.09	70.94	11.23	2.63	2.12
.25-50	14.34	62.90	9.96	6.76	6.04
.35-50	15.77	47.89	7.58	14.76	14.00
.45-50	15.19	18.17	2.88	32.12	31.65
.05-70	19.07	60.65	18.82	0.92	0.54
.15-70	20.20	55.86	17.33	3.79	2.81
.25-70	21.34	47.75	14.82	8.73	7.37
.35-70	21.99	34.07	10.57	17.38	15.99
.45-70	17.87	10.91	3.38	34.32	33.52
.05-90	25.00	48.10	24.67	1.42	0.80
.15-90	25.78	43.12	22.12	5.28	3.70
.25-90	26.21	35.48	18.20	11.12	8.99
.35-90	25.36	23.77	12.19	20.39	18.27
.45-90	17.95	6.63	3.40	36.59	35.43

Table 4.9. Percentages of total positive energy for M=5 and N =1.

	Mode: M=5, N=1				
Case	$\int\sigma^{'}_{33}\varepsilon^{'}_{33}$	$\int\sigma^{'}_{13}\varepsilon^{'}_{13}$	$\int\sigma^{'}_{23}\varepsilon^{'}_{23}$	$\int\sigma^{''}_{22}\varepsilon^{f}_{22}$	$\int\sigma^{''}_{33}\varepsilon^{f}_{33}$
.05-50	0.64	99.07	0.03	0.13	0.14
.15-50	0.71	96.52	0.02	1.37	1.38
.25-50	0.82	90.01	0.02	4.56	4.59
.35-50	1.00	75.68	0.02	11.64	11.67
.45-50	1.35	40.28	0.01	29.17	29.19
.05-70	1.24	98.43	0.05	0.13	0.15
.15-70	1.39	95.79	0.05	1.37	1.41
.25-70	1.59	89.16	0.04	4.57	4.62
.35-70	1.92	74.50	0.15	11.69	11.73
.45-70	2.55	38.98	0.02	29.21	29.24
.05-90	2.03	97.60	0.08	0.14	0.16
.15-90	2.27	94.84	0.08	1.38	1.44
.25-90	2.60	88.06	0.07	4.59	4.67
.35-90	3.13	73.32	0.06	11.70	11.79
.45-90	4.05	37.36	0.03	29.25	29.31

Table 4.10. Percentages of total positive energy for M=1 and N =10.

	Mode: M=1, N=10				
Case	$\int \sigma'_{33}\varepsilon'_{33}$	$\int \sigma'_{13}\varepsilon'_{13}$	$\int \sigma'_{23}\varepsilon'_{23}$	$\int \sigma''_{22}\varepsilon^f_{22}$	$\int \sigma''_{33}\varepsilon^f_{33}$
.05-50	8.76	54.58	34.56	1.70	0.40
.15-50	9.28	50.28	31.84	5.96	2.64
.25-50	9.86	43.26	27.40	11.98	7.49
.35-50	10.43	31.67	20.05	21.17	16.68
.45-50	9.68	11.58	7.33	36.94	34.47
.05-70	11.84	37.65	46.72	3.15	0.65
.15-70	12.01	33.19	41.20	9.88	3.73
.25-70	12.06	27.00	33.51	17.68	9.75
.35-70	11.75	18.20	22.59	27.45	20.01
.45-70	9.27	5.66	7.03	40.88	37.16
.05-90	13.69	26.33	54.02	5.00	0.96
.15-90	13.19	22.06	45.26	14.48	5.00
.25-90	12.49	16.92	34.71	23.73	12.15
.35-90	11.29	10.58	21.70	33.32	23.12
.45-90	7.89	2.91	5.97	43.96	39.26

All modes show a strongly dominant $\sigma'_{13}\varepsilon'_{13}$ term for all material cases, except for the nearly incompressible materials with Poisson's ratio equal to 0.45 in the 70 mm and 90 mm geometries. In those instances, the largest terms are the $\int \sigma''_{22}\varepsilon^f_{22}$ and $\int \sigma''_{33}\varepsilon^f_{33}$ terms. It can be seen there is a pattern: at greater Poisson's ratios, the $\int \sigma'_{13}\varepsilon'_{13}$ term is smaller, while the $\int \sigma''_{22}\varepsilon^f_{22}$ and $\int \sigma''_{33}\varepsilon^f_{33}$ both increase. The same pattern applies to the $\int \sigma'_{23}\varepsilon'_{23}$ term, but this term is significant only when the modes consist of low M relative to N. This fact can be garnered from the tables for the modes with M=1, N=5 and M=1, N=10. The $\int \sigma'_{33}\varepsilon'_{33}$ term accounts for a maximum of 25% of the positive energy (in the case of M=1, N=5), but it is seen that this importance is taken away by the $\int \sigma'_{23}\varepsilon'_{23}$ term in modes with higher N (M=1, N=10). In short, it appears that controlling stabilizing terms are $\int \sigma'_{13}\varepsilon'_{13}$, $\int \sigma''_{22}\varepsilon^f_{22}$ and $\int \sigma''_{33}\varepsilon^f_{33}$.

4.3 PROPOSED REDUCED ENERGY METHOD

The reduced energy method has been used on shell structures in order to find lower bounds for critical loads (Croll, 1975; Sosa, 2005) It is found that the ultimate load capacity can be determined by performing an eigenvalue extraction analysis over the model energy without considering a certain energy term.

As seen previously in Chapter 2, when we utilized the energy retaining all the terms according to our formulation, the eigenvalues obtained depended on the number of waves in the vertical direction (M) and circumferential direction (N). However, these values all decreased to an asymptotical value with increasing M for all geometric/material cases. This is contrary to the usual behavior of buckling in structures with respect to the mode shape, where a certain mode (combination of M and N) is found to hold the lowest eigenvalue, and modes with higher and/or lower M and N all have larger corresponding eigenvalues.

In order to establish a reduced energy analysis, first the relevant energy terms must be identified. The $\int \sigma^f_{11} \varepsilon^{''}_{11}$ and $\int \sigma^f_{11} \varepsilon^{''}_{11}$ terms, since they are both naturally destabilizing (negative) terms, are always included. According to our formulation, this leaves five positive terms, out of which up to four can be retained for a reduced energy analysis. A total of thirty combinations of these remaining positive terms can be assembled.

Because this is a new problem, for which there is no previous experience in the literature, all the possible combinations of positive terms were explored. The numeric trends of the eigenvalues were observed for increasing M (number of vertical waves in the mode) and N (number of circumferential waves). This was done by performing the

buckling analysis while varying either M or N and holding the other one constant for various values. The general behaviors of the eigenvalues with respect to the mode shapes are described in Table 4.11 through 4.14.

Table 4.11. Eigenvalue behavior with respect to mode shape, retaining four terms.

Case	Terms retained	Term eliminated	Eigenvalue behavior with increasing M	Eigenvalue behavior with increasing N
1	$\int \sigma'_{33}\varepsilon'_{33}$, $\int \sigma'_{13}\varepsilon'_{13}$, $\int \sigma'_{23}\varepsilon'_{23}$, $\int \sigma''_{22}\varepsilon^f_{22}$	$\int \sigma''_{33}\varepsilon^f_{33}$	Decreases to asymptote 2	Increases without bound
2	$\int \sigma'_{13}\varepsilon'_{13}$, $\int \sigma'_{23}\varepsilon'_{23}$, $\int \sigma''_{22}\varepsilon^f_{22}$, $\int \sigma''_{33}\varepsilon^f_{33}$	$\int \sigma'_{33}\varepsilon'_{33}$	Decreases to asymptote 1	Increases without bound
3	$\int \sigma'_{23}\varepsilon'_{23}$, $\int \sigma''_{22}\varepsilon^f_{22}$, $\int \sigma''_{33}\varepsilon^f_{33}$, $\int \sigma'_{33}\varepsilon'_{33}$	$\int \sigma'_{13}\varepsilon'_{13}$	Decreases to zero	Increases without bound
4	$\int \sigma''_{22}\varepsilon^f_{22}$, $\int \sigma''_{33}\varepsilon^f_{33}$, $\int \sigma'_{33}\varepsilon'_{33}$, $\int \sigma'_{13}\varepsilon'_{13}$	$\int \sigma'_{23}\varepsilon'_{23}$	Decreases to asymptote 1	No influence
5	$\int \sigma''_{33}\varepsilon^f_{33}$, $\int \sigma'_{33}\varepsilon'_{33}$, $\int \sigma'_{13}\varepsilon'_{13}$, $\int \sigma'_{23}\varepsilon'_{23}$	$\int \sigma''_{22}\varepsilon^f_{22}$	Decreases to asymptote 2	Increases without bound

Table 4.12. Eigenvalue behavior with respect to mode shape, retaining three terms.

Case	Terms retained	Terms eliminated	Eigenvalue behavior with increasing M	Eigenvalue behavior with increasing N
6	$\int \sigma'_{33}\varepsilon'_{33}$, $\int \sigma'_{13}\varepsilon'_{13}$, $\int \sigma'_{23}\varepsilon'_{23}$	$\int \sigma''_{22}\varepsilon^f_{22}$, $\int \sigma''_{33}\varepsilon^f_{33}$	Decreases to asymptote 3	Increases without bound
7	$\int \sigma'_{13}\varepsilon'_{13}$, $\int \sigma'_{23}\varepsilon'_{23}$, $\int \sigma''_{22}\varepsilon^f_{22}$	$\int \sigma''_{33}\varepsilon^f_{33}$, $\int \sigma'_{33}\varepsilon'_{33}$	Decreases to asymptote 2	Increases without bound
8	$\int \sigma'_{23}\varepsilon'_{23}$, $\int \sigma''_{22}\varepsilon^f_{22}$, $\int \sigma''_{33}\varepsilon^f_{33}$	$\int \sigma'_{33}\varepsilon'_{33}$, $\int \sigma'_{13}\varepsilon'_{13}$	Decreases to zero	Increases without bound

Case	Terms retained	Terms eliminated	Eigenvalue behavior with increasing M	Eigenvalue behavior with increasing N
9	$\int \sigma''_{22}\varepsilon^f_{22}$, $\int \sigma''_{33}\varepsilon^f_{33}$, $\int \sigma'_{33}\varepsilon'_{33}$	$\int \sigma'_{13}\varepsilon'_{13}$, $\int \sigma'_{23}\varepsilon'_{23}$	Decreases to zero	No influence
10	$\int \sigma''_{33}\varepsilon^f_{33}$, $\int \sigma'_{33}\varepsilon'_{33}$, $\int \sigma'_{13}\varepsilon'_{13}$	$\int \sigma'_{23}\varepsilon'_{23}$, $\int \sigma''_{22}\varepsilon^f_{22}$	Decreases to asymptote 2	Decreases to zero
11	$\int \sigma'_{33}\varepsilon'_{33}$, $\int \sigma'_{23}\varepsilon'_{23}$, $\int \sigma''_{22}\varepsilon^f_{22}$	$\int \sigma'_{13}\varepsilon'_{13}$, $\int \sigma''_{33}\varepsilon^f_{33}$	Decreases to zero	Increases without bound
12	$\int \sigma'_{13}\varepsilon'_{13}$, $\int \sigma''_{22}\varepsilon^f_{22}$, $\int \sigma''_{33}\varepsilon^f_{33}$	$\int \sigma'_{23}\varepsilon'_{23}$, $\int \sigma'_{33}\varepsilon'_{33}$	Constant asymptote 1 value	Constant asymptote 1 value
13	$\int \sigma'_{23}\varepsilon'_{23}$, $\int \sigma''_{33}\varepsilon^f_{33}$, $\int \sigma'_{33}\varepsilon'_{33}$	$\int \sigma''_{22}\varepsilon^f_{22}$, $\int \sigma'_{13}\varepsilon'_{13}$	Decreases to zero	Increases without bound
14	$\int \sigma''_{22}\varepsilon^f_{22}$, $\int \sigma'_{33}\varepsilon'_{33}$, $\int \sigma'_{13}\varepsilon'_{13}$	$\int \sigma''_{33}\varepsilon^f_{33}$, $\int \sigma'_{23}\varepsilon'_{23}$	Decreases to asymptote 2	Decreases to zero
15	$\int \sigma''_{33}\varepsilon^f_{33}$, $\int \sigma'_{13}\varepsilon'_{13}$, $\int \sigma'_{23}\varepsilon'_{23}$	$\int \sigma'_{33}\varepsilon'_{33}$, $\int \sigma''_{22}\varepsilon^f_{22}$	Decreases to asymptote 2	Increases without bound

Table 4.13. Eigenvalue behavior with respect to mode shape, retaining two terms.

Case	Terms retained	Terms eliminated	Eigenvalue behavior with increasing M	Eigenvalue behavior with increasing N
16	$\int \sigma'_{33}\varepsilon'_{33}$, $\int \sigma'_{13}\varepsilon'_{13}$	$\int \sigma'_{23}\varepsilon'_{23}$, $\int \sigma''_{22}\varepsilon^f_{22}$, $\int \sigma''_{33}\varepsilon^f_{33}$	Decreases to asymptote 3	Decreases to zero
17	$\int \sigma'_{13}\varepsilon'_{13}$, $\int \sigma'_{23}\varepsilon'_{23}$	$\int \sigma''_{22}\varepsilon^f_{22}$, $\int \sigma''_{33}\varepsilon^f_{33}$, $\int \sigma'_{33}\varepsilon'_{33}$	Increases to asymptote 3	Increases without bound
18	$\int \sigma'_{23}\varepsilon'_{23}$, $\int \sigma''_{22}\varepsilon^f_{22}$	$\int \sigma''_{33}\varepsilon^f_{33}$, $\int \sigma'_{33}\varepsilon'_{33}$, $\int \sigma'_{13}\varepsilon'_{13}$	Decreases to zero	Increases without bound
19	$\int \sigma''_{22}\varepsilon^f_{22}$, $\int \sigma''_{33}\varepsilon^f_{33}$	$\int \sigma'_{33}\varepsilon'_{33}$, $\int \sigma'_{13}\varepsilon'_{13}$, $\int \sigma'_{23}\varepsilon'_{23}$	Always zero	Always zero
20	$\int \sigma''_{33}\varepsilon^f_{33}$, $\int \sigma'_{33}\varepsilon'_{33}$	$\int \sigma'_{13}\varepsilon'_{13}$, $\int \sigma'_{23}\varepsilon'_{23}$, $\int \sigma''_{22}\varepsilon^f_{22}$	Decreases to zero	Decreases to zero

21	$\int\sigma'_{33}\varepsilon'_{33}$, $\int\sigma'_{23}\varepsilon'_{23}$	$\int\sigma''_{22}\varepsilon^f_{22}$, $\int\sigma'_{13}\varepsilon'_{13}$, $\int\sigma''_{33}\varepsilon^f_{33}$	Decreases to zero	Increases without bound
22	$\int\sigma'_{13}\varepsilon'_{13}$, $\int\sigma''_{22}\varepsilon^f_{22}$	$\int\sigma''_{33}\varepsilon^f_{33}$, $\int\sigma'_{23}\varepsilon'_{23}$, $\int\sigma'_{33}\varepsilon'_{33}$	Increases to asymptote 2	Decreases to zero
23	$\int\sigma'_{23}\varepsilon'_{23}$, $\int\sigma''_{33}\varepsilon^f_{33}$	$\int\sigma'_{33}\varepsilon'_{33}$, $\int\sigma''_{22}\varepsilon^f_{22}$, $\int\sigma'_{13}\varepsilon'_{13}$	Decreases to zero	Increases without bound
24	$\int\sigma''_{22}\varepsilon^f_{22}$, $\int\sigma'_{33}\varepsilon'_{33}$	$\int\sigma'_{13}\varepsilon'_{13}$, $\int\sigma''_{33}\varepsilon^f_{33}$, $\int\sigma'_{23}\varepsilon'_{23}$	Decreases to zero	Decreases to zero
25	$\int\sigma''_{33}\varepsilon^f_{33}$, $\int\sigma'_{13}\varepsilon'_{13}$	$\int\sigma'_{23}\varepsilon'_{23}$, $\int\sigma'_{33}\varepsilon'_{33}$, $\int\sigma''_{22}\varepsilon^f_{22}$	Increases to asymptote 2	Decreases to zero

Table 4.14. Eigenvalue behavior with respect to mode shape, retaining one term.

Case	Terms retained	Term eliminated	Eigenvalue behavior with increasing M	Eigenvalue behavior with increasing N
26	$\int\sigma'_{33}\varepsilon'_{33}$	$\int\sigma'_{13}\varepsilon'_{13}$, $\int\sigma'_{23}\varepsilon'_{23}$, $\int\sigma''_{22}\varepsilon^f_{22}$, $\int\sigma''_{33}\varepsilon^f_{33}$	Decreases to zero	Decreases to zero
27	$\int\sigma'_{13}\varepsilon'_{13}$	$\int\sigma'_{23}\varepsilon'_{23}$, $\int\sigma''_{22}\varepsilon^f_{22}$, $\int\sigma''_{33}\varepsilon^f_{33}$, $\int\sigma'_{33}\varepsilon'_{33}$	Increases to asymptote 3	Decreases to zero
28	$\int\sigma'_{23}\varepsilon'_{23}$	$\int\sigma''_{22}\varepsilon^f_{22}$, $\int\sigma''_{33}\varepsilon^f_{33}$, $\int\sigma'_{33}\varepsilon'_{33}$, $\int\sigma'_{13}\varepsilon'_{13}$	Decreases to zero	Increases without bound
29	$\int\sigma''_{22}\varepsilon^f_{22}$	$\int\sigma''_{33}\varepsilon^f_{33}$, $\int\sigma'_{33}\varepsilon'_{33}$, $\int\sigma'_{13}\varepsilon'_{13}$, $\int\sigma'_{23}\varepsilon'_{23}$	Always zero	Always zero
30	$\int\sigma''_{33}\varepsilon^f_{33}$	$\int\sigma'_{33}\varepsilon'_{33}$, $\int\sigma'_{13}\varepsilon'_{13}$, $\int\sigma'_{23}\varepsilon'_{23}$, $\int\sigma''_{22}\varepsilon^f_{22}$	Always zero	Always zero

There are five ways the eigenvalues change with increasing M: decreasing to an asymptote, increasing to an asymptote, decreasing to zero, and remaining the same. With respect to increasing N, they either increase without bound, decrease to zero, or remain constant. The same behavior applies to all geometry and material cases.

Three asymptotes are found to occur when utilizing the reduced energy methodology. These are the ones referred to as asymptotes 1, 2 and 3 in Table 4.11 through 4.14. They are numbered in order of decreasing magnitude. Asymptote 1 is the value that is approached with a straightforward buckling analysis. These asymptotes are distinctly different, but the values become very close for lower Poisson's ratio. This is illustrated in a comparison between the .05-90 and .45-90 cases in Table 4.15.

Table 4.15. Comparison between asymptote values.

Case ID	Asymptote 1 [mm]	Asymptote 2 [mm]	Asymptote 3 [mm]
.05-90	42.86	42.85	42.74
.45-90	31.03	18.27	12.95

As the table shows, the three asymptotes obtained by using certain combinations of terms are very different for the case with higher Poisson's ratio – the lower values are so low that it seems unlikely that instability will be found at such displacement levels. Technically, there is a fourth asymptote: the zero value found on some analyses. However, this instance is judged to be trivial, since a zero-displacement instability is not a reasonable result.

The most encouraging results we find, therefore, are those of the reduced energy method when retaining only these three terms: $\int \sigma'_{13} \varepsilon'_{13}$, $\int \sigma''_{22} \varepsilon^f_{22}$ and $\int \sigma''_{33} \varepsilon^f_{33}$. In all cases,

using these terms results in a displacement eigenvalue equal to the asymptotic value approached by the standard buckling analysis as performed with our formulation in Chapter 2. The value is also independent of the mode shape imposed in the incremental displacement field.

It was seen in Chapter 3 that the asymptotic values from our incremental displacement formulation closely resembled the results from the nonlinear analyses performed with finite elements. Having obtained these asymptotic values with the reduced energy method, we now compare the results with the nonlinear analyses.

4.4 COMPARISON OF RESULTS

It was determined that if the eigenvalue extraction analysis was carried out on a reduced energy that contained only the $\int \sigma'_{13} \varepsilon'_{13}$, $\sigma''_{22} \varepsilon^f_{22}$ and $\int \sigma''_{33} \varepsilon^f_{33}$ terms along with the negative terms $\int \sigma''_{11} \varepsilon^f_{11}$ and $\int \sigma^f_{11} \varepsilon''_{11}$, the eigenvalue will always be that asymptotic value approached with increasing M in a regular buckling analysis (see Chapter 2, section 2.6.2), no matter what mode (combination of M and N) is used. Figure 4.1 shows the reduced energy eigenvalues, for all geometric/material cases.
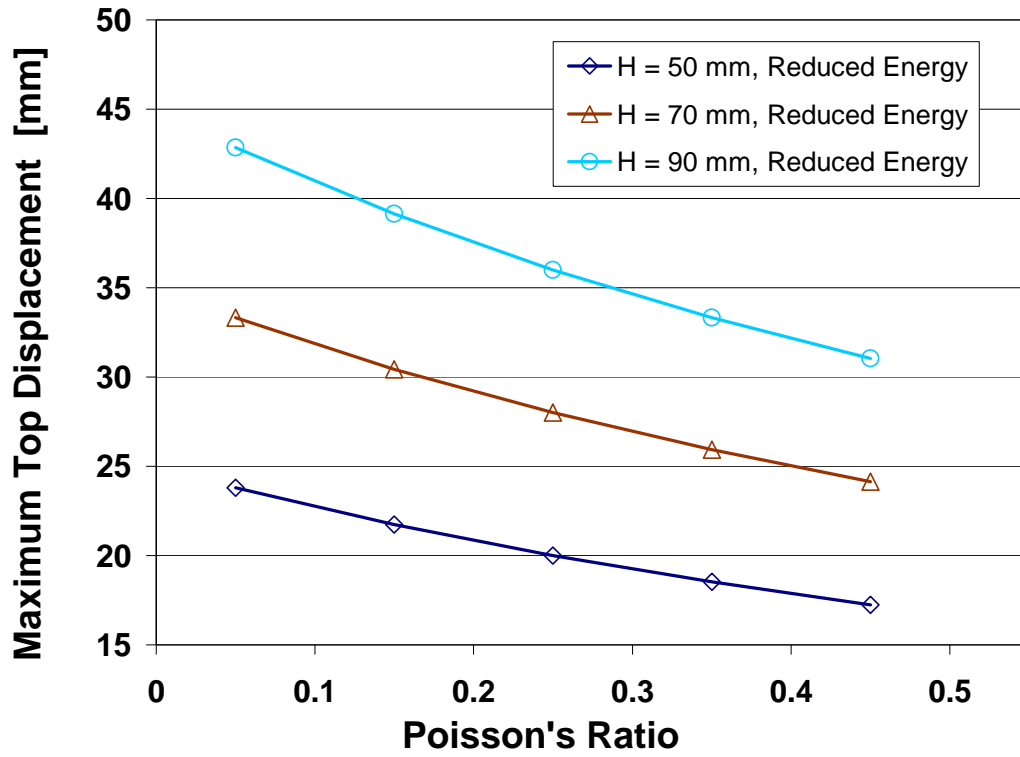
(a)
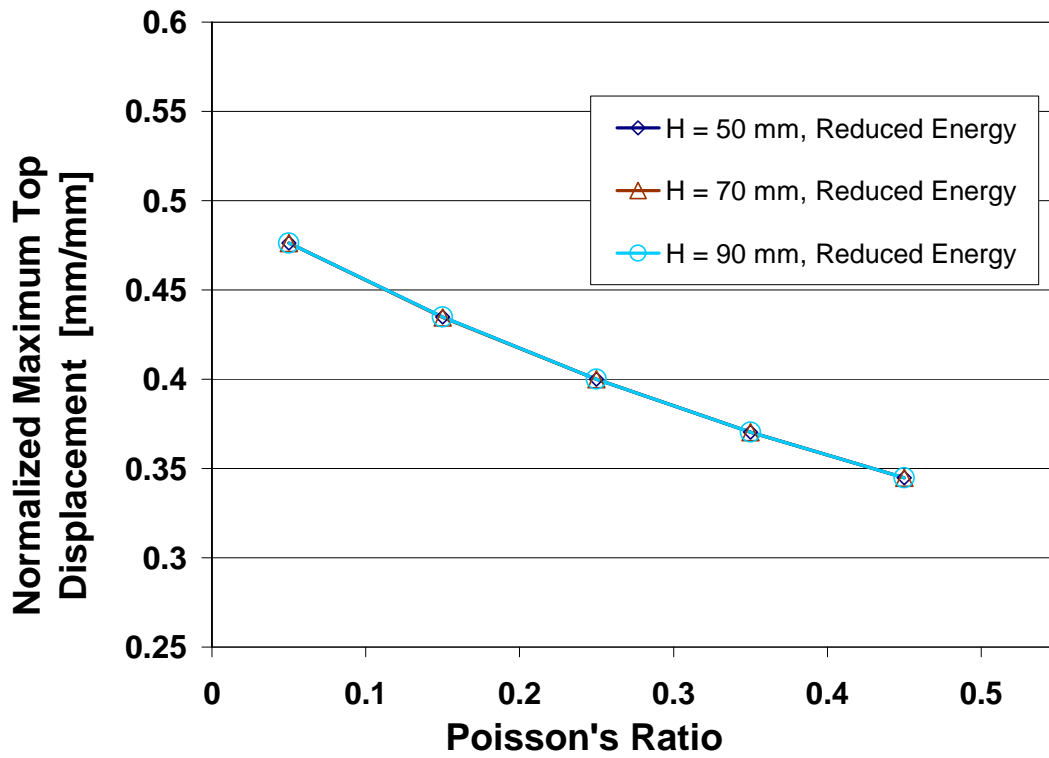
(b)

Figure 4.1. Maximum top displacement versus Poisson's ratio for reduced energy
(a) actual results (b) displacements normalized to solid height.

As seen from the figures, there is a clear decreasing trend with increasing Poisson's ratio. It is also notable that the normalized plots follow a single curve, indicating that the buckling eigenvalues are scaled to the solid height.

Having determined the combination of terms that renders that asymptotic value with the reduced energy, we can now compare the reduced energy methodology with the results for nonlinear analyses obtained in Chapter 3. We compare only the materials with low Poisson's ratio, given the limitations discussed in Chapter 3, section 3.5.2. Table 4.16 lists the maximum displacements obtained for the reduced energy eigenvalue, as well as the nonlinear analyses, for all geometric cases with Poison's equal to 0.05 and 0.15.

Table 4.16. Reduced energy and nonlinear analysis result comparison.

Case ID	ABAQUS Nonlinear Analysis Top Displacement [mm]	Reduced Energy Method Top Displacement [mm]	Percent Difference
Case .05-50	21.35	23.85	10.5%
Case .15-50	21.47	21.78	1.4%
Case .05-70	29.46	33.44	11.9%
Case .15-70	28.13	30.55	7.9%
Case .05-90	37.52	43.09	12.9%
Case .15-90	34.24	39.37	13.0%

As can be seen from Table 4.16, the reduced energy eigenvalues obtained do not constitute a lower bound to the finite element nonlinear results, as for all cases they overestimate the limit points obtained from the nonlinear analyses. It seems this behavior

is more pronounced as the solid becomes taller. However, there is a good overall agreement between the results obtained from both methodologies, with percent differences in the 10-15% range.

4.5 CONCLUSIONS

In this chapter we have investigated the total potential energy following our analytical formulation developed in Chapter 2. Inspecting the energetic contributions of each term, we have found that the naturally destabilizing (negative) terms are $\int\sigma^f_{11}\varepsilon^{''}_{11}$, and $\int\sigma^{''}_{11}\varepsilon^f_{11}$, which is expected since these are the stress-strain terms in the load direction. But the remaining terms are always positive, which implies that they are all stabilizing terms.

Of the stabilizing terms, it was found that three in particular dominated the positive energy, but the magnitudes depended heavily on the mode shape and Poisson's ratio of the material. The $\int\sigma^{'}_{13}\varepsilon^{'}_{13}$ term strongly dominated the energy of most mode shapes for materials for low to intermediate Poisson's ratio (0.05-0.25) – approaching 100% as the number of vertical waves (M) increased past the number of circumferential waves (N). For these materials, as N overtakes M the $\int\sigma^{'}_{23}\varepsilon^{'}_{23}$ term can be seen to take precedence. For materials with high Poisson's ratio (0.35-0.45), depending on the mode shape, the $\int\sigma^{''}_{22}\varepsilon^f_{22}$ and $\int\sigma^{''}_{33}\varepsilon^f_{33}$ terms gain importance (close to 30% of the positive energy each, simultaneously). Even so, the relationships are not direct, and the effects of varying number of waves in both directions are related to a combination of the proportion of M to N, as well as the magnitudes of M and N and the differences between M and N. It is not worth it to attempt to quantify these effects, but our exploration indicates the clear importance of the transverse energy (the $\int\sigma^{'}_{13}\varepsilon^{'}_{13}$ term) in stability. Water can be taken as

an extreme example: if properly bounded, it can resist compression, but it has no shear resistance – therefore it collapses under self weight.

Comparing results, we have found good agreement between finite element nonlinear analyses and the reduced energy methodology. However, the reduced energy method as applied overestimates the maximum displacement compared to nonlinear analysis. This difference was seen to increase with the height of the solid.

The nonlinear analyses from Chapter 3 showed that the instability of a solid, at least for compressible materials, occurs in the form of a limit point. An eigenvalue extraction analysis, on the other hand, assumes the critical state to be a bifurcation, leading to higher results than those obtained by nonlinear analyses. The magnitude of error is highly dependent on the actual nonlinearity of the response of the system. Recalling from Chapter 3, the nonlinear analyses showed that the materials with lower Poisson's ratio had a highly nonlinear response. Even so, the results are still quite similar for the highly compressible materials, even though there is a clear overestimation trend for the materials compared. As such, it seems that contrary to the initial intent of the reduced energy method, we have found an *upper* bound to limit points.

There are three distinct possible reasons for this: first, it is possible that part of the energy contributed by one, some, or all the terms that we have retained in the reduced energy analysis is also lost during the instability process, thereby lowering the displacement capacity. The second possibility is that the terms not considered in our analytical model due to the initial assumptions play a significant role in the instability process. The distribution of the energy contributions, both negative and positive, could be different enough from the models we have used to cause the discrepancy. It is judged

unlikely, however, that the important terms be those related to the circumferential direction, since none of the finite element analyses (linear, buckling, nonlinear) showed any circumferential displacements. Third, there is the previously mentioned relationship between linearity and approximating a limit point as a bifurcation, which is known to overestimate when using a linearized fundamental path. However, even with the noted differences the reduced energy method works well as a first approximation with a simple model.

IMPERFECTION SENSITIVITY IN LINEAR-ELASTIC SOLIDS

5.1 INTRODUCTION

In the last chapter we have used the reduced energy methodology to approximate the limit point behavior of solid instability. This methodology was originally developed by Croll and coworkers (Croll 1975, Croll 1995) to model structural components that were very sensitive to their shape, such as thin-wall structures and shells. Imperfection sensitivity refers to the effect that geometric deviations from the as-designed (perfect) shape of the system can have on its capacity to bear load before reaching a buckled state. The reason why some classes of structures have imperfection sensitivity and others do not exhibit this feature are rather complex, but it is now clear that this depends on both the geometry and the loads. What we know as imperfection sensitivity refers to a process in which several competing (isolated) buckling modes couple due to the presence of imperfections, and the coupled mode leads to lower values of buckling loads along a nonlinear equilibrium path. Thus, what initially may seem as a bifurcation behavior in an isolated mode from a linear fundamental path, becomes a limit point behavior in a

coupled mode from a nonlinear fundamental path. Mode coupling is the key element, and imperfections are the vehicle that makes coupling possible. Finally, modes couple if they are close to each other, i.e. if their eigenvalues show differences of only 2-5%, depending on the problem. Not all components of a geometric imperfection have the effect of triggering buckling, and extensive studies have been performed in the past on the shape of imperfections that are associated with sensitivity of buckling loads. The studies conclude that the worst geometries of imperfections are those given by the eigenmodes in the perfect system. Thus, an eigenmode indicates displacements in a direction of weakness of a structure, and if initial displacements are already present due to imperfections, then the structure has already given a first step towards buckling.

In Chapter 3 we observed that the predicted eigenvalues using finite elements were very close to each other. As mentioned above, the general theory of elastic stability shows that when a system exhibits similar eigenvalues it may be indicative of imperfection sensitivity. Studies of thin-shell structures have found this effect to have an enormous importance in those systems (Thompson and Hunt, 1973). In this chapter, we show that imperfection sensitivity is also predicted for solids. To illustrate this effect, we follow the standard procedure of imposing a modal shape as imperfections on the initial geometry and performing a nonlinear analysis (Croll, 1995). A comparison with the control analysis with no imperfection reveals if there indeed is imperfection sensitivity.

5.2 IMPERFECTION SENSITIVITY IN SOLIDS

5.2.1 Methodology

In order to detect imperfection sensitivity, a common procedure is performed in this chapter. The displacements from a mode shape (or a combination of mode shapes) obtained from an eigenvalue buckling analysis on the same geometry and loads are imposed as imperfections on the initial, "perfect" geometry of the structure. A nonlinear analysis is then performed on this deformed initial geometry. A comparison of the load-displacement responses for analyses with and without imperfections establishes whether or not the structure is imperfection sensitive.

For our present work, we studied the cylindrical geometry with specific dimensions (radius R = 100 mm and height H = 70 mm) and followed the methodology outlined previously. The results from nonlinear analyses performed on models with no imperfections (from Chapter 3) were set as reference (control) cases. Nonlinear analyses were performed on models where mode shapes obtained from the finite element buckling analyses were imposed as three-dimensional imperfections. The imperfection sensitivity was established by comparing the maximum top displacement achieved by the system in each analysis with that of the nonlinear analysis with no imperfections.

Imperfection sensitivity is evaluated in terms of the magnitude of the imperfection applied. For an imperfection sensitive structure, the larger the imperfection, the lesser the ultimate load capacity will be. The sensitivity to imperfection magnitude is determined by imposing the same imperfection mode, but with the initial displacements now multiplied by a factor called the imperfection *amplitude*. The amplitude is a multiplier that is used to either increase or decrease the imperfections initially applied to the

geometry. In our study, the unit imperfection amplitude is taken as the one that imposes a maximum radial displacement in the circumference of the cylinder equal to 1/100 of the cylinder radius (i.e., 1 mm). In other words, an imperfection amplitude of 1 indicates that the cylinder geometry will, at some point(s) in the circumference, have a radius at most 1 mm longer or shorter than the perfect geometry. An imperfection amplitude of 5, for example, will mean that the maximum radius on a point on the circumference of the cylinder will be equal to 105 mm (or the minimum 95 mm, depending on whether the mode applied imposes an outward or inward displacement at the point in question).

5.2.2 Results of Nonlinear Analyses with Imperfections

Figure 5.1 shows the effect of applying the mode shapes from the buckling analyses as imperfections for both material cases studied. The modes are numbered in order of increasing their associated eigenvalues, and are generally different for each material case, i.e. the mode shape of mode 3 for the .05-70 case is not the same as the mode shape of mode 3 for the .15-70 case. In all cases the maximum displacement of the mode shape imposed is equal to 5% of the radius (or 5 mm), that is, the mode shape is normalized to 5. The horizontal lines in the plots represent the maximum displacement obtained in the nonlinear analyses with no imperfections applied.
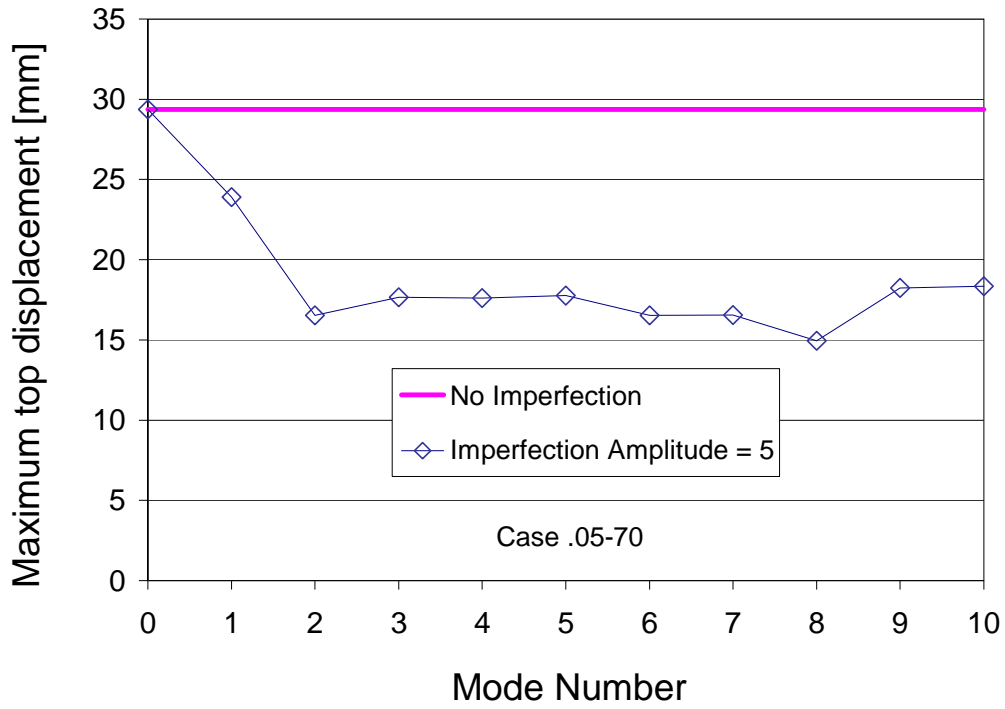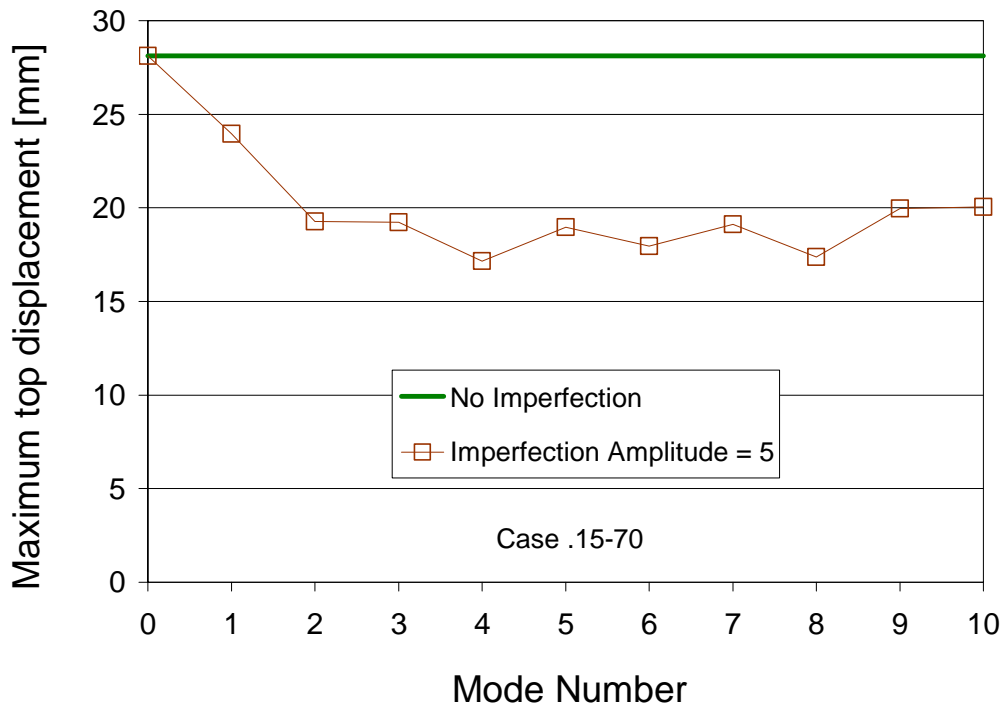
Figure 5.1. Effects of several mode shapes applied as imperfections
(a) Case .05-70; (b) Case .15-70.

As can be seen from the preceding figures, there is a clear indication of a reduction in the buckling loads due to the presence of imperfections for these compressible materials. Recalling that the imperfections were normalized to 5 mm, and that this represents only 5% of the cylinder radius, the adverse effect is clear. Comparing the points in the plots, we can see that the sensitivity effect is dependent upon the mode shape. For example, a lower displacement capacity is found for imperfections with mode 2 than for imperfections with mode 1 for both cases. However, we can surmise that, since all the modes have some effect, *any* imperfection will have *some* effect.

Continuing our investigations, we now select two mode shapes from a buckling analysis and impose them on all the material cases for direct comparison. We have selected mode 6 from the buckling analysis of the .05-70 case and mode 8 of the .15-70 cases because, as it will be seen, these modes produce clear adverse effects. We henceforth refer to these modes as modes 6-05 (mode 6 from the .05-70 buckling analysis) and 8-15 (mode 8 from the .15-70 buckling analysis), to differentiate from the modes corresponding to the same numbers in the buckling analyses of each material case. Figure 5.2 illustrates these mode shapes.
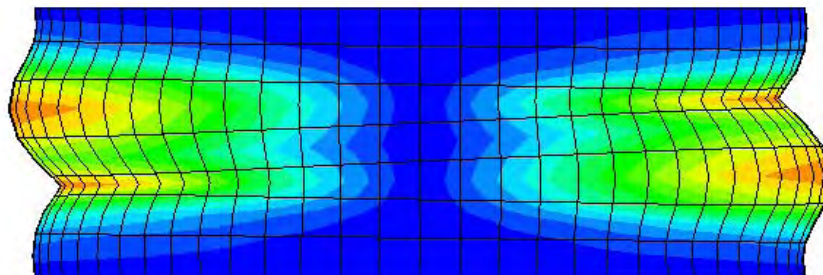
(a)
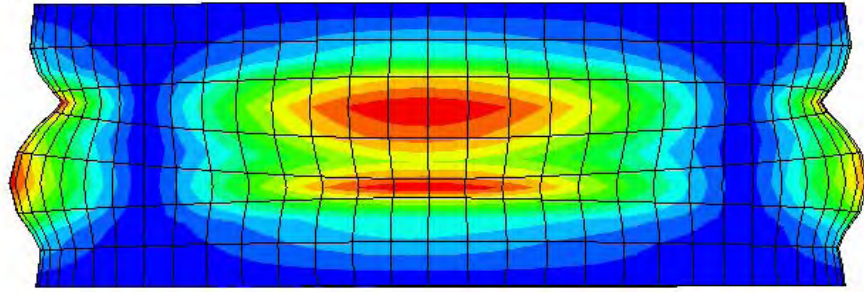
(b)

Figure 5.2. Mode shapes used as imperfections; (a) Mode 6-05; (b) Mode 8-15.

Performing the nonlinear analyses, we can observe the changes in ultimate displacement. Again applying the imperfection modes to each case normalized to 5% of the radius, we can see the effect these modes have as imperfections.

Table 5.1 lists the maximum displacements achieved under the two cases studied, along with the average for the analyses presented previously in Figure 5.1.

Table 5.1. Maximum top displacement for imperfection cases with amplitude=5.

| Case ID | Maximum Top Displacement [mm] | | | |
	Mode used	Value obtained	Average, modes 1-10 for each case:	No Imperfection
.05-70	Mode 6-05	16.52	17.81	29.46
.15-70	Mode 8-15	17.37	19.31	28.13

We can observe the instabilities developing in plots of the radial displacement response to the top displacement. However, a caveat is that a *relevant* point must be chosen for this purpose. As noticed by many authors (Brush and Almroth, 1975), a nonlinear analysis

may exhibit differing responses depending on the point observed. Obvious bad choices would be points in or near the fixed boundaries of the structure, or in the surface the displacement is being applied to. An imperfection mode affects each location in the solid differently, so points which may seem to be perfectly adequate may in fact give poor representations of developing instabilities. Figure 5.3 shows the locations of two nodes on a mesh in a model with mode 8-15 applied as imperfection and the displacement behavior of the two nodes for the same nonlinear analysis. The case is .15-70 with imperfection amplitude = 5.

(a)
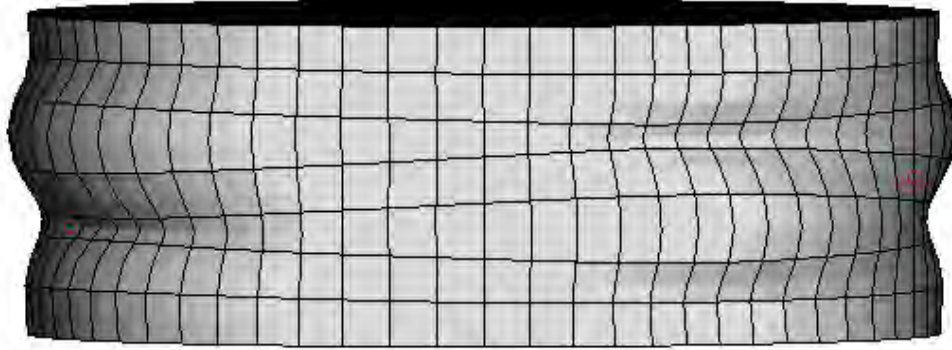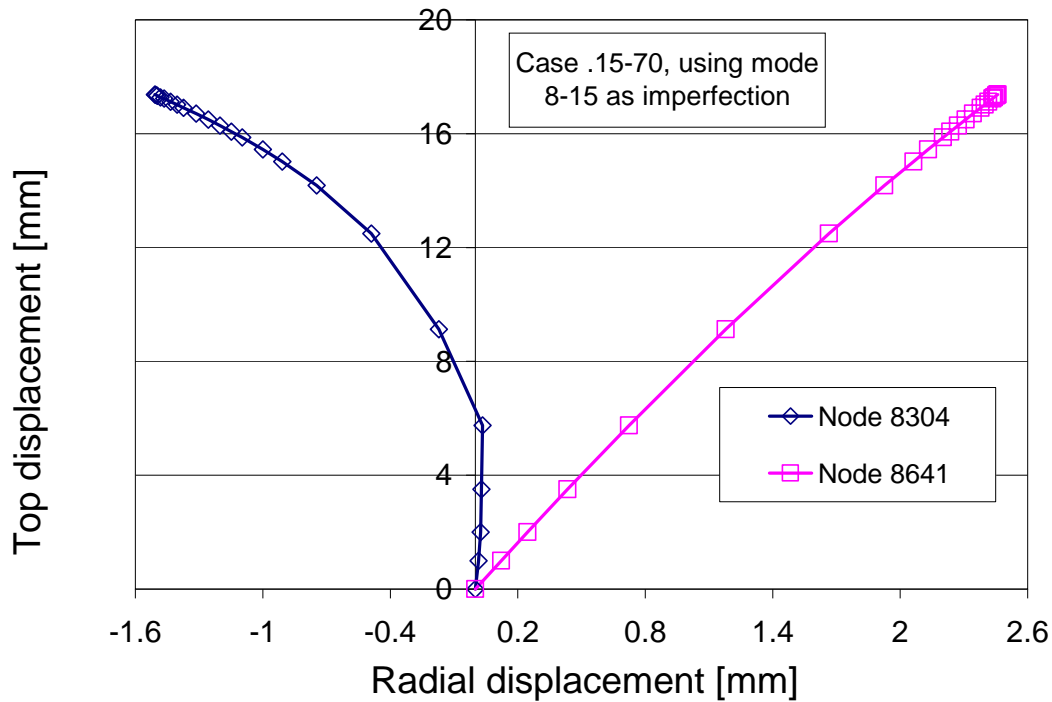
Figure 5.3. Comparison of displacement response in nonlinear analysis with imperfections for nodes in different locations of the same structure; (a) Node locations (Node 8304 at left, 8641 right); (b) Radial displacement response.

A comparison of the radial displacements of node 8304 with those of node 8641 clearly illustrates that node 8641 does not exemplify the nonlinearity of the response. The displacement plot of node 8641 is almost linear, even though it was obtained from a geometrically nonlinear analysis. Nodal displacement behaviors may also differ for various amplitudes. A certain point may illustrate nonlinear behavior well for some amplitude and not another.

In our work, one node was selected to illustrate the displacement response for each mode shape. The selected mode shapes produced comparable behavior for all the amplitudes investigated. These points were chosen for their relevance to the mode shape

and the clear response exhibited at their location. The coordinates for the points chosen

for each mode shape are specified in Table 5.2. The origin of the coordinates is at the

bottom center of the solid. The locations in the mode shape are shown in Figure 5.4.

Table 5.2. Coordinates for selected points.

Mode ID	Node Number	X Coordinate	Y Coordinate	Z Coordinate
6-05	10357	51.11	-85.95	45.00
8-15	8304	-82.29	-56.82	25.00
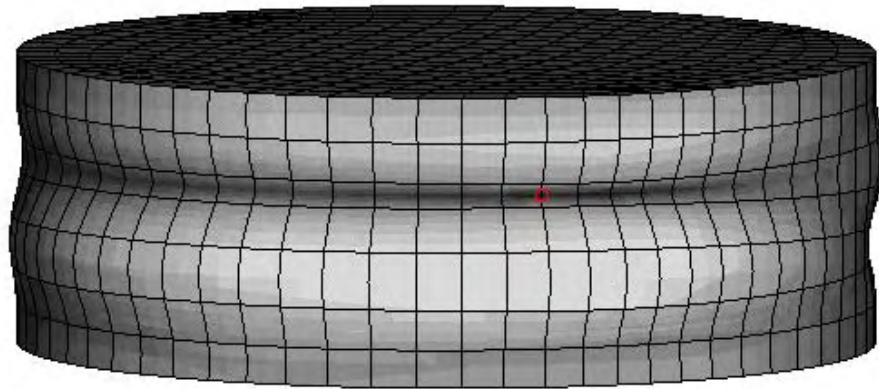
(a)
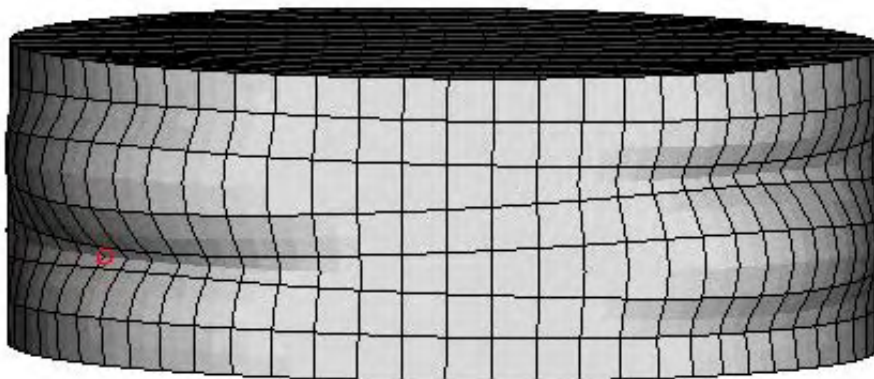
(b)

Figure 5.4 Mode shape location of selected monitoring node for
(a) Mode 6-05, (b) Mode 8-15.

We now illustrate the displacement response for several amplitude/material cases. Figures 5.5 and 5.6 show the changes in response for each material case. The figures show plots of the top displacement versus radial nodal displacement of nonlinear analyses using the aforementioned modes as imperfections with amplitudes set equal to 0 (no imperfection), 1, 3, 5 and 9 for both material cases. In all plots, the vertical axis shows the control parameter of the problem, and the horizontal axis displays the response variable.
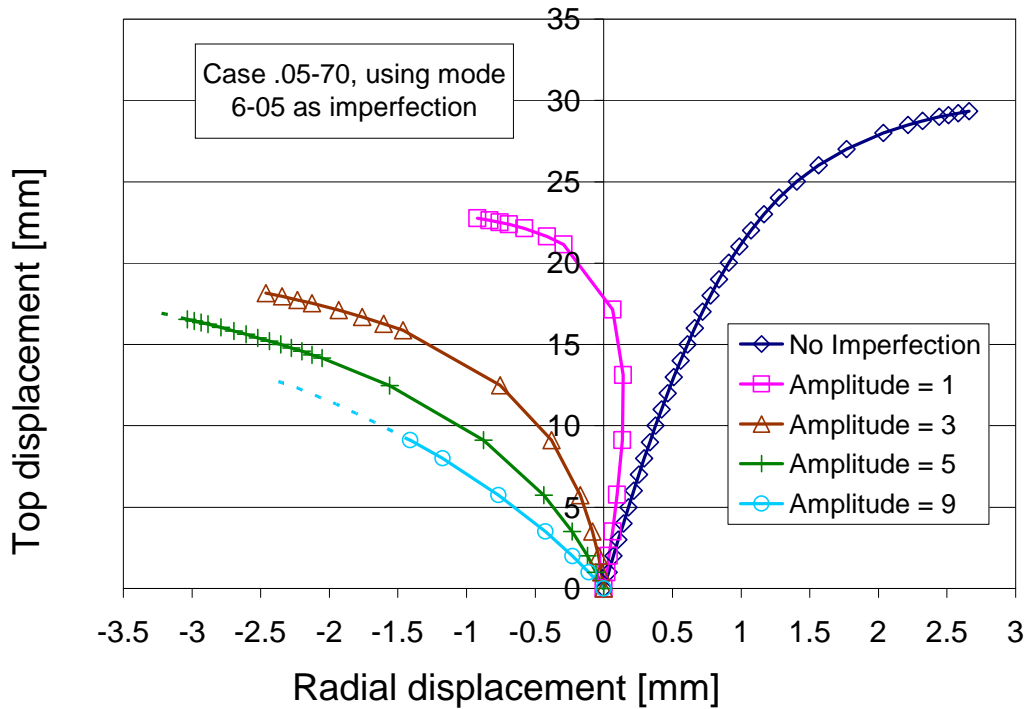
Figure 5.5. Top displacement versus radial displacement plots for varying imperfection amplitudes, Case .05-70 using mode 6-05.
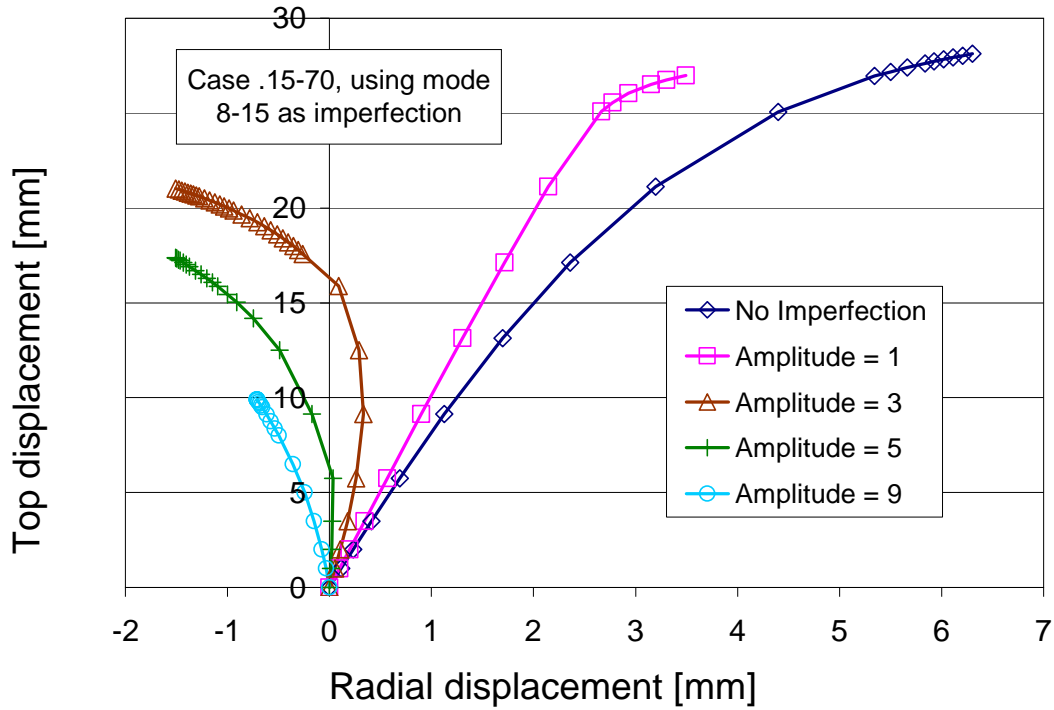
Figure 5.6. Top displacement versus radial displacement plots for varying
imperfection amplitudes, Case .15-70 using mode 8-15.

The effect of increasing the imperfection amplitude of the same mode is
illustrated in the plots. As the imperfection amplitude increases, the point where the
radial displacement increases without bound is found at a lower top displacement level.
The response is seen to reach a point of instability Another effect is also seen in the
graphs. For example, in Case .15-70 for imperfection amplitudes equal to 0 and 1, the
radial displacement is always outward. However, for amplitudes 3 and 5, the mode shape
makes the solid double back on itself, making the displacement curve reverse direction.
This is illustrated in Figure 5.7. The initial outward effect is that of Poisson's ratio, which
is later overcome by the effects of the geometry of the solid.

116
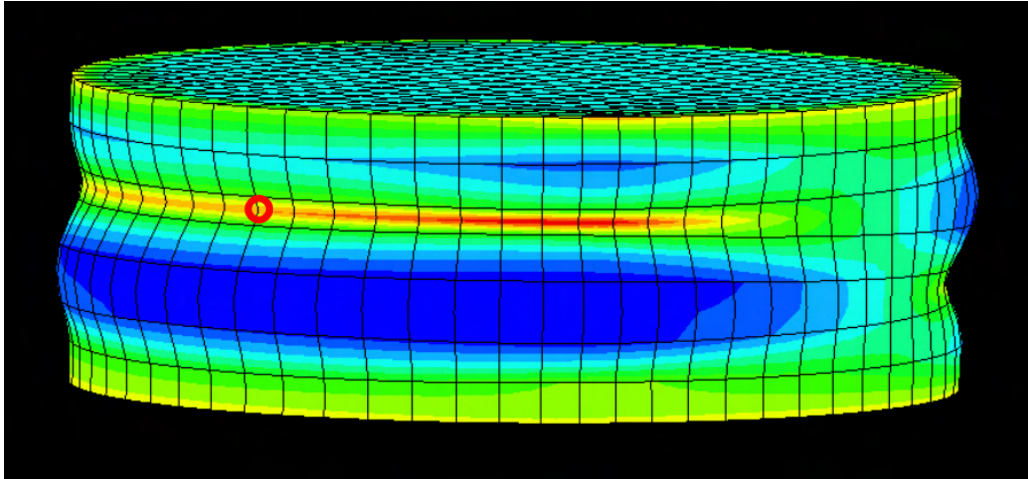
(a)
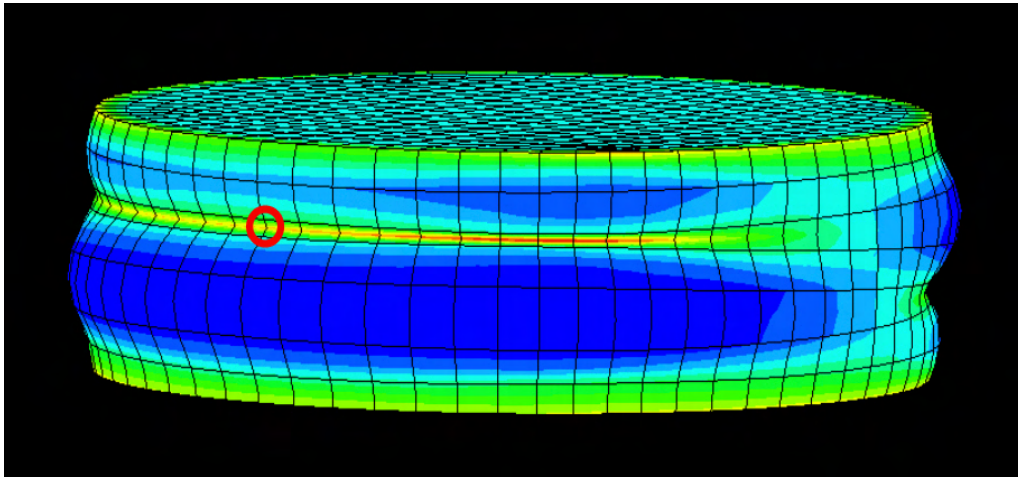
(b)

Figure 5.7. Imperfect geometry influencing displacement direction.

A limitation of the finite element model was encountered at large imperfection amplitudes. The upper and lower bulges of the mode shapes for higher amplitude analyses get close enough to each other during the analysis so that they "touch" and actually invade each other's space in the latter stages of the analysis. Figure 5.8 illustrates this occurrence.
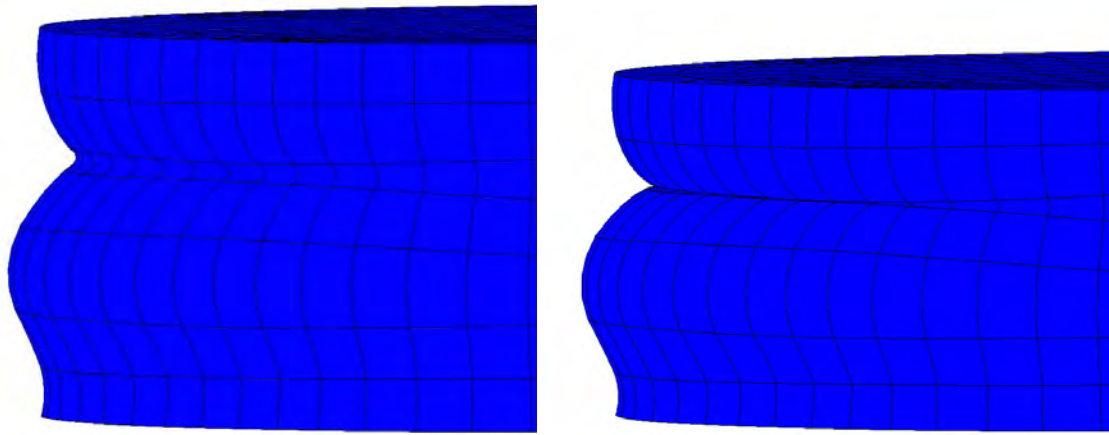
(a)   (b)
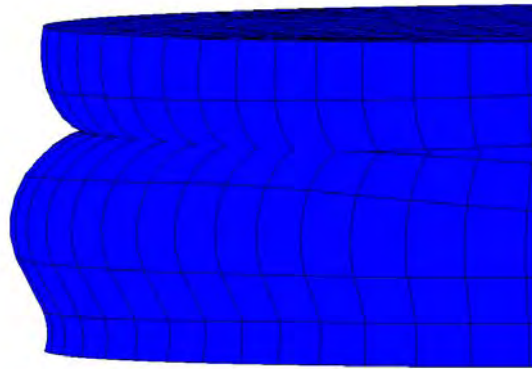
(c)

Figure 5.8. Limitations of nonlinear analysis (a) Inward displacements allow approach of mode bulges (b) Bulges nearly touching (c) Bulges crossing.

This implies changes in the structure behavior and would require contact surfaces to be defined in the outer surface of the solid to be accurately modeled. The nonlinear model with imperfections alone is insufficient to represent such behavior. This effect appears at lower displacements with increasing amplitude. However, the results are still a reasonable approximation, since the bulge surfaces that would come in contact are quite small.

Figure 5.9 shows the imperfection sensitivity curves for both cases studied. The latter portions of the plots in dotted lines indicate the last points in the analyses where the imperfection bulges still do not come into contact, referred to as "break points". From then on, a look into the mesh deformation reveals crossing of the mode bulges.

(a)
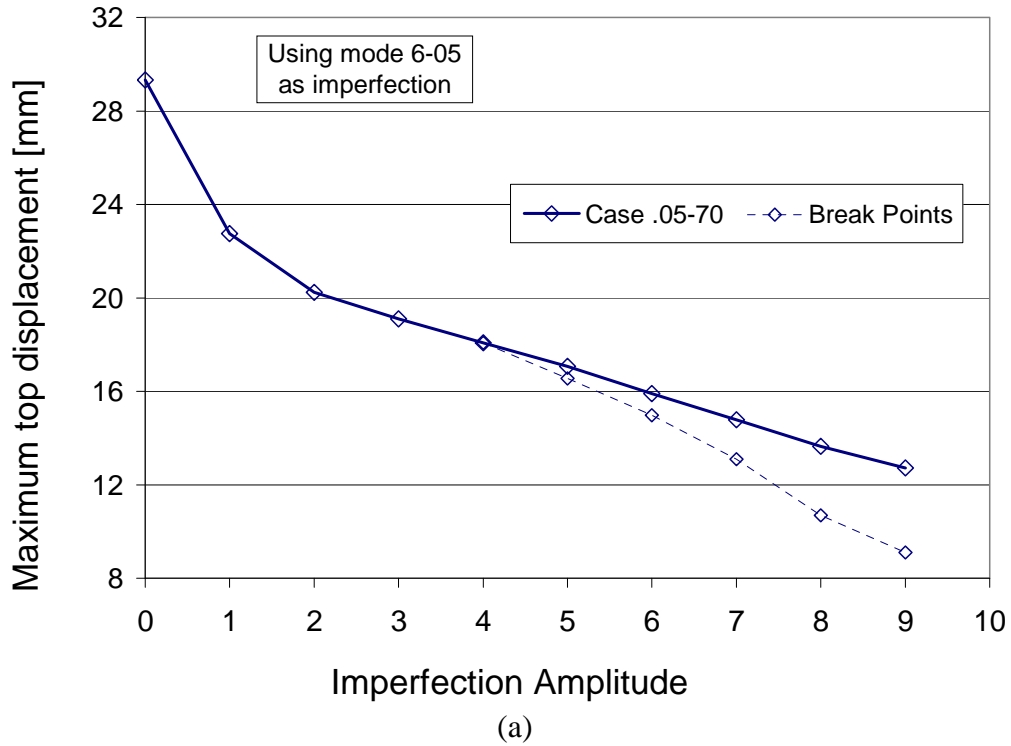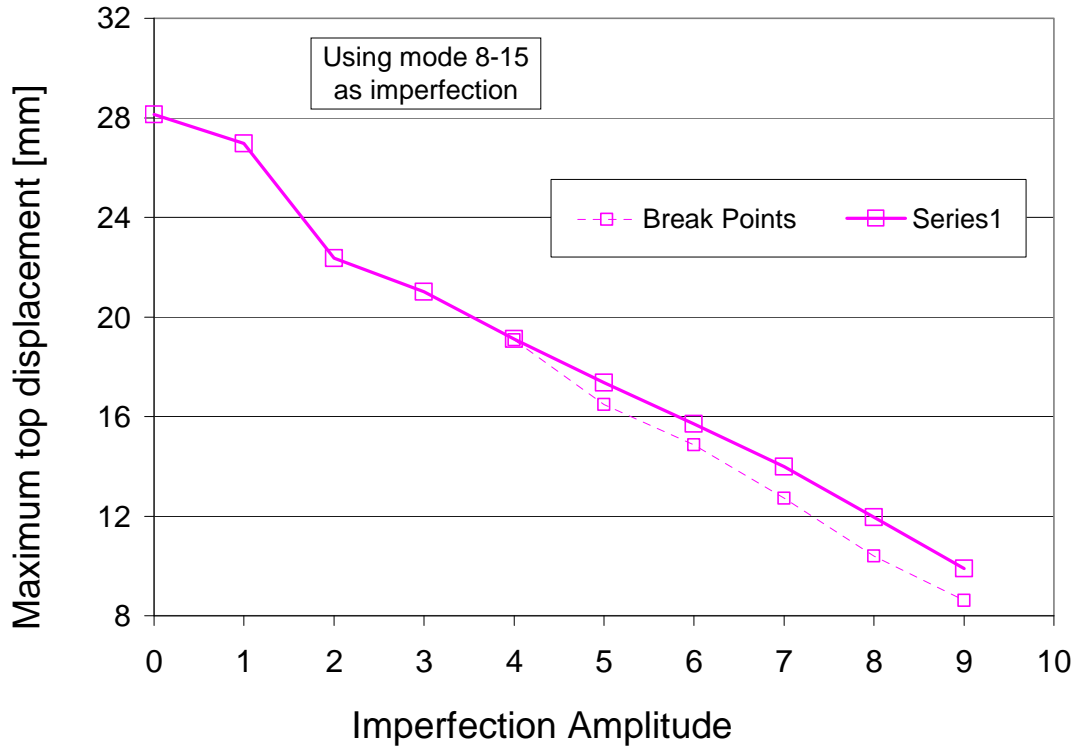
(b)

Figure 5.9. Maximum top displacement versus imperfection amplitudes
(a) Case.05-70, Mode 6-05 as imperfection (b) Case.15-70, Mode 8-15 as imperfection

As Figure 5.9 demonstrates, there is a clear effect of imperfection sensitivity for the solids studied. It is noted that the material with Poisson's ratio equal to 0.05 exhibits a large drop in displacement capacity (from 29mm to 23mm, or 20%) with just a small imperfection amplitude (1%). The second material case, with Poisson's ratio equal to 0.15, seems to be less sensitive, as an amplitude of 2% is needed to achieve a similar effect.

The general trend of the plots seems to be a decrease without bound, but this is unrealistic. We must recall that the finite element results may have inconsistencies springing from the computation of limit points, because the ABAQUS program does not identify physical but numerical instabilities – points which are affected by factors such as

numerical roundoff, mesh size, and solver tolerances. There is also the additional consideration of the mode shape imposed: for larger amplitudes, the mode shape is so prominent that it can hardly be called an "imperfection" – it becomes a whole new geometry, so the problem becomes a more complex one.

Taking all the above into consideration, it is still evident that there is a detected imperfection sensitivity, that confirms the predictions of stability theory for symmetric structures.

5.3 CONCLUSIONS

Investigating the bifurcation process in a three-dimensional solid, we had previously found that the eigenvalues obtained from linear eigenvalue extraction analyses were very close in magnitude (Chapter 3). In stability theory, such similarities have been found to be indicative of imperfection sensitivity. In this chapter we have verified that the effect of imperfection sensitivity, implied by the close values of the results of the eigenvalue extraction analyses, can also occur for solids.

In our investigation, we have focused on linear-elastic, isotropic materials with low Poisson's ratio, given that our method of analysis only handled limit points accurately for such material cases. While it is not outside the realm of possibility that more incompressible materials may also exhibit such sensitivity (indeed, it seems likely, given that this is more a consequence of the symmetry in the geometry and not of the material of which the structures are comprised), we cannot extrapolate our results for these cases; therefore, for the time being, they remain obscure.

INFLUENCE OF MATERIAL NONLINEARITY

6.1 INTRODUCTION

As previously mentioned, within the field of elastic stability the most studied problems have been those involving columns, plates and shells. However, buckling as a phenomenon is not limited to these types of structures. Instability of thick structures has already been predicted for certain cases: highly anisotropic materials, composite structures with very soft components, continuum approximations of latticed structures and materials that undergo drastic reduction of tangential stiffness (Bažant and Cedolin, 1991). Foams are generally modeled as continuum approximations of a latticed structure, falling under one of these categories.

The material behavior of foams is defined by the microstructural behavior, usually dependent on strut or cell-wall bending or buckling (Gan and Chen, 2005). Foams exhibit a great capacity for deformation, which makes them useful for energy absorption applications. Foams are usually employed as core material in sandwich panels, the instability processes of which have been investigated previously and have gone as far as

including the interaction between global and local instabilities (Léotoing et al., 2005). However, the possibility of a macroscopic type of instability has not been taken into account: the buckling of a solid at a macro level, where there is imperfection sensitivity of the foam material to geometric deviations of the structure from its ideal form. This type of macro sensitivity is distinct and different from imperfection sensitivity of the foam microstructure where morphological deviations play a crucial role in defining the material behavior: these imperfections catalyze the onset of instability that defines the elastic limit of a foam (Gong et al., 2005). Geometric *structural* deviations, on the other hand, would facilitate instabilities in the structure as a whole.

Thus, the problem to be studied is that three-dimensional instability processes in foam material, where according to the geometry of the structure, the expected capacity of deformation of the material may be reduced by instability processes.

Due to the exceedingly large displacements predicted for buckling of linear-elastic solids, a possible application suggests itself: foam materials. Foams in general have a large deformation capacity; thus, they make an ideal target for a computational study of the effects of imperfections on solids on a large displacement range, because they are materials that are so complex that they require computational modeling. Additionally, their properties are such that they are geared toward thick solid configurations in their pure forms - as opposed to sandwich forms, which are covered with solid layers, generating more complex combined behaviors (Hunt et al., 1998).

Instability of thick structures has already been predicted for certain cases: highly anisotropic materials, composite structures with very soft components, continuum approximations of latticed structures and materials that undergo drastic reduction of

123

tangential stiffness. (Bažant and Cedolin, 1991). Foams are generally modeled as continuum approximations of a latticed structure, falling under one of these categories.

Foam materials are structurally comprised of small struts or walls that form polyhedrons, called *cells*. Foams can be *open-celled*, when the polyhedrons are delineated by material struts or fibers, or *closed-celled*, when the polyhedrons are defined by material walls. The main difference between a foam and the solid material from which it is made is the volume that is occupied by air. That property is quantified by the relative density, the ratio of the foam density to the solid density. Foams made from the same base material differ greatly in stress-strain properties as the relative density decreases. Since the relative density is controlled by the production process, foams are also different from their solid base materials in that they can, to an extent, be designed for particular properties.

The compression behavior of foams can be divided into three stages: the foam deforms in a linear elastic manner at small strains (5%). The next deformation stage is a plateau at almost constant stress, caused by the elastic buckling of the columns or plates that define the cell. Finally, the cells are crushed, bringing the cell walls or struts in contact and causing densification, which results in a rapid increase of compressive stress. Ultimate compressive nominal strains of 0.7 to 0.9 are typical (Gibson and Ashby, 1988)

Since foams exhibit complex nonlinear behavior, several material models have been developed to model them (see Arruda and Boyce, 1993, for example). Several of them are available on ABAQUS, all based on a strain energy potential. They include the polynomial form (including the neo-Hookean, Mooney-Rivlin and Yeoh forms), Ogden, Arruda-Boyce and Van der Waals forms (Hibbit et al, 2003). These models are

principally geared towards accurately capturing behavior of foams through calibration with experimental data. The abundance of models illustrates the desire for computational representation of advanced materials.

In this chapter, we investigate the imperfection sensitivity of a thick solid foam. This problem has an added complexity with respect to those investigated in previous chapters: here, not only are the kinematics of the problem nonlinear, but also the constitutive relations. However, the material nonlinearity is assumed to remain elastic at all times. Two hypothetical foams are modeled using a first-order strain energy potential model. The models are calibrated to resemble the behavior of a real polyethylene foam. Geometrically nonlinear analyses with and without imperfections applied are performed on solid cylinders, and the effects evaluated.

6.2 FOAM MATERIAL MODEL

There are three main stress-strain behavior zones for foams: the linear portion, the plateau portion and the densification portion. A typical stress-strain curve for an elastomeric foam is presented in Figure 6.1.
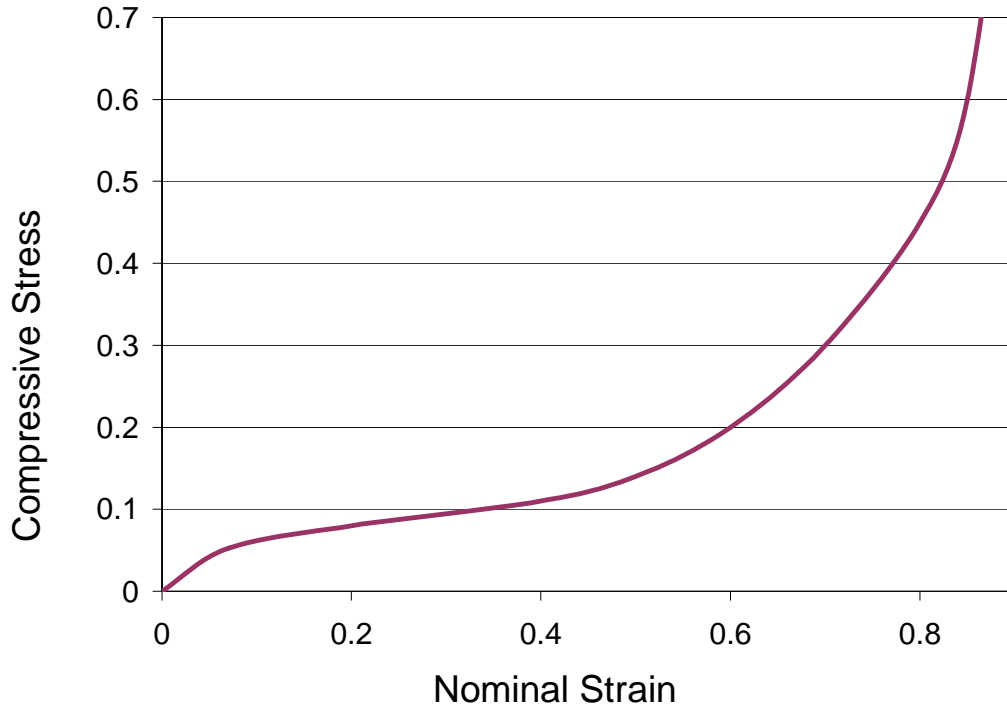
Figure 6.1. Typical stress-strain curve for an elastomeric foam.

These materials have a highly nonlinear behavior as a whole, as such, complex material models are and have been developed to model them. Hyperelastic material models are available in ABAQUS. The appropriate material model option for foams in ABAQUS is the *HYPERFOAM option. This option handles hyperelastic behavior for highly compressible materials like foams (Hibbit et al, 2003). The specific model used was the ABAQUS *HYPERFOAM with a first-order strain energy potential.

Two hypothetical materials were investigated by setting the material parameters as shown in Table 6.1. In the specific material model utilized, the parameters are as follows: μ is the initial shear modulus, α is a curve shape factor, and ν is Poisson's ratio.

Table 6.1. Material parameters used to define each model.

Material	μ [Mpa]	α [Adimensional]	ν [Adimensional]
Case A	0.5	10.0	0.0
Case B	0.5	10.0	0.05

The material parameters were chosen so as to approximate the compressive behavior of a real material; in this case, the stress-strain curve of a polyethylene foam under compression with density equal to 29.4 kg/m^3, as presented in page 181 of Gibson and Ashby (1988). An exact representation was attempted, but it was found that the material model utilized could not be calibrated to represent the exact same curve. However , since our purpose was to investigate a solid structure with a foam material model in general (not to model specific foams), our models will suffice in that they represent behavior not outside the realm of physical reality. Temperature dependency is not considered in the models used. Figure 6.2 shows the compressive stress-strain curves of the material models used as well as the reference polyethylene curve.
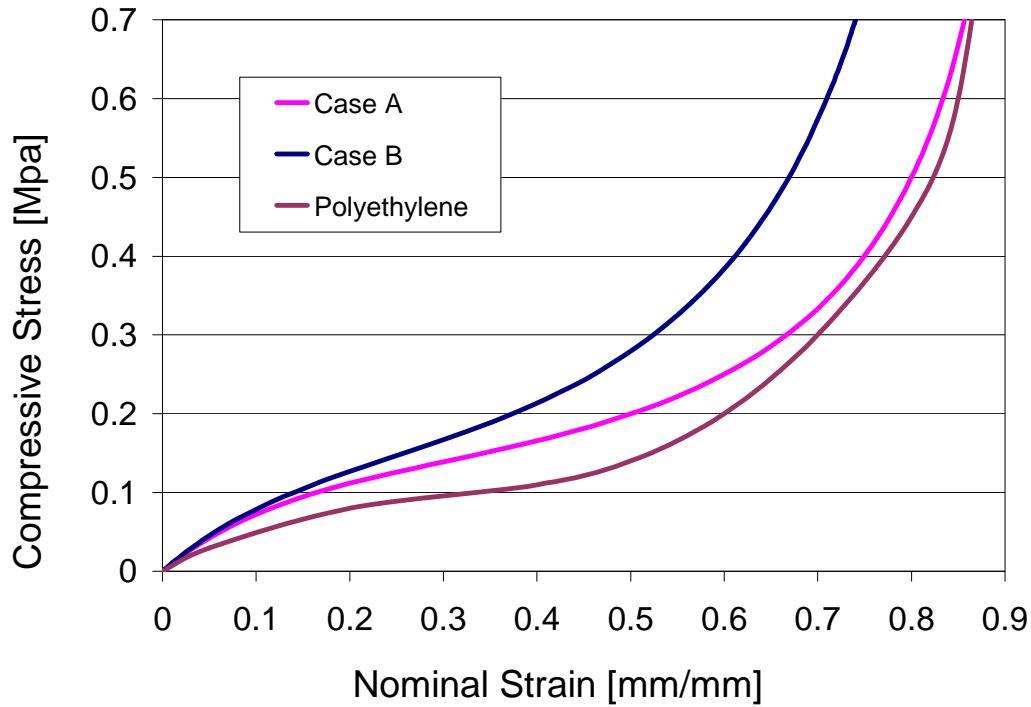
Figure 6.2. Stress-strain curves for two foam models used in computations and reference polyethylene foam.

6.3 EFFECT OF MATERIAL NONLINEARITY

A foam material exhibits a very different stress-strain curve compared to a linear elastic material. The linear part of a foam curve is found at the very beginning, when the microstructural elements are still under loads small enough to induce no disproportionate displacement effects. For the foam cases studied, Figure 6.3 shows a comparison of the stress-strain curves of the foam materials with their completely linear counterparts.
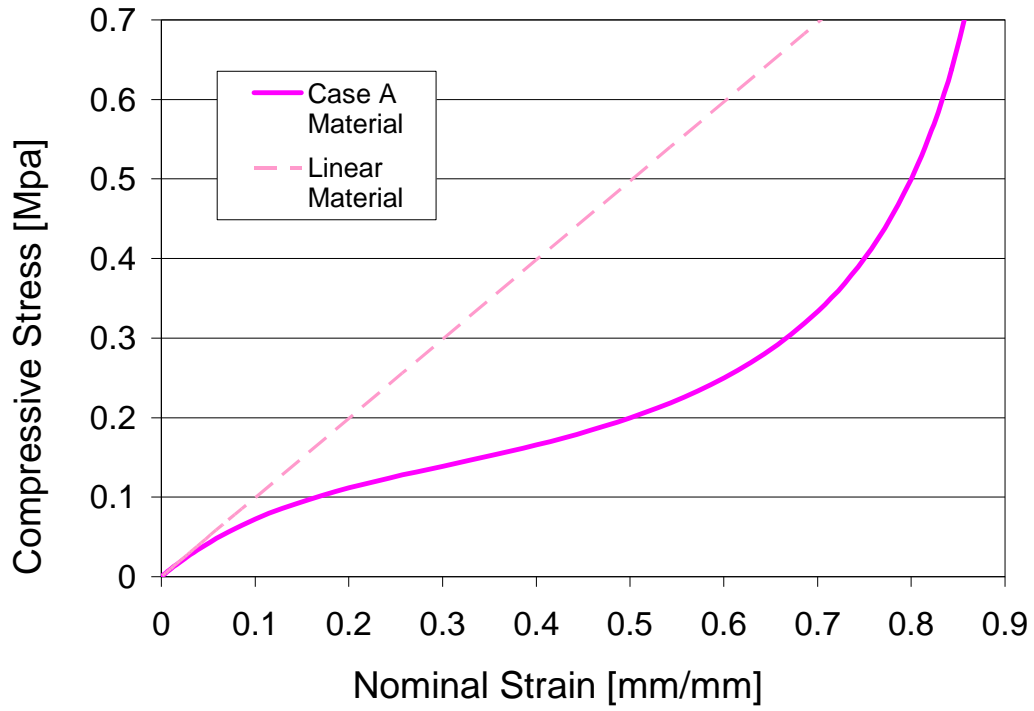
(a)
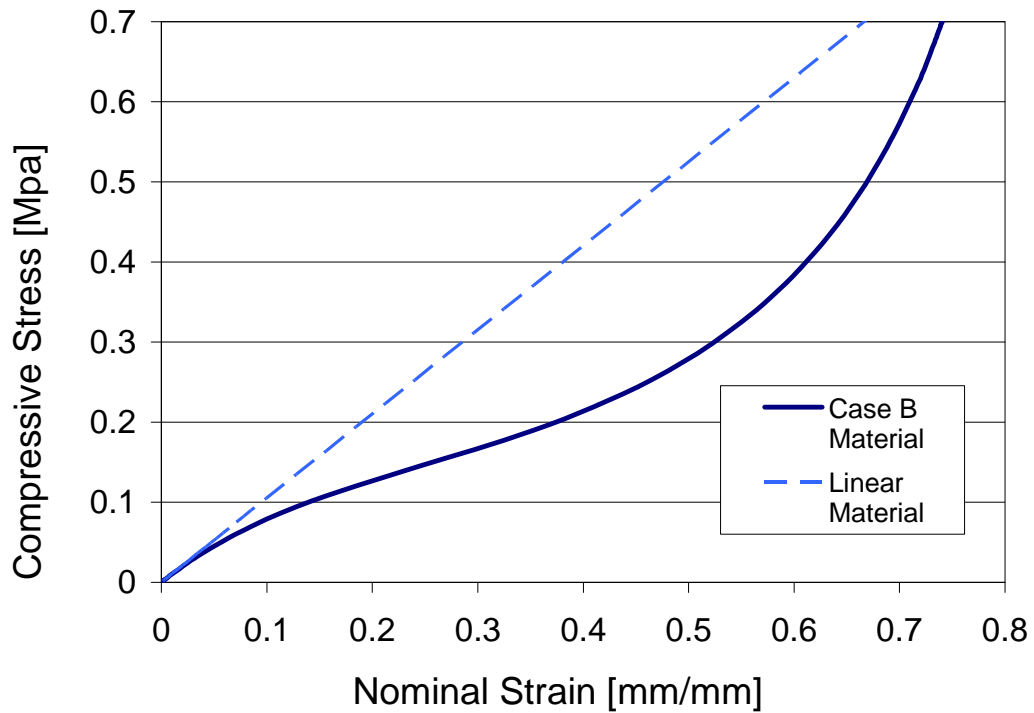
(b)

Figure 6.3. Stress-strain curves for foam models linear counterparts
(a) Case A Material (b) Case B Material

As shown in Figure 6.3, the foam models will attain much larger compressive strains after they exceed their linear portions, compared to their perfectly linear counterparts. This means the solid is more easily deformable.

Comparing the displacement responses obtained from linear materials and the nonlinear foam material we can deduce the effect of the material nonlinearity. Figure 6.4 compares the responses between the Case B foam material and its linear counterpart. No curve is shown for the Case A material since a Poisson's ratio of zero precludes any radial displacement, whether using a linear or nonlinear material.
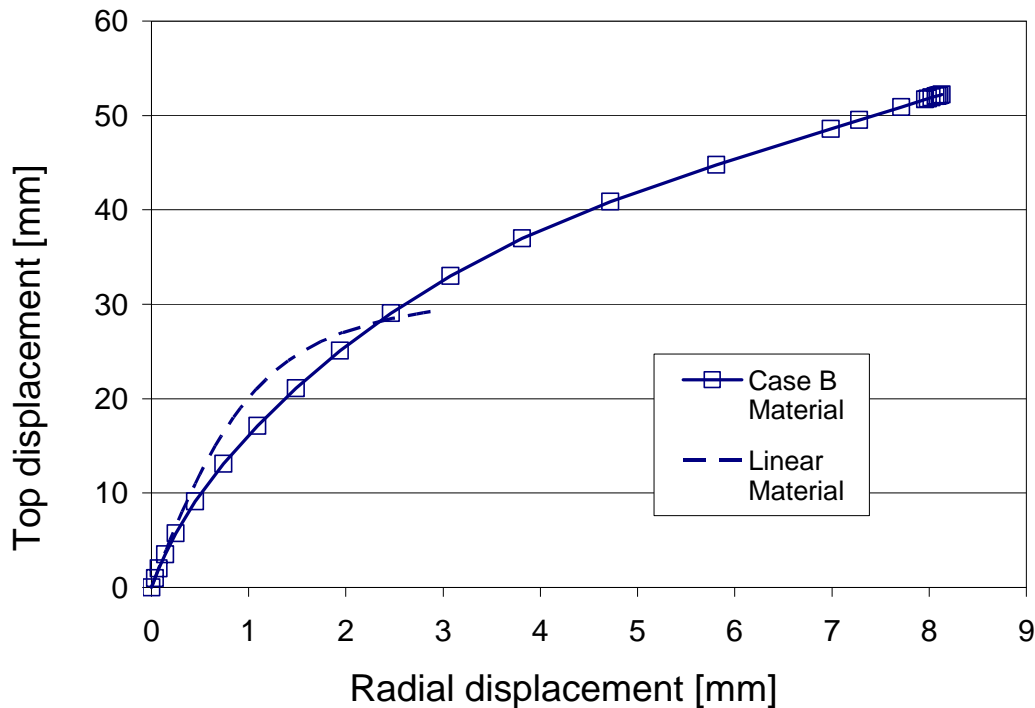
Figure 6.4. Top displacement versus radial displacement plots for linear elastic material and Case B material, both with $\nu=0.05$.

From Figure 6.4 we can see the effect of the material nonlinearity: the curve for the nonlinear material (foam) tolerates much higher top displacements, as the plateau

portion of the material induces much larger deformations for the same compressive displacement. We can also see that the limit point for a linear material is found at a much lower displacement level. The results indicate the material nonlinearity delays buckling, that is, shifts the limit point to a higher value. The high displacement achieved for the foam materials implies large strains. Figure 6.5 again plots the stress-strain curve for the Case B material, and shows the point where the nonlinear analysis encounters a limit point.
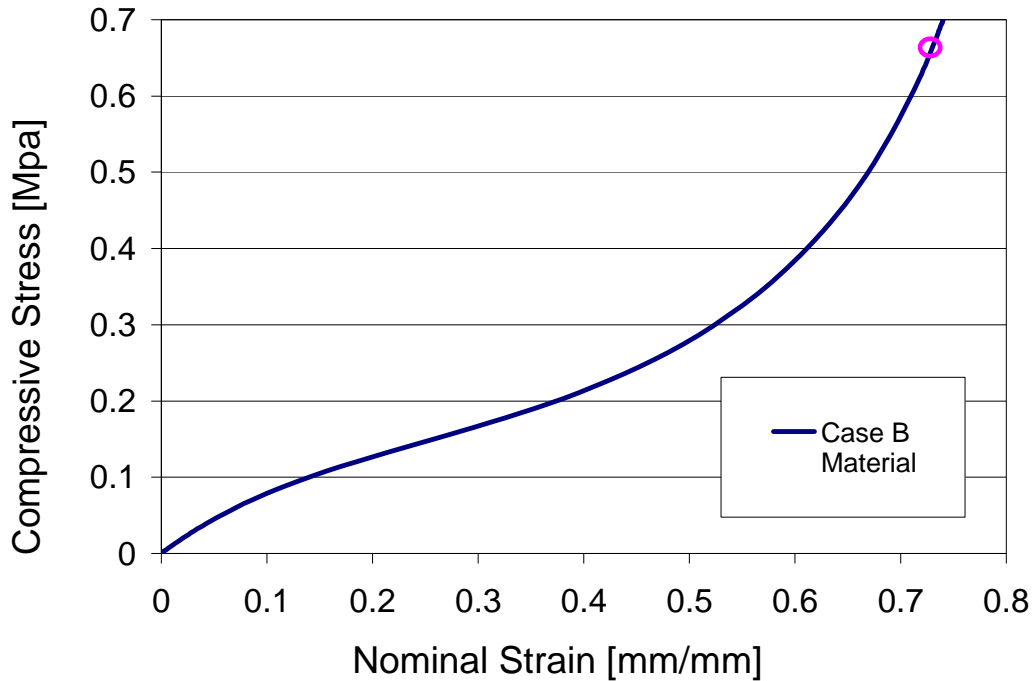
Figure 6.5. Limit point on stress-strain curve, Case B material.

As the figure shows, the limit point is found at a nominal strain of 0.73 – well into the densification part of the material behavior.

6.4 NONLINEAR ANALYSES ON FOAMS

In order to evaluate the imperfection sensitivity of the foam cylinders considered, geometrically nonlinear analyses were performed on finite element models, following the procedure detailed in Chapter 5 for linear elastic material models. Again, the first analysis was performed on a model with no imperfections. Then, nonlinear analyses were performed where an eigenmode obtained from a linear eigenvalue extraction analysis was imposed as three-dimensional imperfection. Since the foam material model is too complex to be used in a linear eigenvalue extraction analysis (Hibbit et al, 2003), the applied imperfection was obtained from the isotropic linear-elastic material model buckling analyses.

We have again selected a mode used previously in Chapter 5 – mode 6 from the buckling analysis of the .05-70 case, named Mode 6-05 (see Chapter 5, section 5.2.2). The imperfection sensitivity was evaluated by comparing the maximum top displacement achieved by the system in each analysis with imperfections with that of the nonlinear analysis with no imperfections.

As was expected, imperfection sensitivity is also detected in the analyses performed using a foam material model. Figure 6.6 and Figure 6.8 show the result of geometrically nonlinear analyses performed on solid cylinder models with material properties as previously shown in Table 6.1. Changes in the displacement behavior are observed according to the imperfection amplitude.

Figure 6.6 plots the top displacement versus radial displacement of nonlinear analyses using Mode 6-05 as imperfection with amplitudes set equal to 1, 3, 5 and 9 for the Case A material. The curve for the case with no imperfection is a vertical line from

the origin, as there is no radial displacement since Poisson's ratio for this material is zero. Therefore, no Poisson's "push" is ever exerted outward. This indicates that the radial displacement response observed in the cases with imperfections is due solely to the geometric effects.
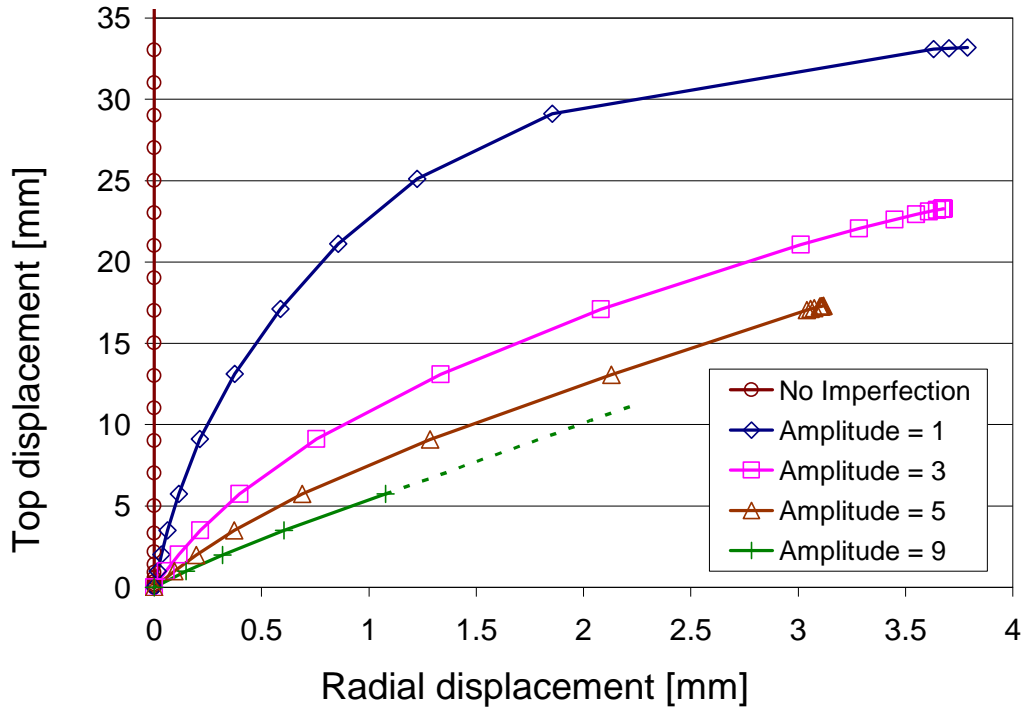
Figure 6.6. Top displacement versus radial displacement plots for varying imperfection amplitudes, Case A material.

It is interesting to note the immediate and large displacement capacity reduction for a unit imperfection amplitude, a drop from 63 mm to 32.5 mm. In Figure 6.7 we plot the limit points on the material stress-strain curve. It is apparent that in the cases with imperfections the material does not even reach the densification portion.
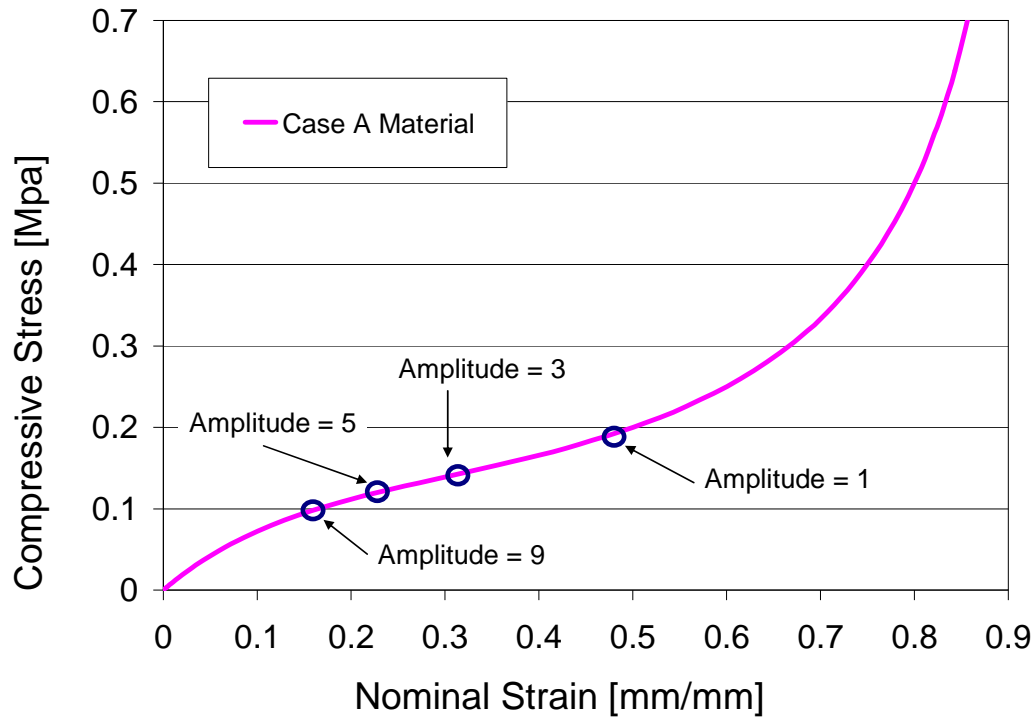
Figure 6.7. Locations of limit points in stress-strain curve, Case A material.

Similarly, Figure 6.8 plots the top displacement versus radial displacement of nonlinear analyses using mode 6-05 as imperfection with amplitudes set equal to 1, 3, 5 and 9 for the Case B material. The response of the case with no imperfections is also presented for comparison. It is notable that the response is quite different for increasing imperfection amplitudes. Also, in Figure 6.9 we again plot the limit points on the material stress-strain curve, for the Case B material. Unlike the Case A material, the unit imperfection case lies well into the densification portion of the material.
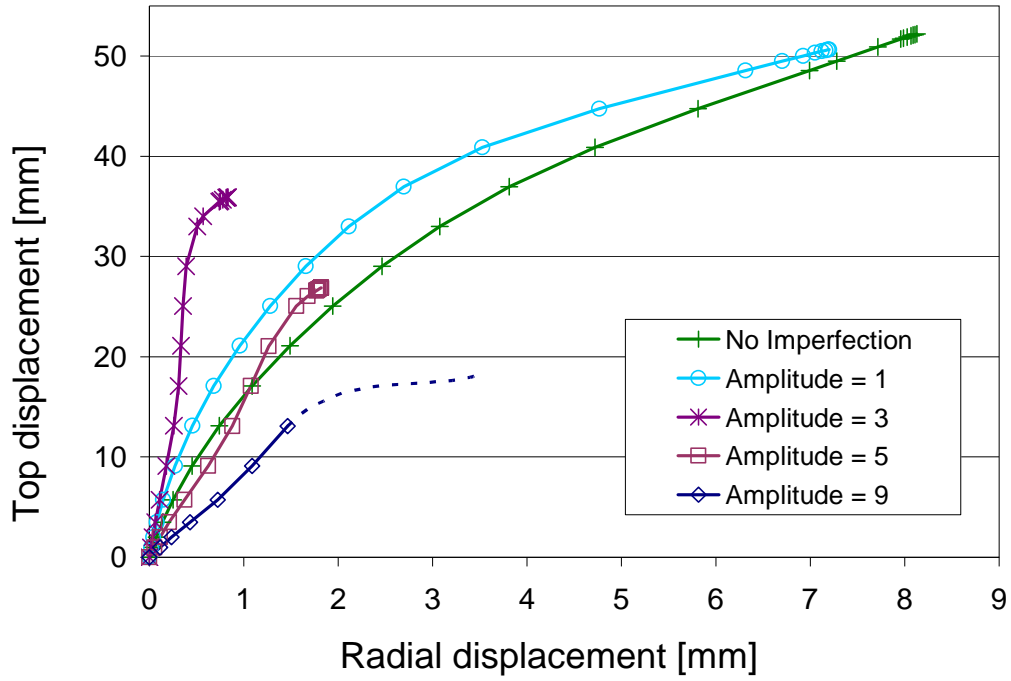
Figure 6.8. Top displacement versus radial displacement plots for varying imperfection amplitudes, Case B material.
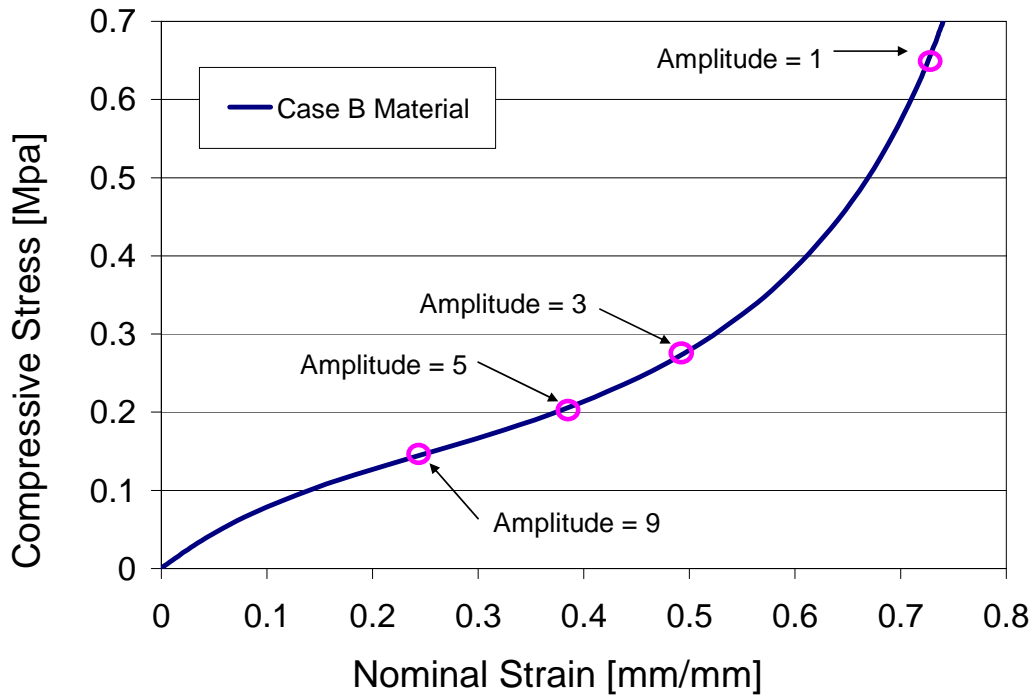
Figure 6.9. Locations of limit points in stress-strain curve, Case B material.

Again, the limitation of the finite element model was encountered, where the upper and lower bulges of the mode shapes get close enough to each other during the analysis to invade each other's space in the latter stages of the analysis (see Chapter 5, section 5.2.2). The upper and lower bulges of the mode shapes for higher amplitude analyses get close enough to each other during the analysis so that they "touch" and actually invade each other's space in the latter stages of the analysis. The dashed curves represent the last points in the analyses where the imperfection bulges still do not come into contact, referred to as "break points". However, for small imperfections, where the bulges do not come into contact, the imperfection sensitivity effect is clear, as is indicated by the graphs in Figure 6.6 and 6.7. The imperfection sensitivity curves for both material cases are plotted in Figure 6.10.
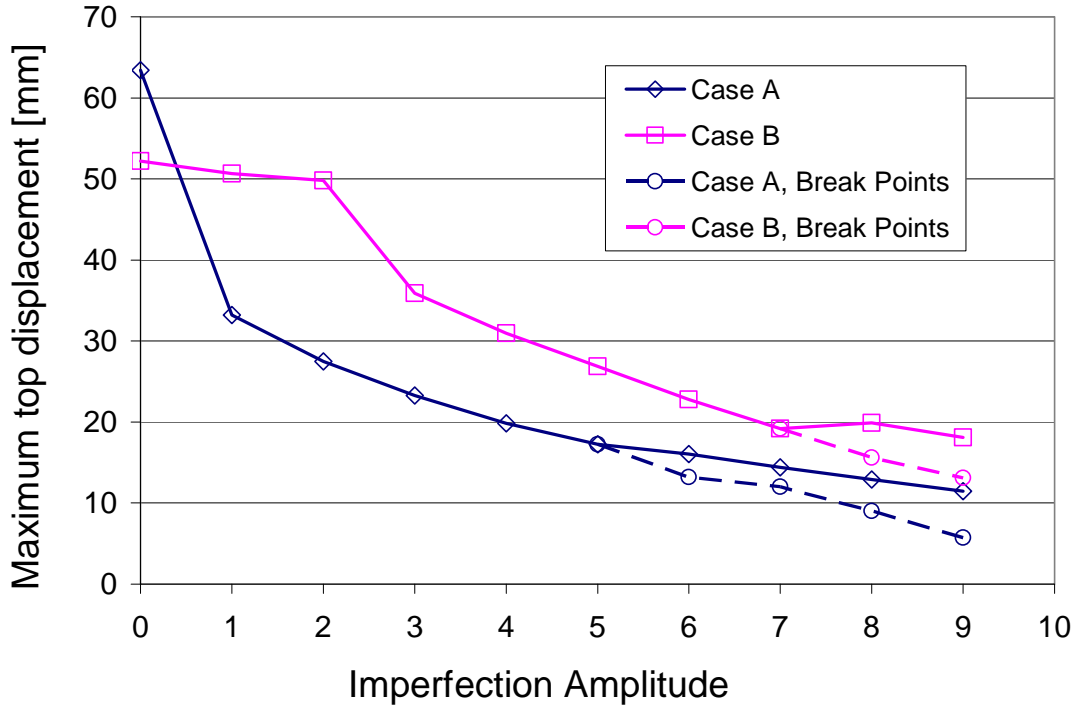
Figure 6.10. Maximum top displacement versus imperfection amplitude for foams

It is notable that the material with Poisson's ratio of zero (Case A) has an immediate and large decrease in deformation capacity with just a small imperfection amplitude. For the Case A material the nonlinear analysis without imperfections yields a maximum displacement of 63.40 mm; with the unit imperfection mode it is 33.19 mm. That is a 47.65% difference in maximum top displacement. Case B also displays imperfection sensitivity, but displays a particular behavior: for small imperfection amplitudes the reduction is slight, but for cases with amplitude 3 and larger, the loss is considerable. The sensitivity curve for Case B resembles the curve for Case A, especially the curve considering the break points, which looks like the Case A curve shifted two amplitudes to the right. Decreased imperfection sensitivity with increasing Poisson's ratio was also seen in the linear elastic materials used in Chapter 5.

6.5 CONCLUSIONS

In this chapter we have explored the behavior of a foam in solid configuration. We have found that material nonlinearity affects the limit point behavior of a given geometry. In the materials studied, foams, the increased deformation capacity gave a greater maximum displacement before reaching a limit point compared to an equally compressible linear-elastic material. This is significant because it implies that the constitutive equations as a whole alter the buckling behavior of a geometry, not only a simple material property like a modulus or a measure of compressibility such as Poisson's ratio.

The nonlinear finite element analyses indicated that imperfection sensitivity is predicted for these materials that are capable of very high strains. Displacement capacity reductions close to 50% were computed for small imperfection amplitudes. It is noticed

that the material modeled with a Poisson's ratio equal to zero had a more noticeable susceptibility to imperfections. This could imply either real imperfection sensitivity of foams with ν equal to zero, or conversely that finite elements show a weakness in this regard, and that it might be better to model a very compressible material using a ν equal to slightly larger than zero.

It is important to understand that the results obtained are mathematical phenomena, not physical. Only actual experiments with foam materials in solid form with carefully controlled imperfections in the manufacture of specimens can establish whether the predicted results are representative of real behavior. If the predicted imperfection sensitivity is an accurate representation of physical phenomena, then a hitherto unexplored (and unconsidered) factor is discovered for materials in solid configuration. This would be important for material modeling because material properties are usually determined from specimens in solid configurations. Imperfection sensitivity could also account for part of the difference in measured response from specimen to specimen.

Conversely, if the predicted phenomenon does not represent physical reality, then it is implied that the theories and/or assumptions involved in the finite element models should be revised.

CONCLUSIONS

7.1 SUMMARY

In this section we present a summary of the investigations in this thesis.

Chapter 1 contains the general introduction to our investigation (instabilities of three-dimensional solids), as well as the motivation, objectives, literature review, scope and methodology followed in the course of the research.

Chapter 2 introduced a simplified analytical approach using the total potential energy formulation. A theme problem of solid cylinder under compressive load was studied for linear elastic materials. Both the derivation of the problem and results of bifurcation buckling analyses were presented. Results were given for various materials and cylinder heights.

Chapter 3 presented bifurcation, linear and nonlinear analyses of the theme problem, using the finite element method. Comparisons were made between all results, including the ones obtained in the preceding chapter.

In Chapter 4, the reduced energy methodology was applied to the 3D solid problem using the analytical formulation developed in Chapter 2. Results were obtained

and the contributions of individual potential energy terms evaluated. The results were compared to those of preceding chapters.

Chapter 5 presented a study of imperfection sensitivity in the theme solid. Buckling modes were imposed as initial imperfections upon the solid geometry and nonlinear analyses performed for different imperfection amplitudes. The results were then compared to the nonlinear analyses without imperfections.

In Chapter 6, the effect of material nonlinearity on the solid buckling problem was evaluated using highly nonlinear materials, foams. Imperfection sensitivity was also explored for these materials. Both nonlinear analyses with and without imperfections were performed. Again, buckling modes were imposed as initial imperfections upon the solid geometry, and the effects of imperfection amplitude evaluated.

7.2 CONCLUSIONS

After a thorough investigation of a theme solid under compression, we come to various conclusions. First and foremost, we have found that instability processes in a thick solid under compression are a structural possibility, a result that corrects erroneous "common knowledge" stemming from conclusions drawn more than a hundred years ago. We have obtained bifurcation points that indicate instabilities at large compressive strains for all materials described by perfectly linear-elastic constitutive equations. Limit points have also been found for very compressible linear elastic materials, and it is seen that these points fall below the eigenvalue buckling points. Therefore, for very compressible linear-elastic materials, the limit point is the controlling instability.

Limitations of the finite-element models became apparent for incompressible materials, so it was impossible to determine limit point behavior for these materials. However, the general trend indicates that for a given geometry, more incompressible materials allow further loading before reaching a limit point. It is possible that the limit point is not the controlling instability for incompressible materials, but this would require further research to be firmly established.

Symmetry in our theme solid, as well as the nearly coincident results for buckling analysis eigenvalues, gave good reason to expect the effect of imperfection sensitivity so important in thin-shell structures. We have verified that there indeed can be imperfection sensitivity on a solid. With the usual method of inputting a mode shape as imperfection on the initial geometry, the capacity was seen to decrease significantly with even small imperfection amplitudes – even more so for the most compressible material studied.

A lower bound approach was attempted using a simplified analytical formulation of the problem. The importance of the energy term transverse to the load was identified. It was found that the buckling results obtained with a reduced energy, while close in magnitude to the calculated limit points, did not represent lower bounds. However, they were close enough (10-15%) to be considered a reasonable first approximation. Also, the reduced energy methodology as developed was consistent in overestimating the limit points for the materials considered, so in this regard it functioned as an upper bound.

Studies with highly nonlinear materials, foams, showed the influence of material nonlinearity on the solid stability. It was found that these highly deformable materials shift the limit point behavior upwards relative to that of an equally compressible linear-elastic material, that is, the limit point occurs at a much higher displacement level. This

indicates that not only compressibility but the whole constitutive equations of the material enter into play in the development of instability. The effect of imperfection sensitivity was also seen to apply to these materials, with drastic displacement capacity reductions.

It is important to note that the results obtained are mathematical phenomena, not physical. Only actual experiments with materials in solid form can establish whether the predicted results are representative of real behavior. The importance of our findings lies in the extensive use of mathematical modeling, especially finite elements, in structural analysis in modern times.

If the predicted instabilities are an accurate representation of physical phenomena, then a hitherto unexplored (and unconsidered) factor is discovered for materials in solid configuration. This would be important for material modeling because material properties are usually determined from specimens in solid configurations, usually cylinders or cubes, precisely to avoid reaching instability points in slender structures and mistaking them for load capacities. Also, imperfection sensitivity could account for part of the difference in measured capacity from specimen to specimen of a given material.

Conversely, if the predicted phenomenon does not represent physical reality, then it is implied that the theories involved in finite element modeling need to be revised – opening up a whole new area of investigation. Even though a foam material model has been investigated, there is the very real possibility that imperfection sensitivity can also affect other materials such as concrete and soil, commonly tested for properties in cylindrical shapes.

7.3 ORIGINAL CONTRIBUTIONS OF THIS THESIS

The original contributions of this thesis are:

1) The identification of instabilities in three-dimensional solids.

2) The understanding of the large strains required to reach points of instability.

3) The determination of the effects of linear elastic material parameters on solid buckling.

4) The identification of imperfection sensitivity in 3D solids.

5) The interpretation of the effect of material nonlinearity in solid stability.

7.4 RECOMMENDATIONS FOR FUTURE WORK

As a theoretical and computational investigation, our work must first and foremost be confirmed by experimental research. This entails dealing with the greater level of complexity studied in this thesis, because real materials always display nonlinear behavior. In addition, material heterogeneity and anisotropy can be issues that can further obscure the effects of instabilities. This represents a truly formidable challenge; however, there are now foundations upon which a knowledge base can be built.

The apparent path to take in order to evaluate the effects of 3D instability is to utilize the easiest constraint to change: the material geometry. Experiments with differing (and controlled) levels of imperfection can begin to establish instability effects.

The use of highly deformable materials can be said to be required for further investigation in this area, since material failure is usually reached before any approach to instabilities in common materials such as concrete and soil.

Our investigation was cut off at a material point because of the inadequacy of the finite element method to handle incompressible materials into limit points. However, it seems like incompressible materials such as man-made rubbers are good candidates for experimental testing, as long as they can withstand large strains. If buckling modes were to be found, they could be directly compared to the ones presented in this thesis; or alternatively, if a limit point were found then the maximum displacement could be compared to the results we have presented.

Once a solid experimental base has been garnered, the reduced energy methodology can be revised from the formulation presented in this thesis, since it is still quite possible that a lower bound method can be implemented with a more accurate formulation, or modified percentages of the energy terms.

Finally, in this thesis we have discussed the case of a cylindrical solid under pure compression, bounded in the top and bottom planes. This is certainly not the only geometric/loading/constraint case by any stretch of the imagination; therefore worlds of knowledge remain to be found regarding the instabilities of three-dimensional solids.

PROGRAM USED FOR SIMPLIFIED ANALYTICAL FORMULATION

This Appendix presents the implementation in the symbolic manipulator Maple of the simplified analytical formulation presented in Chapter 2. The material and geometric properties are specified at the beginning, along with the number of vertical and circumferential waves that describe the eigenmode imposed. The calculation follows automatically, with the load eigenvalue and associated top displacement obtained at the end of the sheet.

```
> #Simplified Analytical Formulation
> restart: with(linalg):
Warning, the protected names norm and trace have been redefined and
unprotected
> interface(prettyprint=0);
> # INPUT
> E:= 7;                    # Elastic modulus [MPa]
E := 7
> nu:= 0.05;               # Poisson's ratio
nu := .5e-1
> R:=100;                  # Cylinder radius
R := 100
> L:=70;                   # Cylinder Height
L := 70
> Ar:= evalf(Pi)*(R^2);   # Cylinder area
Ar := 31415.92654
> # Number of vertical and circumferential waves for mode shape
> M:=3; N:=2 ;
M := 3
N := 2
>
```

```
>  # Calculation starts
>  # Lame's parameters for linear elasticity equations
>
>  mu:=E/(2*(1+nu));
mu := 3.333333333
>  lambda:= (nu*E/((1+nu)*(1-2*nu)));
lambda := .3703703703
>
>  # Linear fundamental path definition
>  sigma11f:=P/Ar; sigma22f:=0; sigma33f:=0;
sigma11f := .3183098861e-4*P
sigma22f := 0
sigma33f := 0
>  epsilon11f:= simplify(1/E*(sigma11f-
nu*(sigma11f+sigma22f+sigma33f)+nu*sigma11f));
epsilon11f := .4547284087e-5*P
>  epsilon22f:= 1/E*(sigma22f-
nu*(sigma11f+sigma22f+sigma33f)+nu*sigma22f);
epsilon22f := -.2273642043e-6*P
>  epsilon33f:=    1/E*(sigma33f-
nu*(sigma11f+sigma22f+sigma33f)+nu*sigma33f);
epsilon33f := -.2273642043e-6*P
>  sigma12f:= 0;
sigma12f := 0
>  sigma13f:= 0;
sigma13f := 0
>  sigma23f:= 0;
sigma23f := 0
>  epsilon12f:=1/2/mu*sigma12f;
epsilon12f := 0.
>  epsilon13f:=1/2/mu*sigma13f;
epsilon13f := 0.
>  epsilon23f:=1/2/mu*sigma23f;
epsilon23f := 0.
>  # Incremental displacement field definition
>
>  x2t:=2*(Pi)*R:
>  u1:=0; u2:=0; u3:=
Q*(x3/R)*sin(M*evalf(Pi)*x1/L)*sin(N*evalf(Pi)*x2/x2t);
u1 := 0
u2 := 0
u3 := 1/100*Q*x3*sin(.1346396852*x1)*sin(.3141592654e-1*x2/Pi)
>  # Cylindrical plot for visualizing mode shapes
>  with(plots):
Warning, the name changecoords has been redefined
>  setoptions3d(title=`Funeral Doom`, style=PATCH, axes=NONE,
        scaling=CONSTRAINED);
>  cylinderplot( { ( 4.5+ ( sin(M*z)* sin(N*theta/2) ) /1.5 )}
,theta=0..2*Pi,z=0..Pi, color = ( 4.5+(sin(M*z)*sin(N*theta/2)))
,grid=[45,35] );
>
>  # Linear incremental field strain terms
>  for i from 1 to 3 do; for j from 1 to 3 do;  epsilon_lin||i||j:=
(1/2)*( diff(u||i, x||j)+ diff(u||j, x||i)); print(epsilon_lin||i||j);
end do; end do;
```

146

```
0
0
.6731984260e-3*Q*x3*cos(.1346396852*x1)*sin(.3141592654e-1*x2/Pi)
0
0
.1570796327e-3*Q*x3*sin(.1346396852*x1)*cos(.3141592654e-1*x2/Pi)/Pi
.6731984260e-3*Q*x3*cos(.1346396852*x1)*sin(.3141592654e-1*x2/Pi)
.1570796327e-3*Q*x3*sin(.1346396852*x1)*cos(.3141592654e-1*x2/Pi)/Pi
1/100*Q*sin(.1346396852*x1)*sin(.3141592654e-1*x2/Pi)
```
>`# Nonlinear incremental field strain terms`
>`for i from 1 to 3 do; for j from 1 to 3 do;  epsilon_no_lin||i||j:=  ( (1/2)*(  add(diff(u||m, x||i)*diff(u||m, x||j), m=1..3)) );`
`print(epsilon_no_lin||i||j) ; end do; end do;`
```
.9063922415e-6*Q^2*x3^2*cos(.1346396852*x1)^2*sin(.3141592654e-
1*x2/Pi)^2
.2114915230e-6*Q^2*x3^2*cos(.1346396852*x1)*sin(.3141592654e-
1*x2/Pi)*sin(.1346396852*x1)*cos(.3141592654e-1*x2/Pi)/Pi
.6731984260e-5*Q^2*x3*cos(.1346396852*x1)*sin(.3141592654e-
1*x2/Pi)^2*sin(.1346396852*x1)
.2114915230e-6*Q^2*x3^2*cos(.1346396852*x1)*sin(.3141592654e-
1*x2/Pi)*sin(.1346396852*x1)*cos(.3141592654e-1*x2/Pi)/Pi
.4934802202e-7*Q^2*x3^2*sin(.1346396852*x1)^2*cos(.3141592654e-
1*x2/Pi)^2/Pi^2
.1570796327e-5*Q^2*x3*sin(.1346396852*x1)^2*cos(.3141592654e-
1*x2/Pi)/Pi*sin(.3141592654e-1*x2/Pi)
.6731984260e-5*Q^2*x3*cos(.1346396852*x1)*sin(.3141592654e-
1*x2/Pi)^2*sin(.1346396852*x1)
.1570796327e-5*Q^2*x3*sin(.1346396852*x1)^2*cos(.3141592654e-
1*x2/Pi)/Pi*sin(.3141592654e-1*x2/Pi)
1/20000*Q^2*sin(.1346396852*x1)^2*sin(.3141592654e-1*x2/Pi)^2
```
>
>`# Linear incremental field stress terms`
>`for i from 1 to 3 do: for j from 1 to 3 do:   if i=j then sigma_lin||i||j:= 2*mu*epsilon_lin||i||j + lambda*add(epsilon_lin||m||m, m=1..3); else  sigma_lin||i||j:= 2*mu*epsilon_lin||i||j; end if;print(sigma_lin||i||j); end do;  end do;`
```
.3703703703e-2*Q*sin(.1346396852*x1)*sin(.3141592654e-1*x2/Pi)
0.
.4487989506e-2*Q*x3*cos(.1346396852*x1)*sin(.3141592654e-1*x2/Pi)
0.
.3703703703e-2*Q*sin(.1346396852*x1)*sin(.3141592654e-1*x2/Pi)
.1047197551e-2*Q*x3*sin(.1346396852*x1)*cos(.3141592654e-1*x2/Pi)/Pi
.4487989506e-2*Q*x3*cos(.1346396852*x1)*sin(.3141592654e-1*x2/Pi)
.1047197551e-2*Q*x3*sin(.1346396852*x1)*cos(.3141592654e-1*x2/Pi)/Pi
.7037037036e-1*Q*sin(.1346396852*x1)*sin(.3141592654e-1*x2/Pi)
```
>`# Nonlinear incremental field stress terms`
>`for i from 1 to 3 do: for j from 1 to 3 do:   if i=j then sigma_no_lin||i||j:= 2*mu*epsilon_no_lin||i||j + lambda*add(epsilon_no_lin||m||m, m=1..3); else  sigma_no_lin||i||j:= 2*mu*epsilon_no_lin||i||j; end if; print(sigma_no_lin||i||j);end do; end do;`
```
.6378315772e-5*Q^2*x3^2*cos(.1346396852*x1)^2*sin(.3141592654e-
1*x2/Pi)^2+.1827704519e-
7*Q^2*x3^2*sin(.1346396852*x1)^2*cos(.3141592654e-
1*x2/Pi)^2/Pi^2+.1851851852e-
4*Q^2*sin(.1346396852*x1)^2*sin(.3141592654e-1*x2/Pi)^2
```

```
.1409943487e-5*Q^2*x3^2*cos(.1346396852*x1)*sin(.3141592654e-
1*x2/Pi)*sin(.1346396852*x1)*cos(.3141592654e-1*x2/Pi)/Pi
.4487989506e-4*Q^2*x3*cos(.1346396852*x1)*sin(.3141592654e-
1*x2/Pi)^2*sin(.1346396852*x1)
.1409943487e-5*Q^2*x3^2*cos(.1346396852*x1)*sin(.3141592654e-
1*x2/Pi)*sin(.1346396852*x1)*cos(.3141592654e-1*x2/Pi)/Pi
.3472638586e-6*Q^2*x3^2*sin(.1346396852*x1)^2*cos(.3141592654e-
1*x2/Pi)^2/Pi^2+.3357008301e-
6*Q^2*x3^2*cos(.1346396852*x1)^2*sin(.3141592654e-
1*x2/Pi)^2+.1851851852e-4*Q^2*sin(.1346396852*x1)^2*sin(.3141592654e-
1*x2/Pi)^2
.1047197551e-4*Q^2*x3*sin(.1346396852*x1)^2*cos(.3141592654e-
1*x2/Pi)/Pi*sin(.3141592654e-1*x2/Pi)
.4487989506e-4*Q^2*x3*cos(.1346396852*x1)*sin(.3141592654e-
1*x2/Pi)^2*sin(.1346396852*x1)
.1047197551e-4*Q^2*x3*sin(.1346396852*x1)^2*cos(.3141592654e-
1*x2/Pi)/Pi*sin(.3141592654e-1*x2/Pi)
.3518518517e-3*Q^2*sin(.1346396852*x1)^2*sin(.3141592654e-
1*x2/Pi)^2+.3357008301e-
6*Q^2*x3^2*cos(.1346396852*x1)^2*sin(.3141592654e-
1*x2/Pi)^2+.1827704519e-
7*Q^2*x3^2*sin(.1346396852*x1)^2*cos(.3141592654e-1*x2/Pi)^2/Pi^2
># Assembly of the total potential energy by terms
># Combination of linear terms
>Va:=  .5*int(int(int( (sigma_lin11*epsilon_lin11   ),
x2=0..2*evalf(Pi)*R), x3=0..R), x1=0..L);
Va := 0.
>Vb:=  .5*int(int(int( (sigma_lin22*epsilon_lin22   ),
x2=0..2*evalf(Pi)*R), x3=0..R), x1=0..L);
Vb := 0.
>Vc:=  .5*int(int(int( (sigma_lin33*epsilon_lin33   ),
x2=0..2*evalf(Pi)*R), x3=0..R), x1=0..L);
Vc := 386.8813174*Q^2
>Vd:=  .5*int(int(int( (2*sigma_lin12*epsilon_lin12   ),
x2=0..2*evalf(Pi)*R), x3=0..R), x1=0..L);
Vd := 0.
>Ve:=   .5*int(int(int( (2*sigma_lin13*epsilon_lin13   ),
x2=0..2*evalf(Pi)*R), x3=0..R), x1=0..L);
Ve := 11073.67025*Q^2
>Vf:=   .5*int(int(int( (2*sigma_lin23*epsilon_lin23   ),
x2=0..2*evalf(Pi)*R), x3=0..R), x1=0..L);
Vf := 61.08652380*Q^2
># Combination of fundamental stress terms and nonlinear strain terms
>Vf1:= .5*int(int(int( (sigma11f*epsilon_no_lin11   ),
x2=0..2*evalf(Pi)*R), x3=0..R), x1=0..L);
Vf1 := .5287288080e-1*P*Q^2
>Vf2:=.5*int(int(int( (sigma22f*epsilon_no_lin22   ),
x2=0..2*evalf(Pi)*R), x3=0..R), x1=0..L);
Vf2 := 0.
>Vf3:=.5*int(int(int( (sigma33f*epsilon_no_lin33  ),
x2=0..2*evalf(Pi)*R), x3=0..R), x1=0..L);
Vf3 := 0.
>Vf12:=.5*int(int(int( (2*sigma12f*epsilon_no_lin12   ),
x2=0..2*evalf(Pi)*R), x3=0..R), x1=0..L);
Vf12 := 0.
```

```
>Vf13:=.5*int(int(int( (2*sigma13f*epsilon_no_lin13   ),
x2=0..2*evalf(Pi)*R), x3=0..R), x1=0..L);
Vf13 := 0.
>Vf23:=.5*int(int(int( (2*sigma23f*epsilon_no_lin23   ),
x2=0..2*evalf(Pi)*R), x3=0..R), x1=0..L);
Vf23 := 0.
># Combination of nonlinear stress terms and fundamental strain terms
>V1f:=    .5*int(int(int( (sigma_no_lin11*epsilon11f    ),
x2=0..2*evalf(Pi)*R), x3=0..R), x1=0..L);
V1f := .5321435985e-1*P*Q^2
>V2f:=    .5*int(int(int( (sigma_no_lin22*epsilon22f    ),
x2=0..2*evalf(Pi)*R), x3=0..R), x1=0..L);
V2f := -.1568506546e-3*P*Q^2
>V3f:=    .5*int(int(int( (sigma_no_lin33*epsilon33f   ),
x2=0..2*evalf(Pi)*R), x3=0..R), x1=0..L);
V3f := -.1846284323e-3*P*Q^2
>V12f:=.5*int(int(int( (2*sigma_no_lin12*epsilon12f    ),
x2=0..2*evalf(Pi)*R), x3=0..R), x1=0..L);
V12f := 0.
>V13f:=.5*int(int(int( (2*sigma_no_lin13*epsilon13f    ),
x2=0..2*evalf(Pi)*R), x3=0..R), x1=0..L);
V13f := 0.
>V23f:=.5*int(int(int( (2*sigma_no_lin23*epsilon23f    ),
x2=0..2*evalf(Pi)*R), x3=0..R), x1=0..L);
V23f := 0.
># Total potential energy
>V:= Va+Vb+Vc+Vd+Ve+Vf  +  V1f+V2f+V3f + V12f+V13f+V23f  +  Vf1+Vf2+Vf3
+  Vf12+Vf13+Vf23  ;
V := 11521.63809*Q^2+.1057457615*P*Q^2
># Variation of potential energy; critical load eigenvalue
>Vcu:=diff(V,Q);
Vcu := 23043.27618*Q+.2114915230*P*Q
>Pc:=solve(Vcu=0,P);
Pc := -108956.0274
># Critical stress and strain
>sigma11c:=Pc/Ar;
sigma11c := -3.468178068
>epsilon11c:= simplify(1/E*(sigma11c-
nu*(sigma11c+sigma22f+sigma33f)+nu*sigma11c));
epsilon11c := -.4954540097
># Top displacement associated to load eigenvalue
>Q:=epsilon11c*L;
Q := -34.68178068
```

REFERENCES:

Arruda, E.M., Boyce, M.C. (1993). *A three-dimensional constitutive model for the large stretch behavior of rubber elastic materials*. Journal of the Mechanics and Physics of Solids, Volume 41, Issue 2, February 1993, Pages 389-412.

Batista, R. (1979). "*Lower bound estimates for cylindrical shell buckling*", Ph.D. Thesis, University College. London.

Bažant, Z.P., Cedolin, L. (1991). Stability of Structures. Oxford University Press, New York.

Bažant, Z.P., Beghini, A. (2004). *Sandwich buckling formulas and applicability of standard computational algorithm for finite strain*. Composites Part B: Engineering, Volume 35, Issues 6-8, September-December 2004, pp. 573-581.

Biezeno, C.B., Hencky, H. (1928). *On the general theory of elastic stability*. Proc. Acad. Sci. Amsterdam 31: 569-592. Vol. 32: 444-456.

Biot, M. (1938). *Theory of elasticity with large displacements and rotations*. Proceedings of the Fifth International Congress of Applied Mechanics. P.117. Cambridge, Mass.

Brush and Almroth. (1975). Buckling of Bars, Plates and Shells. McGraw-Hill, New York.

Bryan, G.H. (1888), On the stability of elastic systems, Proceedings Cambridge Philosophical Society, 6, pp. 199-210.

Burgess, I. W., Levinson, M. (1972). *The instability of slightly compressible rectangular rubberlike solids under biaxial loadings*. International Journal of Solids and Structures, vol. 8, **2**, pp. 133-148.

Crisfield, M. A. (1981). *A Fast incremental/iteration solution procedure that handles snap-through*, Computers and Structures, vol.13, pp. 55–62.

Croll J.G.A. (1975). *Towards simple estimates of shell buckling loads*, Der Stahlbau, Part I, Heft, August, 1975, pp. 243-248; Part II: Heft, September, pp. 283-285.

Croll, J.G.A. (1995). *Towards a rationally based elastic-plastic shell buckling design methodology*, Thin Walled Structures, vol. 23, pp. 67-84.

Croll, J.G.A. and Ellinas, C.P. (1983). *Reduced stiffness axial buckling of cylinders*, International Journal of Solid Structures, vol. 19, **5**, pp. 461-477.

Croll, J.G.A. and Walker, A.C. (1972), Elements of Structural Stability, Halsted Press, John Wiley and Sons, Inc, New York.

del Castillo, J., D. S. Smith, A. M. Vidal, and C. Sierra. (1995). *Catch in the primary spines of the sea urchin* Eucidaris tribuloides*: a brief review and a new interpretation*. Biol.Bull. 188: 120–127.

Elphick, M. R., and R. Melarange. (2001). *Neural control of muscle relaxation in echinoderms*. J. Exp. Biol. 204: 875–885.

Euler, L. (1744). Methodus inveniendi lineas curvas maximi minimive proprietate gaudentes, Additamentum I, De curvis elasticis. Lausanne and Geneva.

Evans, A.G., Hutchinson, J.W., Ashby, M.F. (1999). *Multifunctionality of cellular metal systems*. Progress in Materials Science 43 (3) pp. 171-221.

Gan. Y.X., Chen, C. (2005). *Three-dimensional modeling of the mechanical property of linearly elastic open cell foams*. Int. J. of Solids and Structs. Vol. 42, **26**, pp. 6628-6642

Gibson, L. J. & Ashby, M. F., (1988). Cellular solids: Structure and properties. Oxford: Pergamon Press.

Godoy, L.A. (2000). Theory of Elastic Stability: Analysis and Sensitivity. Taylor & Francis, Philadelphia.

Greenhill, A.G. (1881). *Determination of the greatest height consistent with stability that a vertical pole or mast can be made, and of the greatest height to which a tree of given proportions can grow*. Proceedings of the Cambridge Philosophical Society 4, pp. 65-73

Gong L., Kyriakides S., Jang, W.-Y. (2005). *Compressive response of open-cell foams. Part I: Morphology and elastic properties*. International Journal of Solids and Structures, Volume 42, Issues 5-6, pp. 1355-1379.

Hibbitt, H.D. Karlsson, B.I. and Sorensen, P. (2003). *ABAQUS User Manual, V6.4*, Hibbitt, Karlsson and Sorensen, Pawtucket, RI, USA.

Hunt, G.W.; Da Silva, L.S. and Manzocchi, G.M.E. (1988). *Interactive buckling in sandwich structures*. Proceedings of the Royal Society, London A **417** (1988), pp. 155–177.

Kerr, A.D., Tang, S. (1966). *The effect of lateral hydrostatic pressure on the instability of elastic solids, particularly beams and plates*. J. Appl. Mech. 33. 617-622

Kirchhoff, G. (1877). Vorlesungen uber Mathematische Physik, Teubner, Leipzig.

Koiter, W.T. (1945). *Over de stabiliteit van het elastiche evenwicht*. Dissertation, Delft. English transl. 1970. *On the stability of elastic equilibrium*, NASA TT-F10, 883, 1967, AFFDL-TR70-25

Léotoing, L., Drapier S., Vautrin, A. (2005). *Global, local and interactive buckling in sandwich structures*. http://www.emse.fr/~drapier/ficPDF/ECCM10-Lionel.pdf

Malvern L. (1969). Introduction to the Mechanics of a Continuous Medium, Prentice Hall, Englewood Cliffs, NJ.

Ramm, E. (1981).*Strategies for Tracing the Nonlinear Response Near Limit Points*, Nonlinear Finite Element Analysis in Structural Mechanics, Edited by E. Wunderlich, E. Stein, and K. J. Bathe, Springer-Verlag, Berlin.

Schoen, Frederick J. (2006). *Biomaterial challenges in substitute heart valves*, presented at: Biomaterials for Sensors, Implants and Regenerative Medicine, Boston University, October 21, 2006.

Song, C.Y., Teng, J.G. (2003). *Buckling of circular steel silos subject to code-specified eccentric discharge pressures*. Engineering Structures 25: 1397-1417.

Sosa, E.M. (2005). *Computational buckling analysis of cylindrical thin-walled aboveground tanks*, Ph.D. Thesis, University of Puerto Rico, Mayagüez, Puerto Rico.

Southwell, R.V. (1914). *On the general theory of elastic stability*. Philos. Trans. Roy. Soc. London, Ser A. **213**. pp. 187-244.

Stewart, I., Golubitsky, M. (1992). Fearful Symmetry: Is God a Geometer?.: Blackwell Publishers, Oxford.

Takemae, N., and Motokawa, T. (2005). *Mechanical Properties of the Isolated Catch Apparatus of the Sea Urchin Spine Joint: Muscle Fibers Do Not Contribute to Passive Stiffness Changes*. Biol. Bull., 208(**1**): pp. 29-35.

Thompson, J.M.T and Hunt, G.W. (1973). A General Theory of Elastic Stability. Wiley, London.

Trefftz, V.E. (1933). Zur Theorie der Stabilitat des elastischen Gleichgewichts" (Theory of stability of elastic equilibrium), Z. Angew. Math. Mech, 13, 160-165.

Von Kárman, T. and Tsien. (1941). *The buckling of thin cylindrical shells under axial compression*. Journal of the Aeronautical Sciences, vol. 88, pp.303-312

Washizu, K. (1968). <u>Variational Methods in Elasticity and Plasticity</u>, Pergamon Press, Oxford.

Wu, C.H., Widera O.E. (1969). *Stability of a thick rubber solid subject to pressure loads*. International Journal of Solids and Structures, Volume 5, **10**, pp. 1107-1117.